

EXPERIMENTAL CHEMICAL PHYSICS
OF DROPLETS AND CLUSTERS

Thesis by

Julio Danin Lobo

In partial fulfillment of the requirements for the
Degree of Doctor of Philosophy

California Institute of Technology

Pasadena, California

2001

(Defended 5.17.2001)

...to my grandmother Julia and my parents. My grandmother taught me how to question. My mother taught me to look behind things and understand them. My father taught me how to enjoy the process.

...and to those who have had faith in me

Acknowledgments

The work presented in this thesis was only possible with the collaboration of many others. My advisor, professor Okumura, has always been a source of inspiration. As an advisor, he always expected the best from me. For that, I am thankful. He also has an outstanding quality as an advisor, which is to teach by example rather than by words. I have learnt much from working with professor Okumura. I am equally grateful for the support and for the financial backing throughout my years at Caltech.

For committee members, I had the honor of having Aron Kuppermann, Jack Beauchamp and Nate Lewis. Thank you Aron for your insight and wonderful stories. I always left my exams with a feeling of excitement for new discoveries to be made. Jack always had his door open and it was great fun to work on his ICR machine for chem. 6. My interactions with Nate were restricted to my exams, but I appreciate his practical attitude.

Through my tenure at Caltech, I have been fortunate to collaborate with an array of outstanding people. For a few months, I had the opportunity of working with T. Dibble, from whom I took over the helium source project. Y. Cao and Z. Xhang did much of the time-of-flight setup and S. Lo originally designed the machine. For a summer, I had the pleasure of working with S. Blumberg, a summer 'surf'er, who put me in touch with the Caltech undergrad life and explained to me the meaning of 'grad turkeys'. He helped me complete the setup for the metastable helium experiment.

Y. K. Bae then joined the project. He took occasional breaks from low temperature physics to study eastern medicine. He told me to drink more water after examining my tongue. Bae had many good ideas about improvements to the liquid helium source. C. C. Tsao then joined the project. I was very fortunate to work with Tsao. He had very good lab practices and was very methodological. Tsao taught me that according to the Chinese calendar there are some days in which one should not run

experiments, since on those days they would fail. (We never got any statistics to prove this.) I think it was a hoax to get me to clean the lab.

K. Kuwata introduced me to the 'TOFU' experiment, on which we performed chlorine anion ammonia cluster spectroscopy. A(CK) Wong was my coworker for about a year. He taught me how to operate the 'AFOSR' machine. Together, we conducted vibrational predissociation spectroscopy of cyanide anion water clusters. Wong and I were attempting to produce calcium chloride water clusters when we observed the Ca_2Cl_3 radical, which led to chapters 3 and 4 of this work. Wong is a renaissance man. We spent hours discussing science, eastern philosophy and China's position in the world. J. M. Spotts worked previously on the experiment. He was also very helpful in teaching me about the experiment. A. Deev was the last group member with whom I had the opportunity to work directly. Deev did significant parts of the scanning of the Ca_2Cl_3 radical. I wish Deev the best of luck with the experiment, and I hope I have imprinted on him some of the experimental techniques and scientific ethics I learned from the ones before me. V. Glezakou shared some of her unpublished work on the Ca_2Cl_3 clusters. I would also like to express gratitude to my fellow labmates, whom I did not work directly with, but have had the pleasure of interacting with Garland, Christensen, Rosario, Niemer, Fuelberth, Paik, Gordon, Anderson, Hwuang, and Nizkorodov.

Caltech is a wonderful place for conducting scientific research. I was very fortunate to count with the support of many outstanding professionals, including Duremberg, Roy, and Garcia in the chemistry machine shop; Dunn in the electronics shop; Gerhart in the glass blowing shop; Paniagua in Physics; and technicians in the infrared detector laboratory who taught me many liquid helium techniques. To them and all the staff, which I have met at Caltech, thank you for your help and the excellence in your work.

I would like to thank my parents Ana and Lula, for always giving me emotional and financial support. I love you both. My life in California was made much richer by the friendship and support of the Conner family. I would like to thank my girlfriend Christy for inspiration, companionship, friendship, and for putting up with my crazy schedule. I love you more. Also, I'd like to thank my sisters Ana and Isabel and their families, and my friends Vedad and Adam, for a good time.

Abstract

Time-of-flight measurements of energetic He atoms, field ionization of cryogenic liquid helium clusters, and time-of-flight and REMPI spectroscopy of radical salt clusters were investigated experimentally. The excited He atoms were generated in a corona discharge. Two strong neutral peaks were observed, accompanied by a prompt photon peak and a charged peak. All peaks were correlated with the pulsing of the discharge. The neutral hyperthermal and metastable atoms were formed by different mechanisms at different stages of the corona discharge. Positively charged helium droplets were produced by ionization of liquid helium in an electrostatic spraying experiment. The fluid emerging from a thin glass capillary was ionized by a high voltage applied to a needle inside the capillary. Fine droplets ($<10\ \mu\text{m}$ in diameter) were produced in showers with currents as high as $0.4\ \mu\text{A}$ at $2 - 4\ \text{kV}$. The high currents resulting from field ionization in helium and the low surface tension of He I, led to charge densities that greatly exceeded the Rayleigh limit, thus resulting in coulombic explosion of the liquid. In contrast, liquid nitrogen formed a well-defined Taylor cone with droplets having diameters comparable to the jet ($\approx 100\ \mu\text{m}$) at lower currents ($10\ \text{nA}$) and higher voltages ($8\ \text{kV}$). The metal-halide clusters of calcium and chlorine were generated by laser ablation of calcium metal in a Ar/CCl_4 expansion. A visible spectrum of the Ca_2Cl_3 cluster was observed from 651 to $630\ \text{nm}$ by $1+1'$ REMPI. The spectra were composed of a strong origin band at $15\ 350.8\ \text{cm}^{-1}$ and several weak vibronic bands. Density functional calculations predicted three minimum energy isomers. The spectrum was assigned to the ${}^2\text{B}_2 \leftarrow \text{X } {}^2\text{A}_1$ transition of a planar C_{2v} structure having a ring of two Cl and two Ca atoms and a terminal Cl atom. The ring isomer of Ca_2Cl_3 has the unpaired electron localized on one Ca^{2+} ion to form a Ca^+ chromophore. A second electronic band of Ca_2Cl_3 was observed

at 720 nm. The band is sharply different from the 650 nm band and likely due to a different isomer.

Table of contents

	page
<u>Table of contents</u>	ix
<u>List of tables</u>	xii
<u>List of illustrations</u>	xiv
<u>Summary</u>	1
<u>Chapter 1</u> Generation of Energetic Helium Atom Beams by a Pulsed Positive Corona Discharge	5
Introduction	6
Apparatus	8
Results	11
Discussion	16
Conclusions	20
References	22
Figure captions	24
<u>Chapter 2</u> Generation of Charged Helium Droplets by Field Ionization	35
Introduction	36
Apparatus	38
Experimental procedure	40
Results	42
Discussion	47

Conclusions	54
References	56
Figure captions	59
<u>Chapter 3</u> Electronic Spectroscopy of the Alkaline-Earth Halide Cluster Ca_2Cl_3	70
Introduction	71
Apparatus	73
Experimental results	75
Quantum chemistry calculations	80
Assignment of spectra	84
Discussion	91
Conclusions	97
References	99
Figure captions	113
<u>Chapter 4</u> 720 nm band system of Ca_2Cl_3 .	122
Introduction	123
Experiment	124
Experimental results	125
Quantum chemistry calculations	126
Discussion	130
Conclusions	132
References	133
Figure captions	134

<u>Appendix A</u>	Design of Second Generation Charged Liquid Helium Droplet Source	143
	Summary	144
	New source design	144
	Figure captions	145
<u>Appendix B</u>	Generation of 118 nm photons	155
	Summary	156
	Experimental setup	156
	Experiment	158
	References	158
	Calculations	159
	Figure captions	161

List of tables

Chapter 2

TABLE 2–I Comparison of the charge per unit length for He and N₂ (C/m) 58
 computed for the experimental source conditions (equation 2–2), and the
 Rayleigh limits (equation 2–1). The calculated flow rate and velocity and
 some relevant physical properties are also included.

Chapter 3

TABLE 3–I Observed vibronic transitions of Ca₂³⁵Cl₃ (185 amu). Bands are 102
 assigned to the ²B₂ ← ²A₁ electronic transition of the C_{2v} planar ring
 structure. Predicted vibrational frequencies are from B3LYP/6-311+G(3df)
 calculations.

TABLE 3–II Observed vibronic transitions of Ca₂³⁵Cl₂³⁷Cl (187 amu). Δv¹⁸⁷ 104
 are the shifts observed relative to the frequencies of the bands of Ca₂³⁵Cl₃
 (185 amu). Δv^{calc} are the calculated values. Bands are assigned to one of
 two isomers of Ca₂³⁵Cl₂³⁷Cl, C_{2v} or C_s. Combination bands are calculated
 using observed vibrational frequencies.

TABLE 3–III Observed vibronic transitions of Ca₂³⁵Cl³⁷Cl₂ (189 amu). Δv¹⁸⁹ 106
 are the shifts observed relative to the frequencies of the bands of Ca₂³⁵Cl₃
 (185 amu). Δv^{calc} are the calculated values. Bands are assigned to one of
 two isomers of Ca₂³⁵Cl³⁷Cl₂, C_{2v} or C_s. Combination bands are calculated
 using observed vibrational frequencies.

TABLE 3–IV Observed vibronic transitions of $\text{Ca}_2^{37}\text{Cl}_3$ (191 amu). $\Delta\nu^{191}$ 108
are the shifts observed relative to the frequencies of the bands of $\text{Ca}_2^{35}\text{Cl}_3$
(185 amu). $\Delta\nu^{\text{calc}}$ are the calculated values. Predicted vibrational
frequencies are from B3LYP/6-311+G(3df) calculations.

TABLE 3–V Calculated geometries, energies and vibrational frequencies of 109
the lowest-lying states of the C_{2v} planar ring $\text{Ca}_2^{35}\text{Cl}_3$ structure. Results are
B3LYP/6-311+G(3df) calculations unless otherwise noted.

TABLE 3–VI Calculated geometries, energies and vibrational frequencies of 111
the ground state and energies of some excited electronic states of (a) the
 C_{2v} planar V structure and (b) the D_{3h} trigonal bipyramidal Ca_2Cl_3 structure.
From B3LYP/6-311+G(3df) calculations unless otherwise noted.

Chapter 4

TABLE 4–VII Calculated geometries, energies and vibrational frequencies of 140
the lowest-lying states of the C_{2v} planar V-shape $\text{Ca}_2^{35}\text{Cl}_3$ structure. Results
are from HF/6-311+G(3df) for the ground state and CIS/6-311+G(3df) for
excited state calculations.

TABLE 4–VIII Calculated geometries, energy and vibrational frequencies of the 141

lowest-lying states of the C_{3v} distorted trigonal bipyramid $\text{Ca}_2^{35}\text{Cl}_3$ structure. Results are from HF/6-311+G(3df) for the ground state and CIS/6-311+G(3df) for excited state calculations.

TABLE 4–III Calculated geometries, energy and vibrational frequencies of the lowest-lying states of the C_s rhombus $\text{Ca}_2^{35}\text{Cl}_3$ structure. Results are from HF/6-311+G(3df) for the ground state and CIS/6-311+G(3df) for excited state calculations. 142

Appendix B

TABLE B–I List of equipment for assembly of THG xenon cell. 160

List of figures

<u>Chapter 1</u>	page
Figure 1–1(a) Assembly drawing of experimental apparatus.	26
Figure 1–1(b) Schematic of experiment including detection electronics.	27
Figure 1–2 T-o-f spectra of fast neutral peak with and without repelling potential at conditions of $V_{\text{source}} = 2.0$ kV, $p = 660$ Torr and $V_{\text{skimmer}} = -16$ V. The spectrum with repeller off includes signal due to ions, and is thus larger than the spectrum with the repeller at 2.2 kV, where the ions are eliminated.	28
Figure 1–3 TOF spectrum showing photon peak, fast neutral peak and slow neutral peak. Slow neutral peak is also scaled up by a factor of 10 for better viewing.	29
Figure 1–4 (a) Dependence of fast neutral intensity on source pressure and voltage. (b) Dependence of fast neutral velocity on source pressure and voltage.	30
Figure 1–5 T-o-f spectra of fast atom peak for various source voltages at conditions of $p = 960$ Torr and $V_{\text{skimmer}} = -16$ V.	31
Figure 1–6(a) Dependence of slow neutral intensity on source pressure and	32

voltage. (b) Dependence of slow neutral velocity on source pressure and voltage.

Figure 1-7 (a) Dependence of fast and slow neutral intensities on skimmer voltage ($V_{\text{source}} = 2.0 \text{ kV}$, $p = 660 \text{ Torr}$). (b) Dependence of fast neutral velocity on skimmer voltage. (The slow neutral velocity was independent of skimmer voltage.) 33

Figure 1-8 T-o-f spectra of fast neutral atoms at various skimmer voltages showing the photon peak, an ionic pulse which increases as the skimmer voltage is varied from +200 V to -400 V, and the fast neutral peak ($V_{\text{source}} = 2.0 \text{ kV}$, $p = 660 \text{ Torr}$). 34

Chapter 2

Figure 2-1 Detailed schematic of the source, droplet cell and cryostat. 61

Figure 2-2 Schematic of the apparatus. 62

Figure 2-3 Scanning electron microscope images of typical tungsten tips. 63

(a) An etched tip prior to use. The radius of the tip is approximately $0.4 \mu\text{m}$.

(b) A tip after a single run in liquid helium.

Figure 2-4 Liquid helium at $T = 2.2 \text{ K}$, $\Delta P = 2 \text{ Torr}$. (a) No voltage applied to the needle tip. A drop clinging to the capillary is apparent. The burst of fluid emerging from the nozzle is induced by pressure fluctuations. (b) $V =$ 64

2 kV. A spray of fine charged droplets is observed. The drop on the capillary exterior has shrunk.

Figure 2-5 Liquid helium at $T = 2.2$ K, $\Delta P = 5$ Torr. (a) No voltage applied to the needle. A stable jet with a diameter of $130 \mu\text{m}$ emerges from the nozzle. (b) $V = 2$ kV. A pulsed coulomb explosion is apparent. 65

Figure 2-6 Effect of charging the Faraday cup. $T = 2.2$ K, $\Delta P = 5$ Torr, and $V = 2.5$ kV. (a) No voltage is applied to the Faraday cup. The jet surface is relatively smooth and there is no sign of deflected particles. (b) $V_{\text{Fc}} = +900$ V is applied to the Faraday cup. The droplet fragments are deflected back and scattered. (c) $V_{\text{Fc}} = -900$ V on the Faraday cup. The charged droplets are accelerated toward the cup and instabilities on the jet surface are produced. 66

Figure 2-7 Droplet formation in He II. $T = 1.8$ K, and $\Delta P = -4$ Torr. (a) $V = 0$ V, (b) $V = 1.75$ kV. Large, irregularly shaped droplets ($200\text{-}300 \mu\text{m}$) are formed. 67

Figure 2-8 The effect of charge on liquid nitrogen. $T = 70$ K, $\Delta P = 20$ Torr. (a) $V = 0$ V. Wetting of the capillary is observed. (b) $V = 5$ kV. The drop bound to the tip expands and a Taylor cone is seen. (c) $V = 10$ kV. A small jet is ejected. 68

Figure 2-9 The effect of charge on liquid nitrogen spraying, $T = 70$ K, 69

$\Delta P = 40$ Torr. (a) No voltage is applied to the needle. (b) $V = 5$ kV. (c) $V = 8$ kV. The jet length is shortened and the droplets become slightly smaller as the needle voltage is increased.

Chapter 3

Figure 3–1 Laser vaporization source. The calcium rod was ablated at the throat of a supersonic expansion of a CCl_4/Ar mixture. 115

Figure 3–2 Multiphoton Time-of-Flight (TOF) mass spectrum. Spectrum was recorded by ionizing with 651 nm and 308 nm radiation. Inset: Ca_2Cl_3 isotopomer peaks. Relative intensities of the Ca_2Cl_3 peaks are close to those expected from the natural chlorine isotope abundances. 116

Figure 3–3 (a) Electronic $1 + 1'$ REMPI spectrum of $\text{Ca}_2^{35}\text{Cl}_3$ ($m/e = 185$ amu). All bands beyond origin are magnified by X36 (b) Stick spectrum of $\text{Ca}_2^{35}\text{Cl}_3$ plotted on a log scale. Dotted lines indicate weak and very weak bands for which the intensities were not quantified due to saturation. 117

Figure 3–4 Overlaid vibronic bands of the isotopomers $\text{Ca}_2^{35}\text{Cl}_3$ (185 amu, solid line) and $\text{Ca}_2^{35}\text{Cl}_2^{37}\text{Cl}$ (187 amu, dotted line). (a) Origin at $15\,350.8\text{ cm}^{-1}$ with a simulation of b -type rotational contour at 9 K (offset curve) (b) ν_8 at $15\,616.7\text{ cm}^{-1}$ and (c) $2\nu_8$ at $15\,881\text{ cm}^{-1}$ bands. 118

Figure 3–5 Comparison of a portion of the spectra of $\text{Ca}_2^{35}\text{Cl}_3$ (185 amu, solid line) and $\text{Ca}_2^{35}\text{Cl}_2^{37}\text{Cl}$ (187 amu, dotted line). 119

Figure 3–6 Structures of Ca_2Cl_3 predicted by B3LYP / [6 - 311G + (3df)] density functional theory calculations. (a) C_{2v} planar V, (b) D_{3h} trigonal bipyramid, and (c) C_{2v} planar ring. 120

Figure 3–7 Relative displacements of the ν_8 normal mode of the C_{2v} planar ring structure. 121

Chapter 4

Figure 4–1 Structures of Ca_2Cl_3 predicted by HF / [6 - 311G + (3df)] and MP2/[6-311G+(3df)] theory calculations. (a) C_{2v} planar V, (b) C_{3v} distorted trigonal bipyramid, and (c) C_{2v} planar ring. 135

Figure 4–2 Electronic 1+1' REMPI spectrum of $\text{Ca}_2^{35}\text{Cl}_3$ ($m/e = 185$ amu). 136

Figure 4–3 Electronic 1+1' REMPI spectrum of $\text{Ca}_2^{35}\text{Cl}_2^{37}\text{Cl}$ ($m/e = 187$ amu). 137

Figure 4–4 Comparison of a portion of the spectra of $\text{Ca}_2^{35}\text{Cl}_3$ (185 amu, solid line) and $\text{Ca}_2^{35}\text{Cl}_2^{37}\text{Cl}$ (187 amu, dotted line). 138

Figure 4–5 Franck-Condon simulation of the transition to the first excited state of the V-shaped C_{2v} symmetry isomer. 139

Appendix A

Figure A–1 Assembly of charged liquid helium droplet source. Components of assembly are shown by arrows. 146

Figure A–2 Assembly of charged liquid helium droplet source with dimensions. 147

Figure A–3 Drawing of the source body. 148

Figure A–4 Drawing of the source cover. 149

Figure A–5 Drawing of the macor piece. 150

Figure A–6 Drawing of the repeller piece. 151

Figure A–7 Drawing of the flange piece. 152

Figure A–8 Drawing of the base piece (top view). 153

Figure A–9 Drawing of the base piece (3-dimensional view). 154

Appendix B

Figure B–1 Drawing of modified blank double-sided flange. 162

Figure B–2 Drawing of internal flange for fixing MgF_2 lens. 163

Figure B-3 Benzene ion signal acquired from oscilloscope. 164

Figure B-4 Plot of benzene ion signal as a function of the xenon pressure in
the THG cell. 165

Summary

Experimental Chemical Physics of Droplets and Clusters

Summary

Each chapter of this work is a self-consistent independent topic of research. The chapters are tied under the general topic of experimental chemical physics of droplets and clusters. Chapters one and two present results from experiments conducted on the generation of molecular beams and liquid droplets of helium. Chapter one reports results that qualitatively explain the origin of the observed time-of-flight products extracted from a corona discharge of helium. In chapter two a new method for the generation of charged liquid helium jets and droplets is demonstrated and discussed within the framework of the Rayleigh limit for charged liquid jets. Chapter three presents resonantly enhanced multi photon ionization (REMPI) spectroscopy results for the newly observed salt cluster Ca_2Cl_3 .

Helium atoms have a special role in the development of Chemical Physics. The small size of helium and the relatively weak attraction of helium to other atoms, make it a special tool for conducting molecular beam scattering and surface scattering experiments. These features and the development of molecular beam techniques have led to an interest in methods to produce well-characterized hyperthermal beams of helium atoms.

The first excited electronic state of helium is 23.1 eV above the atomic ground state. Metastable helium atoms are therefore a very versatile carrier of relatively high energy, which can be employed in a number of applications, including surface bombardment, electron transfer, collision induced ionization and mass spectrometry.

In chapter one, a study of the generation of hyperthermal neutral and metastable atomic beams of helium in a corona discharge supersonic expansion is presented. The products of a corona discharge of helium were expanded into vacuum and analyzed in a time-of-flight mass spectrometer. The observation of three peaks in the time-of-flight and

the measurement of their respective dependencies on the conditions of the corona discharge expansion allowed us to qualitatively explain the origin of the different products and to conciliate discrepant results from the corona discharge literature.

Liquid helium has unusual properties, which are inherently due to Bose-Einstein statistical behavior, and the weak interactions between He – He. As the temperature of liquid helium is lowered beyond 2.2 K, a fraction of the fluid condenses into a superfluid state. This condensate has many unusual properties, such as a low surface tension and a high thermal velocity. Droplets of liquid helium are expected to exhibit novel physics resembling the bulk liquid. Therefore, there is growing interest in methods to produce droplets of liquid helium. Charges injected into liquid helium have served as unique probes of elementary excitations in the superfluid. Similarly, charges may provide a method for elucidating the quantum mechanical and coherent properties of helium clusters and droplets.

In chapter two, a new method for generating charged helium droplets is presented. The method is based on the field injection of charges directly into liquid helium. In most nonconducting cryogenic liquids, such as nitrogen and hydrogen, field injection leads to well characterized Raleigh - Taylor jet instabilities, which break the liquid jet into stable droplets with diameters comparable to that of the jet. In sharp contrast, the injection of charge in a liquid helium jet leads to a coulombic explosion of the jet. The underlying physical limit of the charge sustainable in a liquid jet before it breaks into charged droplets provides the framework for quantitatively explaining the observed phenomena. In superfluid helium, the injection of charge leads to a Rayleigh-Taylor like instability, but the superfluid droplets produced are irregular in shape.

Molecular beams and time-of-flight mass spectrometry are essential tools in the study of gas-phase droplets and clusters. In chapter three, the techniques of molecular

beams and mass spectrometry are combined with laser ablation and laser spectroscopy to study the novel Ca_2Cl_3 alkaline-earth halide cluster.

The study of salt clusters is partly driven by the desire to understand how the simple ionic interaction in the diatomic metal halide scales into the bulk salt properties. Small clusters are important to understand the importance of third and n-body interactions in salt structures. Ca_2Cl_3 is an especially interesting system to study because the valence electron serves as a spectroscopic probe of the molecule. The spectra obtained for a ground to excited state transition of Ca_2Cl_3 in conjunction with Density Functional Theory allowed determination of the geometry and electronic structure of the ground electronic state of the cluster and of the observed excited electronic state.

The chemical physics of a corona discharge of helium, of charged jets and droplets of liquid helium, and of the alkaline-earth halide cluster Ca_2Cl_3 investigated through molecular beam, time-of-flight mass spectrometry and REMPI spectroscopy techniques are here presented. The material presented in chapters one, two and three has been published.^{1,2,3}

References:

1. Generation of Energetic He Atom Beams by a Pulsed Positive Corona Discharge
S-Y. Lo , J. D. Lobo, S. Blumberg, T. S. Dibble, X. Zhang, C-C. Tsao, and M. Okumura
J. Appl. Phys. **9** 5896 (1997).
2. Generation of Charged Droplets by Field Ionization of Liquid Helium
C-C. Tsao, J. D. Lobo, M. Okumura, S-Y. Lo, *J. Phys. D* **17** 2195 (1998).
3. Electronic Spectroscopy of the alkaline-earth Halide cluster Ca_2Cl_3 .
J. D. Lobo, A. Deev, C-K. Wong, J.M. Spotts, M. Okumura, *J. Chem. Phys.* **114** 8913 (2001).

Chapter 1

Generation of Energetic Helium Atom Beams by a Pulsed Positive Corona Discharge

1. I. Introduction

Corona discharges can generate reactive ions, clusters, free radicals, and energetic species. For this reason, corona discharges and discharge-excited beam sources have been employed in a number of applications, including mass spectrometry, environmental remediation,¹ laser spectroscopy,^{2,3} fast atom bombardment ionization,⁴ surface etching,⁵ and fundamental studies of hot atom chemistry and physics.⁶

One important application has been the generation of well-defined beams of energetic atoms formed by corona and corona-excited discharges in pure inert gases. Searcy⁷ was the first to report the use of a combined sonic nozzle expansion and direct current (DC) corona/glow discharge to generate helium metastables. Searcy's positive discharge generated a fast peak, which he assigned to photons, and a slow metastable peak. In 1975, Leasure *et al.*,⁸ with a slightly modified design, observed two distributions from the spectrum: a fast, hot metastable peak with 5 eV energy and a slower supersonic peak. By further modification of the source, Fahey *et al.*⁹ observed a fast 800 eV helium peak, which they characterized as being predominantly ground state neutrals. In 1980, the same group¹⁰ using a negative discharge produced spectra containing only low-energy metastable and photon peaks, suggesting the fast neutrals were not generated with negative discharges. Verheijen *et al.*¹¹ expanded on Fahey's work on negative discharges. Again, no fast peak was observed in their spectra. In their paper greater emphasis was given to the intensity and velocity distributions of the slow metastable peak. The velocity distribution was found to agree with an undisturbed supersonic expansion model, and the intensity was found to correlate with the degree of excitation inside the source and the degree of de-excitation by collision with the residual gas. In 1991, Ferkel *et al.*¹² used two negative discharges in series to produce a beam of metastable atoms in the 0.2-5 eV range. Although Ferkel *et al.* focused on the slow

metastable peak, their spectra did show a small fast peak approximately 20 μs after the photon peak with translational energy around 120 eV.

Most sources used in applications of coronas for generation of energetic atom beams are based on Searcy's design and involve discharges through a dielectric nozzle separating high and low pressure regions. The discharge occurs from the point of a sharp electrode in the high pressure region confined by the dielectric (e.g., a capped glass tube) to a skimmer located in vacuum (10^{-2} to 10^{-5} Torr). The plasma undergoes a supersonic expansion through the nozzle, and the beam is extracted through the skimmer orifice.

Despite the widespread uses of corona discharges for generating energetic beams, there has been little work oriented towards understanding the mechanism of fast neutral atom formation in these sources. On the other hand, many experiments concerning the properties of corona discharges have been conducted^{13,14,15} (for an insightful overview on mechanisms of coronas see Loeb¹⁶) and extensive theoretical literature exists regarding these discharges.^{13,17,18,19} However, the typical configuration for creating atom beams differs considerably from experiments on the properties of corona discharges. In the latter, discharges occur at high uniform pressures in ideal point-to-plane or point-to-cylinder electrode geometries. Furthermore, the currents in corona discharges are typically in the 10-100 μA range; in atom sources, the current between the tip and skimmer may range from microamperes to several milliamperes. Thus, it is not apparent to what extent the atom sources behave like conventional corona discharges.

There have been suggestions that the high velocity atoms generated by these atom sources are formed in the low-pressure region⁸ rather than within the high pressure discharge. Such arguments are based on the assumption that collisional

relaxation of translationally fast atoms is rapid because the mean free path in the high pressure region is short (100 nm length scale). In this picture, fast He atoms are formed by recombination of ions accelerated between the nozzle and skimmer. However, high velocities are also found within high pressure corona discharges, not as random motion of individual atoms but as bulk plasma waves.¹³⁻¹⁶ For example, at the onset of a pulsed positive corona discharge, ionization fronts (streamers) propagate rapidly from the anode tip to the cathode plane. The velocity of the ionization front is typically 10^6 to 10^8 cm/s. Fast atoms can then be generated within a high pressure discharge if they are moving with the propagating plasma front. Several plausible mechanisms for the generation of fast atoms therefore exist.

Here we report a preliminary study of the energetic He atoms extracted directly through a small orifice in a pulsed point-to-plane corona discharge. Such sources have been used in the past to form cluster ions, but the properties of the neutral beams have not been reported. This work is part of an effort to develop a new source designed to generate He and H₂ clusters and droplets at cryogenic temperatures. Here we characterize the fast and metastable atoms generated from within the high pressure discharge and we compare our results to energetic atom beams formed in standard (dielectric nozzle) sources. Based on the physics of corona discharges, we qualitatively discuss the mechanisms by which the fast atoms may be generated.

1. II. Apparatus

The apparatus consisted of a cryogenically cooled, high-pressure discharge source coupled to a time-of-flight (TOF) spectrometer. (A schematic is shown in Figure 1-1a.) Helium discharges were sampled through a small orifice in the source and expanded through two differentially pumped chambers: an expansion chamber and a

detection chamber. TOF measurements were made in the detection chamber using two detectors located at different distances from the source.

The source was contained within a copper block mounted to the base of an RMC model CT-610-1 liquid helium cryostat. In this experiment, the cryostat was filled with liquid nitrogen. The discharge portion of the source, which was sealed with indium, consisted of a hollow cylinder (4 mm in length and 2 mm in radius) capped by a 25 μm diameter platinum nozzle. A 0.2 mm diameter tungsten needle was fixed at 1 mm from the nozzle. The tip of the needle was electrochemically etched and inspected with a microscope before assembly. The needle was held by a screw in a macor plate which ensured perpendicular alignment and electrical insulation. A high voltage lead connected the needle to a 60 M Ω current-limiting resistor in series with an ammeter and high voltage power supply. A 200 M Ω to 200 k Ω voltage divider was connected after the 60 M Ω ballast to allow monitoring of the discharge on an oscilloscope.

Before entering the source, helium gas of 99.995% purity passed through a 15 μm filter, a liquid nitrogen cooled reservoir, and then made thermal contact with the cryostat. Prior to operation, the He inlet line was pumped to less than 100 mTorr lest water should be present. The helium pressure was controlled using a Matheson vacuum regulator (Model 3491). As the gas flowed continuously into the source, a point-to-plane corona discharge was struck between the charged needle and the nozzle. The plasma resulting from the discharge expanded through the aperture into the expansion chamber. This chamber was pumped by a 10" Varian diffusion pump baffled by a liquid nitrogen cryotrap. The base pressure in the expansion chamber was 2×10^{-7} Torr, and rose to 5×10^{-4} Torr when the inlet pressure reached about 800 Torr. Grounded liquid-nitrogen-cooled radiation shields enclosed the source to reduce stray electric fields and

temperature loss. In addition, a grounded copper mesh wire was attached to the discharge cylinder also to reduce stray electric fields.

After traveling 2.5 cm from the nozzle in the expansion chamber, the beam was collimated by a skimmer with an aperture of 2.9 mm and a length of 2 cm before entering the detection chamber. The conical, nickel skimmer was mounted using a flat ring (less than 1 mm thick) clamp in order to prevent shock wave interference. It was electrically insulated and could be floated. Downstream 7 cm from the skimmer, a meshed plane aperture ion optic (repeller grid plate) was raised to a 2.2 kV potential in order to repel positive ions. The detection chamber was pumped by a 1400 l/s Pfeiffer turbomolecular pump. The base pressure in the detection chamber was 1.5×10^{-7} Torr and rose to 1.4×10^{-5} Torr at 800 Torr inlet pressure.

The apparatus for TOF measurements is shown schematically in Figure 1–1b. Absolute velocity measurements were made using the TOF spectra from two independent detectors: a Galileo microchannel plate (MCP) detector (model FTD-2003) permanently situated 109.7 cm away from the nozzle, and an ETP direct dynode electron multiplier (DEM) detector (model AF820) situated on a retractable mount 32.5 cm from the source. Care was taken to ensure reproducibility of the DEM alignment. A grounded mesh was fixed 0.2 cm before the MCP to avoid acceleration of ions. The voltage at the MCP cathode could be adjusted up to -2.0 kV and the anode was typically set at -100 V. The cathode of the DEM was raised to -1390 V.

The signals from the detectors were amplified ($\times 25$) and then digitized by a Le Croy TR8818A Transient Recorder. A Le Croy 6010 Magic Controller communicated via GPIB interface to a PC where data was recorded. Sampling rates varied from 10 ns/point to 640 ns/point. The trigger signal of the TOF was either taken from the sharp

falling edge of the discharge voltage or, as was later found more appropriate, from the signal itself. The trigger signal was fed first to a Tektronix oscilloscope (model 2465A), because of its higher trigger sensitivity. A synchronous peak from the oscilloscope was then fed to a digital delay generator (model DG-535 from Stanford Research Systems), which generated a TTL trigger pulse for the Transient Recorder.

1. III. Results

The source discharge exhibited pulsing behavior for a range of source voltages (both positive and negative) and source pressures. Discharge periods were on the order of milliseconds and varied with the source conditions. For the base condition of needle voltage $V_{\text{source}} = 2.0$ kV and source inlet pressure $p = 660$ Torr, the period was 5.3 ms. The period was found to vary inversely with source voltage, increase with source pressure, and increase as the skimmer voltage was raised from negative to positive values. At pressures lower than 600 Torr, we found that the periodic discharge behavior was unstable. At these conditions, it was often necessary to initiate the discharge by temporarily increasing the pressure or by increasing the voltage.

Due to stray capacitance and impedance mismatch, we were not able to accurately measure the fall time of the discharge, but an upper limit of 10 μs was established for positive discharges (needle as anode). Within this time the voltage dropped at least 40% of the maximum value. The discharge voltage then remained at this low level for 10-20 μs , before slowly rising back to the initial voltage. Measurements of the voltage divider signal indicated that despite the high source voltage (defined as the voltage at the power supply) in the range of 1 – 4.8 kV, the actual potential across the needle ranged approximately from 300 to 450 V. The average current through the

source increased with the source voltage and was in the range from 15 μA to 85 μA . Over a period of the discharge oscillation, the current changed by a few microamps.

The detector signal was composed of ionic and neutral peaks (Figure 1–2) correlated temporally to the fast drop in the source voltage. By increasing the voltage on the ion repelling grid, we were able to eliminate the ion contribution and isolate the neutral component, except for a small ionic peak easily identified by its dependence on the repeller plate voltage and skimmer voltage.

For positive discharges, the neutral TOF spectra contained three large peaks (Figure 1–3). The earliest peak arrived within 1 μs of the discharge onset. When the pressure in the detection chamber was raised to 5×10^{-4} Torr, the signal from the two slower peaks decreased but the very fast signal remained unchanged. This observation indicated that the fast peak was generated by photons, which would have been unaffected by the higher background gas pressure. We assigned the remaining two peaks, which arrived at approximately 10 μs and 300 μs at the farther MCP detector, to neutral He atoms.

The velocities of the neutral atoms were measured independently of the discharge trigger by comparing the arrival times at the two detectors. For a typical run, we found that the two neutral atom peaks typically corresponded to velocities of $\approx 9.6 \times 10^4$ and $\approx 1.2 \times 10^3$ m/s (He atoms with kinetic energies of 190 and 0.03 eV, respectively). We inferred that the slowest peak consisted of electronically metastable helium atoms, since the detectors were only sensitive to particles having more than 20 eV in energy. With the current apparatus we were unable to determine if the faster peak was composed of ground state atoms, metastable atoms, or both. The integrated intensities of the slow and fast peaks were approximately the same. However, we do

not know the relative sensitivities of the detectors to translationally energetic atoms versus electronically metastable atoms; therefore, we could not quantitatively estimate the relative fluxes of the two types of atoms.

From the velocity measurements and the known nozzle-detector distances, we were able to determine the time of origin (time zero) of the fast and slow peaks observed. We found that the fast peak originated at the leading edge of the photon peak, $\approx 0.7 \mu\text{s}$ before the photon maximum. In contrast, the slow metastable peak originated $\approx 40 \mu\text{s}$ after the photon peak. The dual detector setup also allowed us to compare the velocity distributions at both positions. Upon scaling the fast peak signal obtained at the two different detectors, we observed that the distribution at the MCP (rear) detector was $\approx 20\%$ broader than the distribution at the DEM (front) detector. This result implied a small dispersion term in addition to a simple velocity distribution. There are two possible explanations: some neutrals were generated in the nozzle-skimmer region after they had expanded out of the source or there was a small spread in time of origin with the atoms generated first having slower speed than the atoms generated later. The same scaling comparison for the slow peaks showed that the distribution at the MCP was broader by only 3% than that of the DEM. Neither the fast nor the slow metastable velocity distributions fit to a Maxwell-Boltzmann distribution. However, except for a high velocity tail, the slower peak could be fit to the expression:

$$f(v) = A(m / 2kT)^{3/2} v^3 \exp[-(m / 2kT)(v - v_0)^2] \quad (1-1)$$

This formula is appropriate for the velocity distribution of a gas undergoing supersonic expansion. The fit was characterized by a thermal temperature of about 21 K and a mean velocity v_0 of ≈ 1067 m/sec. Therefore, the slow peak had a speed ratio of

about 3.6. In contrast, the velocity distribution of the fast peak had a characteristic long tail on the slow velocity edge and sharp edge on the high velocity end.

For the fast peak, the dependencies of peak velocity and intensity on source voltage and inlet pressure were studied in the ranges $V_{\text{source}} = 1.0$ to 4.8 kV, and $p = 460$ to 970 Torr (Figures 1–4a and 1–4b). In general, we found that the source voltage and pressure dependencies were coupled. For the fast peak, at pressures between 660 and 960 Torr, the intensity increased by 40 to 100% as the source voltage went from 1 to 4.8 kV. At 570 Torr, the intensity tripled as source voltage went from 1 to 3 kV, but then decreased by a few percent as the source voltage reached 4.8 kV. TOF spectra showing the dependence on source voltage are presented in Figure 1–5. In contrast to the large changes in intensity, only small changes of velocity were observed for the fast peak when the source voltage was varied, although the trends were similar. From 760 to 960 Torr, the velocity increased by at most 10% as the source voltage went from 1 to 4.8 kV. At 570 Torr, the velocity increased by 3% for a source voltage range of 1 to 3 kV, and then decreased by 2% as the source voltage went from 4 to 4.8 kV. The intensity and velocity of the fast peak exhibited a weaker dependence on the stagnation pressure setting than on source voltage. At 1 kV, the intensity increased by 100% as the pressure was increase from 670 to 970 Torr. At higher voltages, the intensity increased no more than 10%. The dependence of intensity on pressure was unclear for pressures below 670 Torr. The velocity dependence went through a minimum at 650–850 Torr when the pressure was varied from 470 to 970 Torr, but the variation in the velocity was again very small (less than 10% typically).

The dependencies of the intensity and velocity of the slow peak on source voltage and pressure were also studied for the same conditions mentioned above (Figs. 6a and 6b). The dependence of intensity on voltage and pressure was opposite to that

observed for the fast peak. The intensity was found to decrease as much as 50% with rising voltage and decrease as much as 80% with increasing pressure. The velocity, which showed little variation, increased 5% with increasing voltage and 10% with increasing pressure.

The dependence on skimmer voltage for the fast peak was measured in the range $V_{\text{skimmer}} = -400$ to $+300$ V (Figs. 7a and 7b). A characteristic jump in intensity and velocity was observed as the polarity was switched. The intensity changed by less than 10% for voltages from -400 to -100 V, but it decreased by a factor of 10 near 0 V. From $+100$ to $+300$ V it only decreased by an additional 50%. The velocity did not change for low skimmer voltages, but increased by about 8% as the skimmer voltage increased from -200 V to 100 V. Above 100 V, the velocity was constant. We also observed a qualitative change in the shape of the fast peak as the skimmer voltage was changed from 0 to -400 V. A second, faster component (1.2×10^5 m/s, 300 eV) appeared to augment in magnitude with higher negative skimmer voltages (Fig. 8). We saw a distinct glow protruding from the nozzle when the skimmer was at very negative voltages ($V_{\text{skimmer}} < -300$ V); the plasma glow appeared to extend further into the source region.

For the slow peak, the intensity also showed a large change as the skimmer polarity was switched (Fig. 7a.). From -400 V to -100 V the intensity increased by 10%. From -100 V to $+100$ V it decreased by 52%. From 100 V to 300 V it increased by less than 20%. The skimmer voltage had a negligible effect on the velocity of the slow peak.

For negative discharges (needle as cathode), only the photon and slow metastable peak were observed. These were not characterized further in the current experiment.

1. IV. Discussion

1. IV. a. Corona-Discharge

Although the conditions (1 mm gap, 77 K, nonattaching gas) are somewhat different from conventional air corona discharges, the discharge we observe in this experiment exhibits behavior similar to other repetitive, pulsed, positive point corona discharges. Such discharges are characterized by an initial ionizing streamer which occurs within the first several nanoseconds of the breakdown. Photoionization is often thought to be a major contributor to ionization processes during streamer propagation. If so, emission of very short wavelength photons should be a characteristic of streamers, and would account for some of the early photons we observe. The primary streamer may be followed by secondary streamers and the formation of a longer-lived plasma similar to a glow discharge. The UV photon burst lasts for only $\approx 1\mu\text{s}$, but our current measurements indicate that the discharge persists for about 30–50 μs before slowly relaxing.

1. IV. b. Translationally Hot Atoms

There are several possible mechanisms for the formation of the fast He atoms ($v \approx 10^5$ m/s and $E \approx 190$ eV). These atoms originate within 1 μs of the onset of the discharge. From this result we infer that the translationally hot atoms are associated with the early breakdown of the gas. Furthermore, the similarity in velocity distributions and

intensities between the fast atoms and the ion peaks (observed with the deflector voltage turned on and off - Figure 1–2), suggest that the fast atoms and the ions have a common origin.

The early time of origin of the fast atoms, $\approx 0.7 \mu\text{s}$ before the maximum in the photon peak, should coincide with streamer formation. If this is the case, these fast atoms and ions may be formed in the primary streamer itself. This notion is supported by the similarity between the velocities we observe for the fast atoms (and ions) and the propagation velocities of streamers observed directly by optical methods in pulsed corona discharges. For example, Grangé *et al.*¹³ observed ionizing front velocities of 2×10^5 m/s. Their result is within a factor of two of the fast helium velocities we measure; however, we cannot make a direct comparison, since Grangé's experiments were performed in air with a 1 cm gap at a 7 kV applied potential.

Alternatively, the similarity between the fast atom energy (≈ 190 eV) and the transient discharge voltage (minimum at 150 V and maximum at 400 V) suggests that the fast atoms may be formed by recombination of ions accelerated in the cathode fall region. Neutralization could occur as the ions pass through the orifice in the cathode, or later as it expands. This picture might also be compatible with streamer ionization. Once the streamer reaches a point where it interacts with the cathode space charge, ions at the head of the streamer would be accelerated towards the cathode, and thus be emitted with high energies.

A third alternative, electrohydrodynamic acceleration of the background gas, does not seem plausible. Eichwald *et al.*¹⁹ have calculated the velocity field induced in the neutral background for short gap, highly repetitive He discharges. They found

maximum velocities on the order of 10 m/s, well below the velocities of the fast atoms emitted by this source.

1. IV. c. Metastable Atoms

The slower metastable atoms appear to have a significantly different origin from that of the translationally excited atoms. These atoms originate 30 to 50 μs after the photon peak, indicating that they are formed in the later glow-discharge portion of the pulsed discharge sequence. Furthermore, the intensities of the slow metastable peaks generally have the opposite dependence on source conditions relative to the fast peaks. The slow metastable velocities are also closer to thermal velocities, with a distribution characteristic of atomic beams generated by a supersonic expansion through a small orifice rather than acceleration by high fields. Thus, we attribute the slow peak to metastable atoms that are emitted from a plasma with thermalized neutral gas background, in agreement with the metastables observed by others.^{7,8,10-12}

If we assume an isentropic expansion, then we find that the metastable atoms are produced from expansion of a gas with a stagnation temperature of 131 K. Thus, the plasma 30 to 50 μs after initial breakdown has a neutral background temperature approximately double that of the cell walls. Plasma effects could also explain the high velocity tail of the distribution, which exceeds that expected for a supersonic distribution, since collisions with more energetic charged particles would lead to excess population in high translational energies.

Based on a supersonic expansion model, the dependencies of the slow peak on source pressure and voltage can be qualitatively understood. Higher pressures lead to a stronger expansion from the nozzle, resulting in faster velocities. The stronger expansion also increases the flux and thus the intensity. However, the higher stagnation

density should also lead to increased quenching of the metastable species by collision prior to expansion. The decrease in metastable intensity observed implies that the quenching process dominates. The weak dependence of the intensity and velocity on voltage suggests that the stagnation temperature and the local concentration of excited helium atoms in the glow-discharge region are relatively unchanged. Changes in the electrode voltage may be screened by the plasma.

1. IV. d. Comparison with Previous Beam Experiments

Both translationally hot and thermal metastable atoms have been observed previously. All of these earlier studies used sources with dielectric nozzles in which the discharge was struck between a point inside the nozzle and the skimmer. Curiously, no paper reported photons, fast atoms, and thermal metastables simultaneously. Several papers^{7,8,10-12} have described thermal metastable beams from corona discharge sources, both pulsed and continuous. These authors arrived at a similar conclusion for the mechanism of metastable atom beam generation, i.e., supersonic expansion from a high pressure plasma. The origin of the fast atoms, however, was never addressed.

Fast atoms have been detected with energies ranging from 5 eV to 800 eV in pulsed and continuous discharges. Although Searcy *et al.*⁷ assigned a fast neutral peak to photons, Leasure *et al.*⁸ speculated that the first group might have mistakenly attributed a fast peak to photons. Without knowledge of the time resolution in Searcy experiment it is impossible to know if they observed photons, a fast peak, or both. Leasure *et al.* observed helium atoms at 5 eV and attributed them to metastables. The authors conjectured that these fast atoms were accelerated by collisions in the low pressure region (outside the nozzle). Their reasoning was based on the assumption that metastables accelerated before the nozzle would probably be quenched due to the high

density in the stagnation region. Fahey *et al.*,⁹ in their 1978 publication, observed an 800 eV neutral peak. They detected neither a photon peak nor any other peak with energies below 100 eV. The significantly higher energies may be attributable to different source conditions (8-9 kV and order of milliamps discharge currents), but there is currently no model to account for this result.

Although the anode in our experiment is the grounded nozzle, the skimmer voltage does produce strong effects on the plasma. We found that the skimmer voltage has a significant effect on the intensity of the fast atom peak. Application of a high positive potential leads to a large decrease in neutral intensity (Figure 1–8). This result suggests that the positive field of the charged skimmer (which was located 2.5 cm from the nozzle) might have been sufficient to affect the plasma at the source aperture. Alternatively, if most of the neutralization indeed occurs in the low pressure region, then a positive bias on the skimmer may repel the ions before neutralization. By applying a large negative potential to the skimmer, an increase in plasma glow brightness is observed outside of the nozzle. Thus, the plasma appears to be drawn further out of the source. This correlates with the large secondary peak arriving at $\approx 10 \mu\text{s}$ (with energy equivalent to $\approx 300 \text{ eV}$) in Fig. 8. It is conceivable then that the 800 eV atoms observed by Fahey *et al.*⁹ were formed either in a secondary discharge or by single collision processes in the nozzle-skimmer region. Further experiments are needed to clarify the role of the low pressure region in fast atom formation.

1. V. Conclusions

In our experiment, translationally energetic and slow metastable neutral atoms were observed from a repetitive, pulsed corona discharge, accompanied by photon and

ion peaks. The atoms, ions and photons correlated temporally with the pulsing of the discharge. The fast atoms are associated with the onset of the discharge, at the leading edge of the photon pulse, and may result from the initial streamer in the discharge. The slow metastable peak had a velocity distribution typical of an undisturbed supersonic expansion, with a stagnation temperature of 131 K, and originated 30 to 50 μs after the photon pulse.

There are many possible directions for further investigation. First, experiments are needed to establish a more direct correlation of the discharge plasma phenomena with fast atoms. Perhaps the most direct method would be to obtain images of streamers within a typical corona discharge source and compare the timing and velocity of the streamer with that of the fast atoms. A complementary approach would be to relate the time dependence of the discharge current with the time of origin of the fast atoms. Second, a more comprehensive study of source conditions, specially the needle-to-nozzle gap, voltage and current, stagnation temperature, and skimmer is necessary to account for the wide variations in fast atom velocities and to provide a means of accurately controlling the beam velocity. Finally, control over beam energy could lead to the development of a very powerful new tool with many possible applications. This source could be used as an alternative to other hyperthermal neutral beam sources. For example, the corona source may prove to be simpler, more compact, and more versatile than the laser-detonation sources currently being developed for applications in semiconductor etching.²⁰

1. VI. References

1. T. H. Teich and M. Jacob, *Inst. Phys. Conf. Ser.* **143** 227 (1995).
2. P. C. Engelking, *Rev. Sci. Instrum.* **57** 2274 (1986).
3. M. E. Derose, P. G. Carrick, and C. R. Brazier, *J. Mol. Spectrosc.* **174** 379 (1995).
4. D. Faubert, G. J. C. Paul, J. Giroux, and M. J. Bertrand, *Int. J. Mass Spectrom. Ion Processes* **124** 69 (1993).
5. T. Nishimura, H. Suzuki, and T. Satake, *Appl. Surf. Sci.* **70** 133 (1993).
6. U. Buck, in *Atomic and Molecular Beam Methods*, edited by G. Scoles (Oxford Univ. Press, 1988).
7. J. Q. Searcy, *Rev. Sci. Instrum.* **45** 589 (1974).
8. E. L. Leasure, C. R. Mueller, and T. Y. Ridley, *Rev. Sci. Instrum.* **46** 635 (1975).
9. D. W. Fahey, L. D. Schearer, and W. F. Parks, *Rev. Sci. Instrum.* **49** 503 (1978).
10. D. W. Fahey, W. F. Parks, and L. D. Schearer, *J. Phys. E: Sci. Instrum.* **13** 381 (1980).
11. M. J. Verheijen, H. C. W. Beijerinck, L. H. A. M. v. Moll, J. Driessen, and N. F. Verster, *J. Phys. E: Sci. Instrum.* **17** 904 (1984).
12. H. Ferkel, R. Feltgen, and D. Pikorz, *Rev. Sci. Instrum.* **62** 2626 (1991).
13. F. Grange, N. Soulem, J. F. Loiseau and N. Spyrou, *J. Phys. D: Appl. Phys.* **28** 1619 (1995).
14. E. Marode, *J. Appl. Phys.* **46** 2005 (1975).
15. G. F. L. Ferreira, O. N. Oliveira, Jr., and J. A. Giacometti, *J. Appl. Phys.* **59** 3045 (1986).
16. L. B. Loeb, *Electrical Coronas Their Basic Physical Mechanism* (Univ. of Calif. Press, Berkeley, 1965).
17. P. Bayle and B. Cornebois, *Phys. Rev. A* **31** 1046 (1985).
18. N. Y. Babaeva, G. V. Naidis, *Phys. Letts. A* **215** 187 (1996).
19. O. Eichwald, M. Jugroot, P. Bayle, and M. Yousfi, *J. Appl. Phys.* **80** 694 (1996).

20. K. P. Giapis, T. A. Moore, and T. K. Minton, *J. Vac. Sci. and Tech. A.* **13** 959 (1995).

1. VII. Figure captions

Figure 1–1(a) Assembly drawing of experimental apparatus.

Figure 1–1(b) Schematic of experiment including detection electronics.

Figure 1–2 TOF spectra of fast neutral peak with and without repelling potential at conditions of $V_{\text{source}} = 2.0$ kV, $p = 660$ Torr and $V_{\text{skimmer}} = -16$ V. The spectrum with repeller off includes signal due to ions, and is thus larger than the spectrum with the repeller at 2.2 kV, where the ions are eliminated.

Figure 1–3 TOF spectrum showing photon peak, fast neutral peak and slow neutral peak. Slow neutral peak is also scaled up by a factor of 10 for better viewing.

Figure 1–4(a) Dependence of fast neutral intensity on source pressure and voltage. (b) Dependence of fast neutral velocity on source pressure and voltage.

Figure 1–5 TOF spectra of fast atom peak for various source voltages at conditions of $p = 960$ Torr and $V_{\text{skimmer}} = -16$ V.

Figure 1–6(a) Dependence of slow neutral intensity on source pressure and voltage. (b) Dependence of slow neutral velocity on source pressure and voltage.

Figure 1–7(a) Dependence of fast and slow neutral intensities on skimmer voltage ($V_{\text{source}} = 2.0 \text{ kV}$, $p = 660 \text{ Torr}$). (b) Dependence of fast neutral velocity on skimmer voltage. (The slow neutral velocity was independent of skimmer voltage.)

Figure 1–8 TOF spectra of fast neutral atoms at various skimmer voltages showing the photon peak, an ionic pulse which increases as the skimmer voltage is varied from +200 V to –400 V, and the fast neutral peak ($V_{\text{source}} = 2.0 \text{ kV}$, $p = 660 \text{ Torr}$).

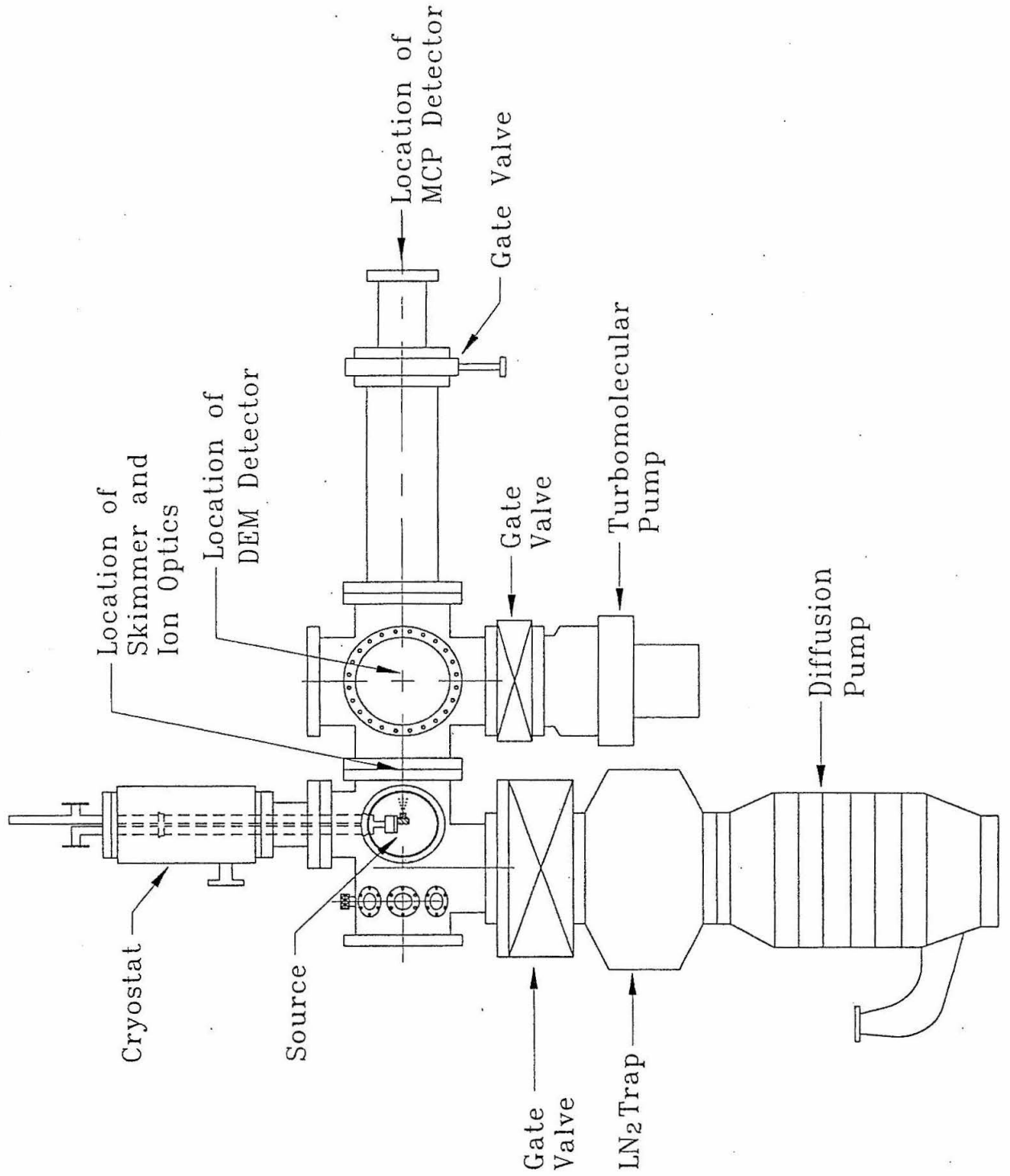


Figure 1-1(a)

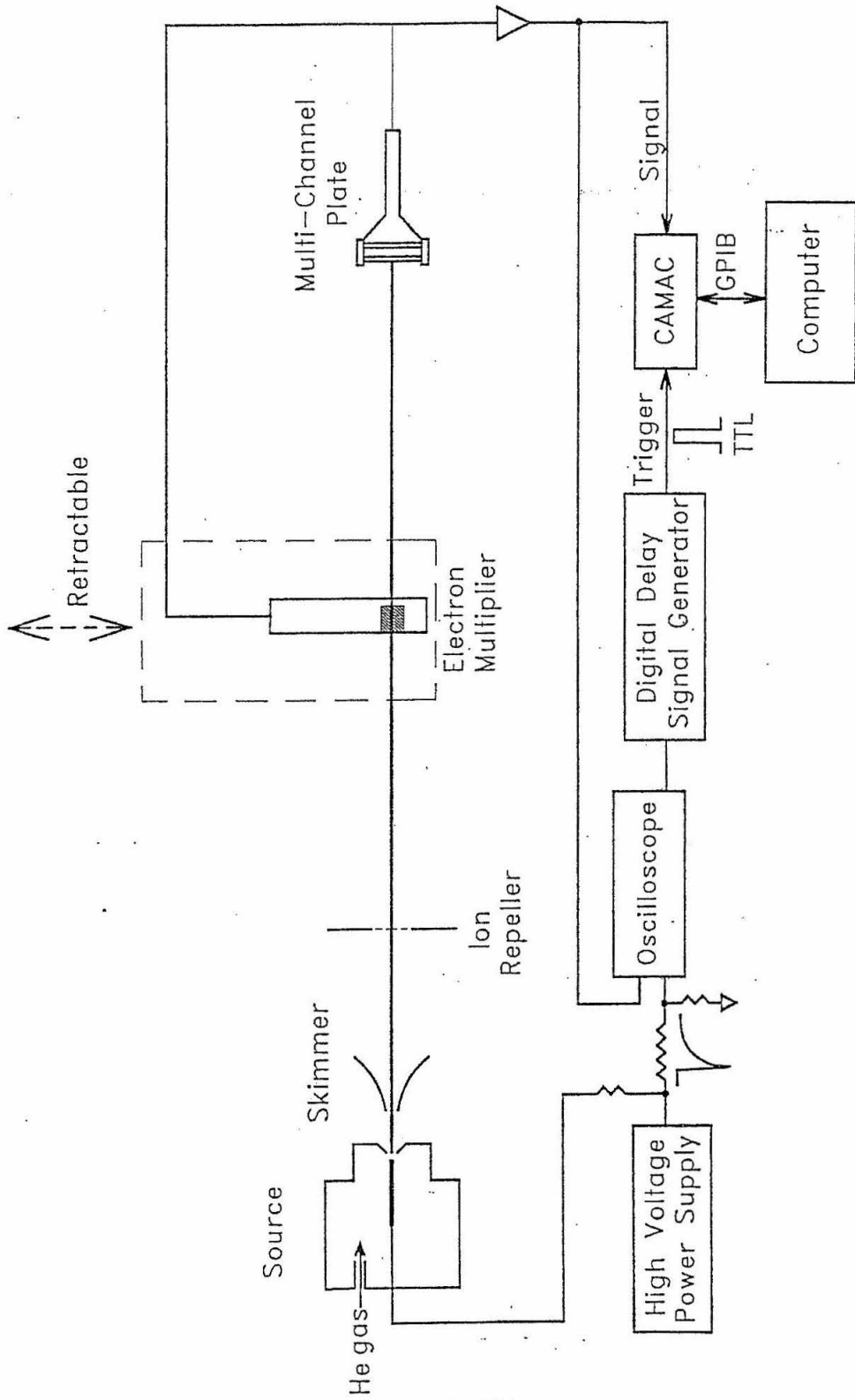


Figure 1-1(b)

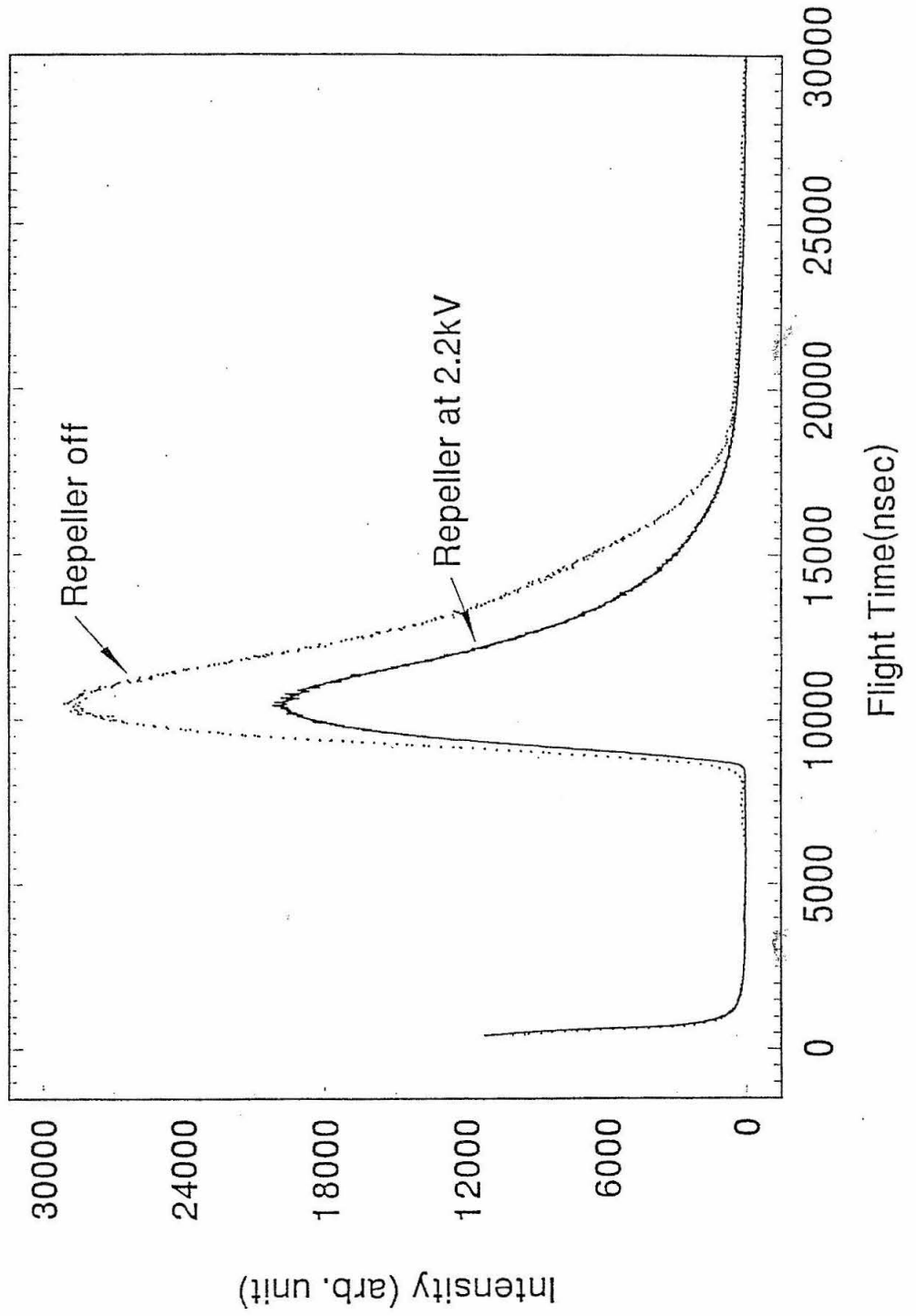


Figure 1-2

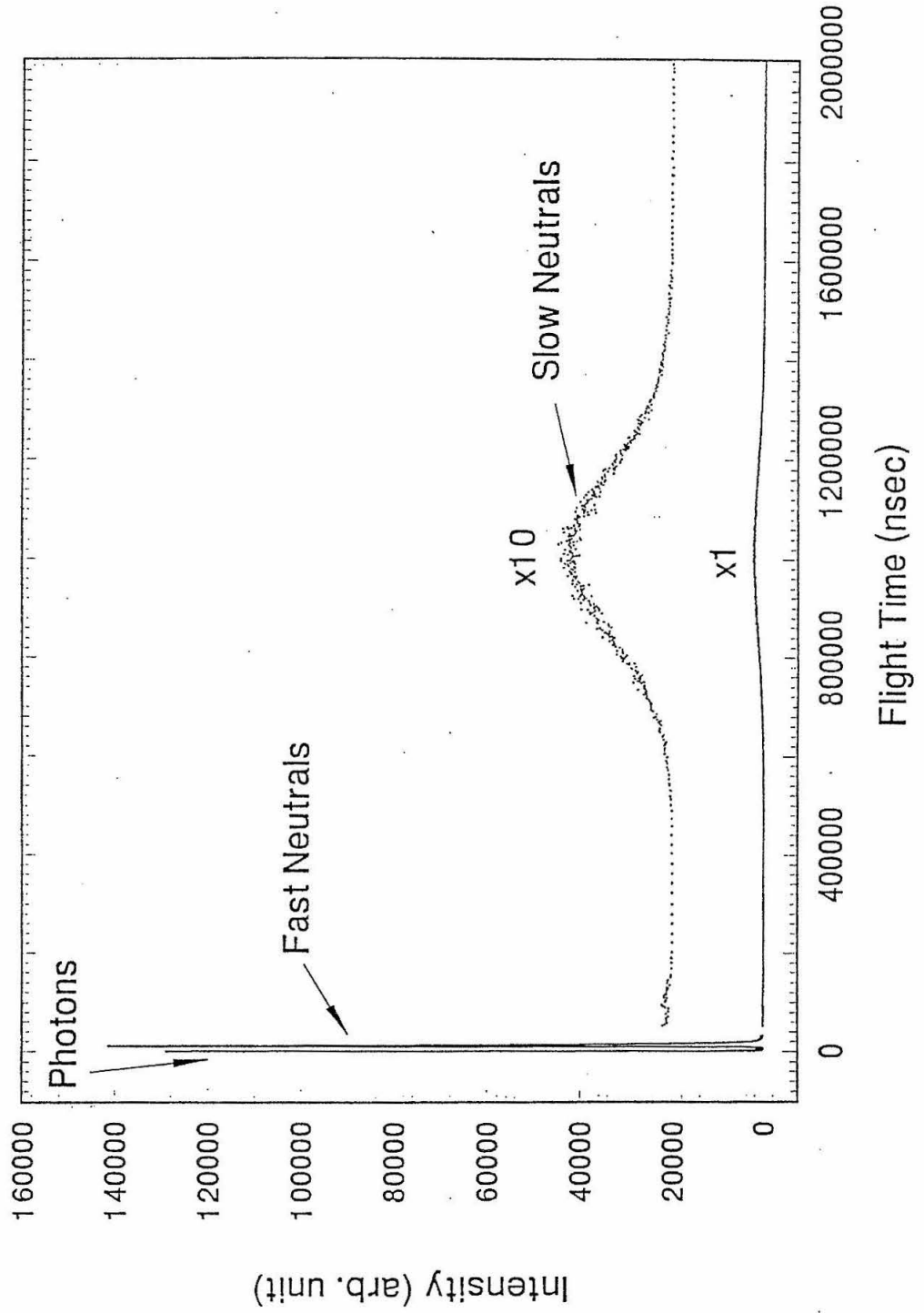


Figure 1-3

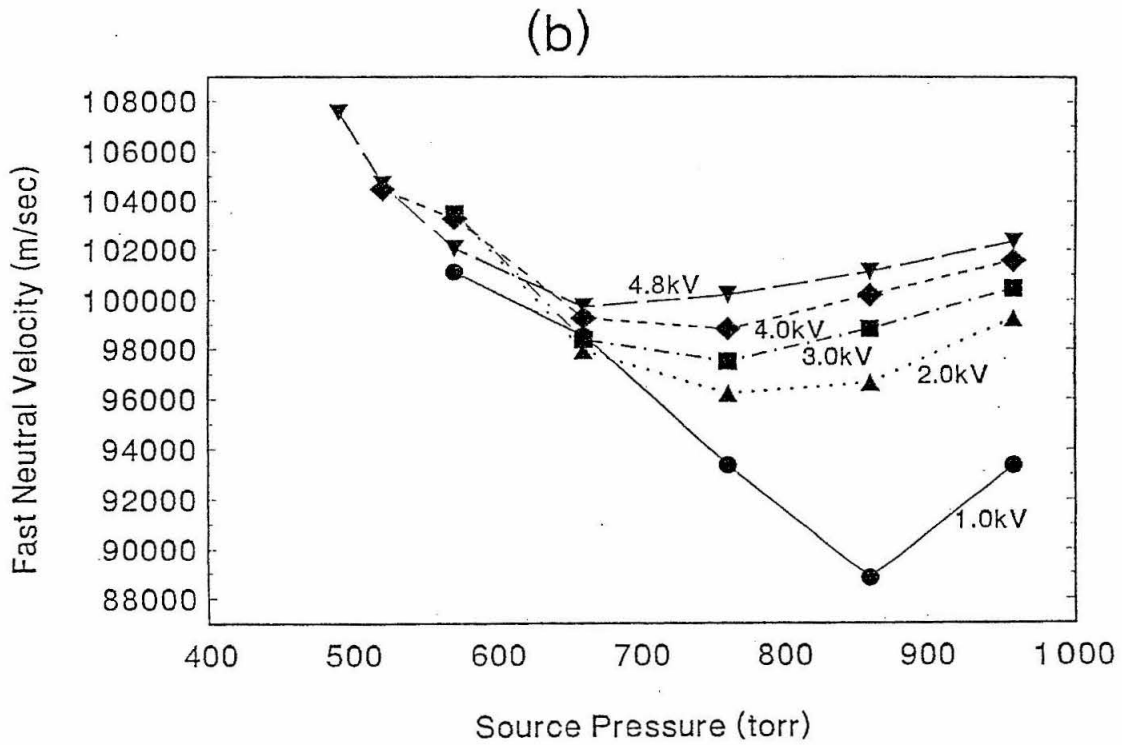
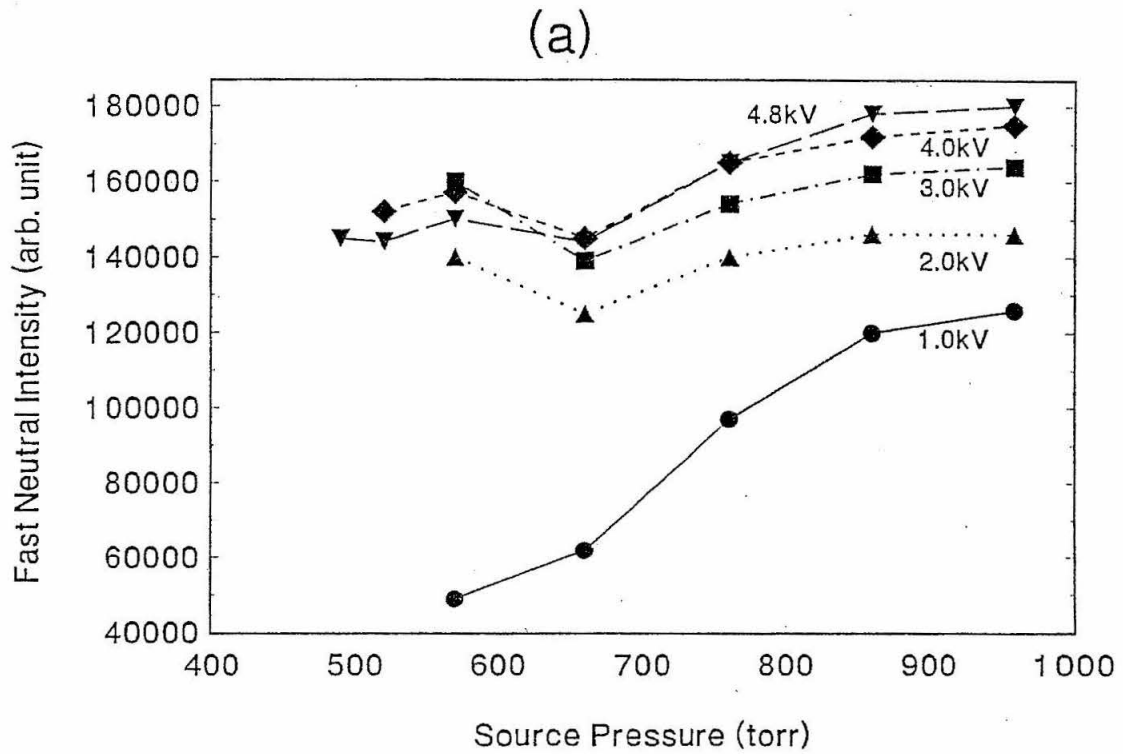


Figure 1-4

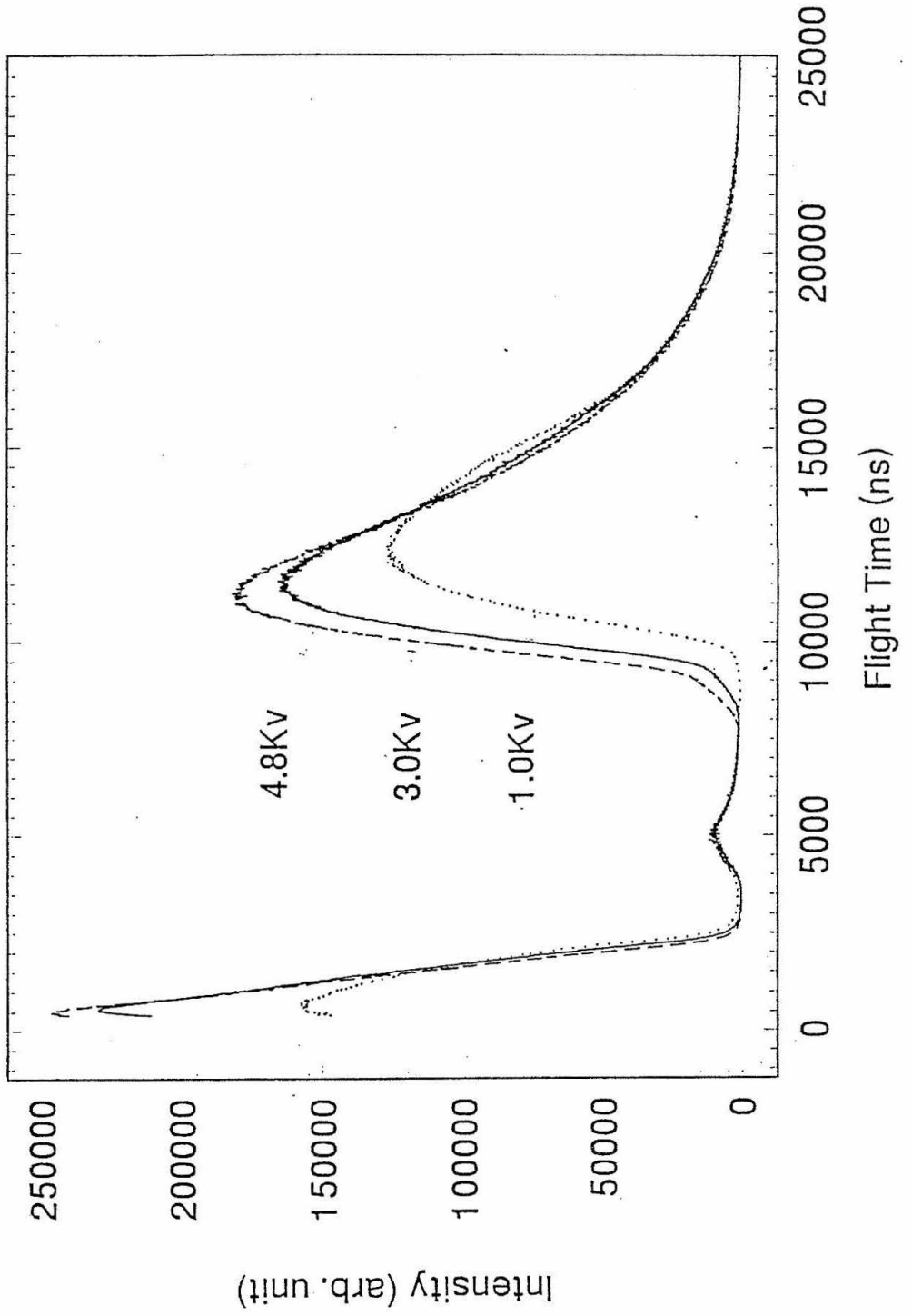
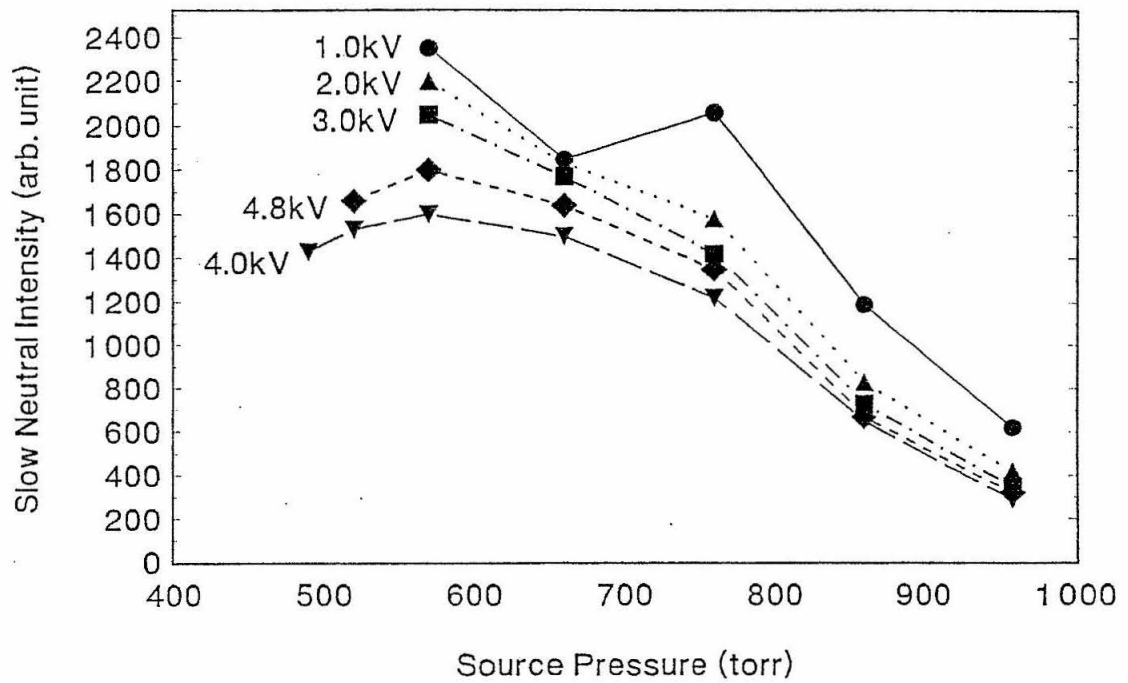


Figure 1-5

(a)



(b)

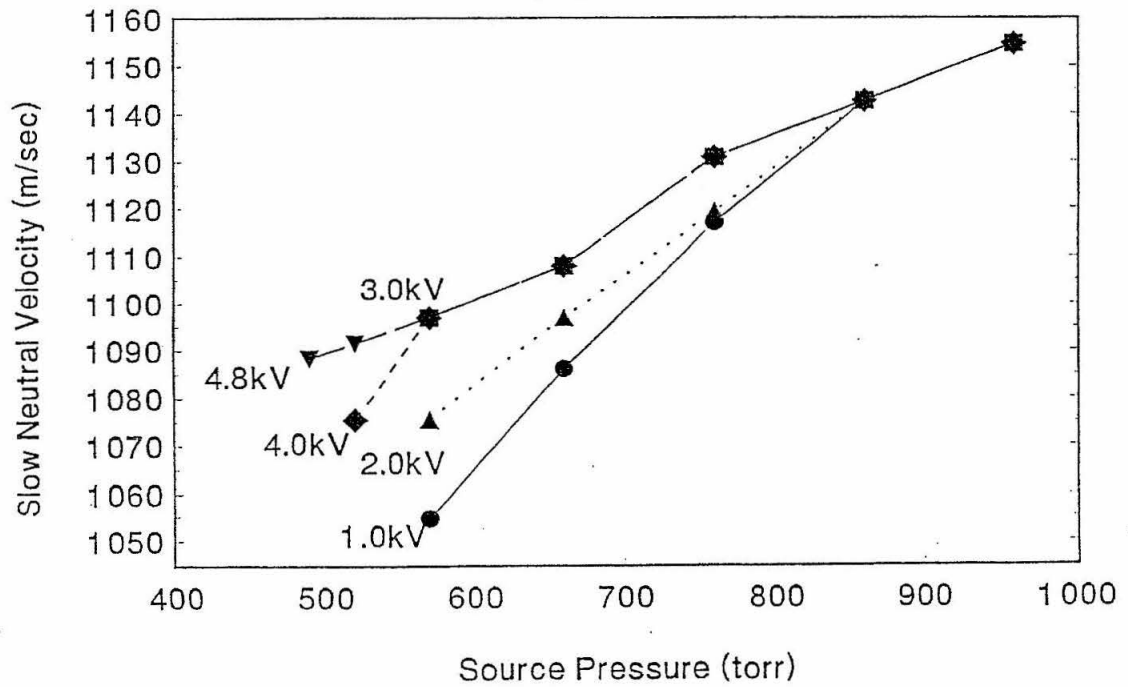


Figure 1-6

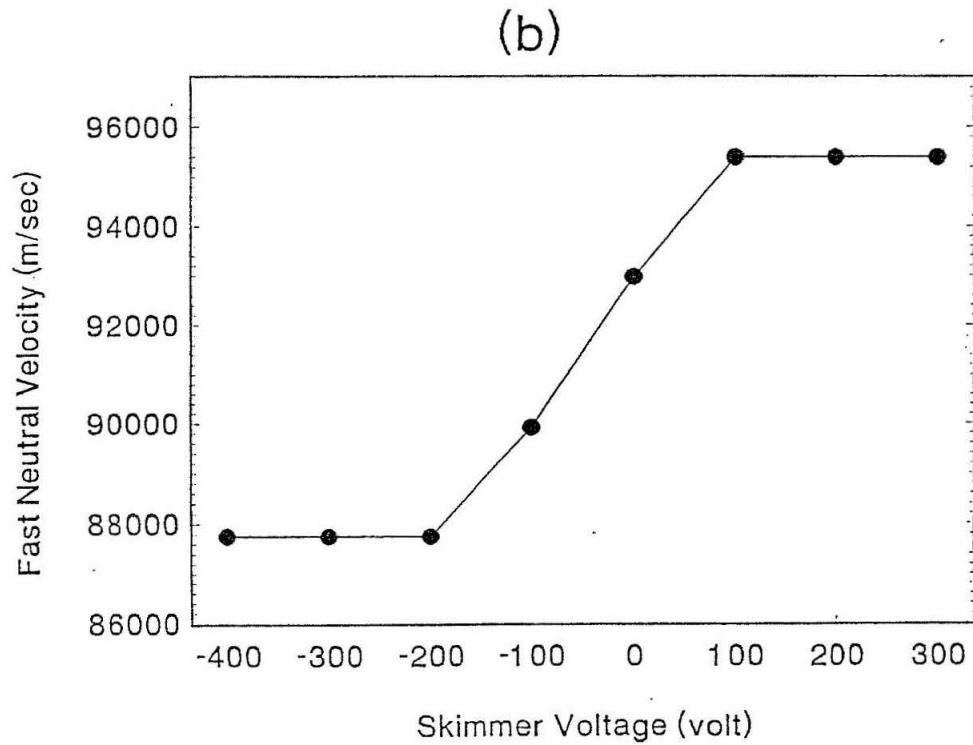
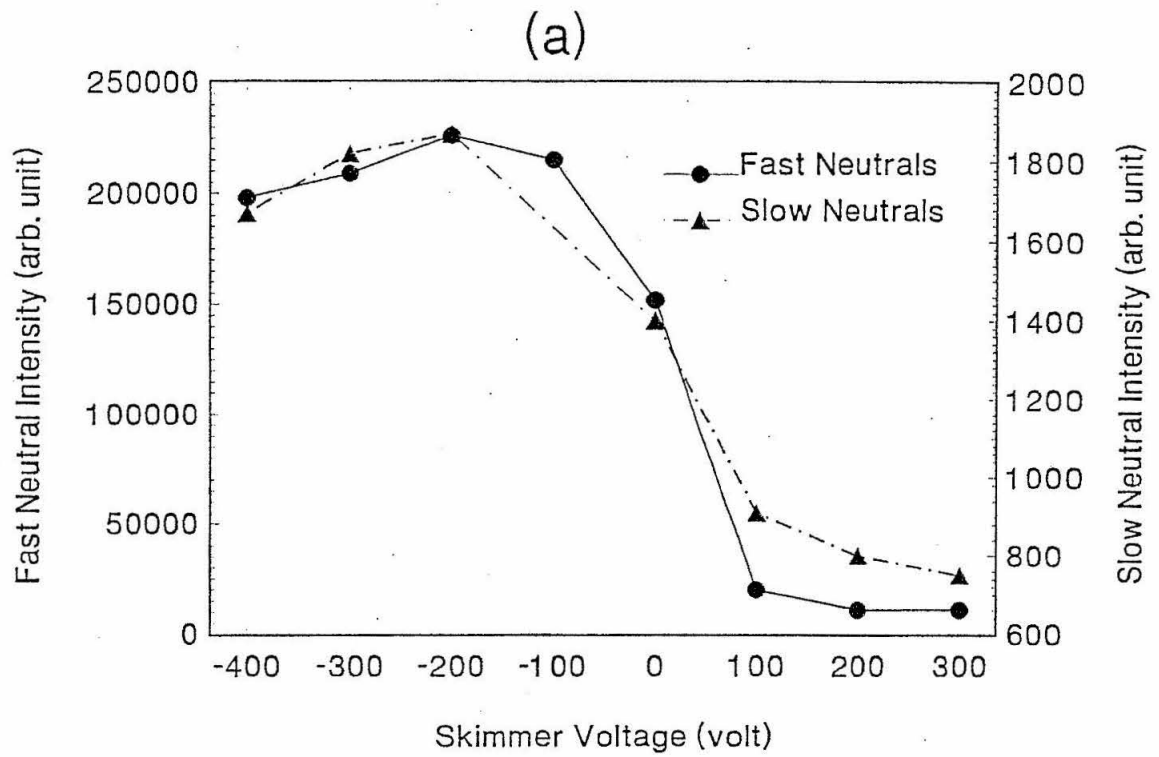


Figure 1-7

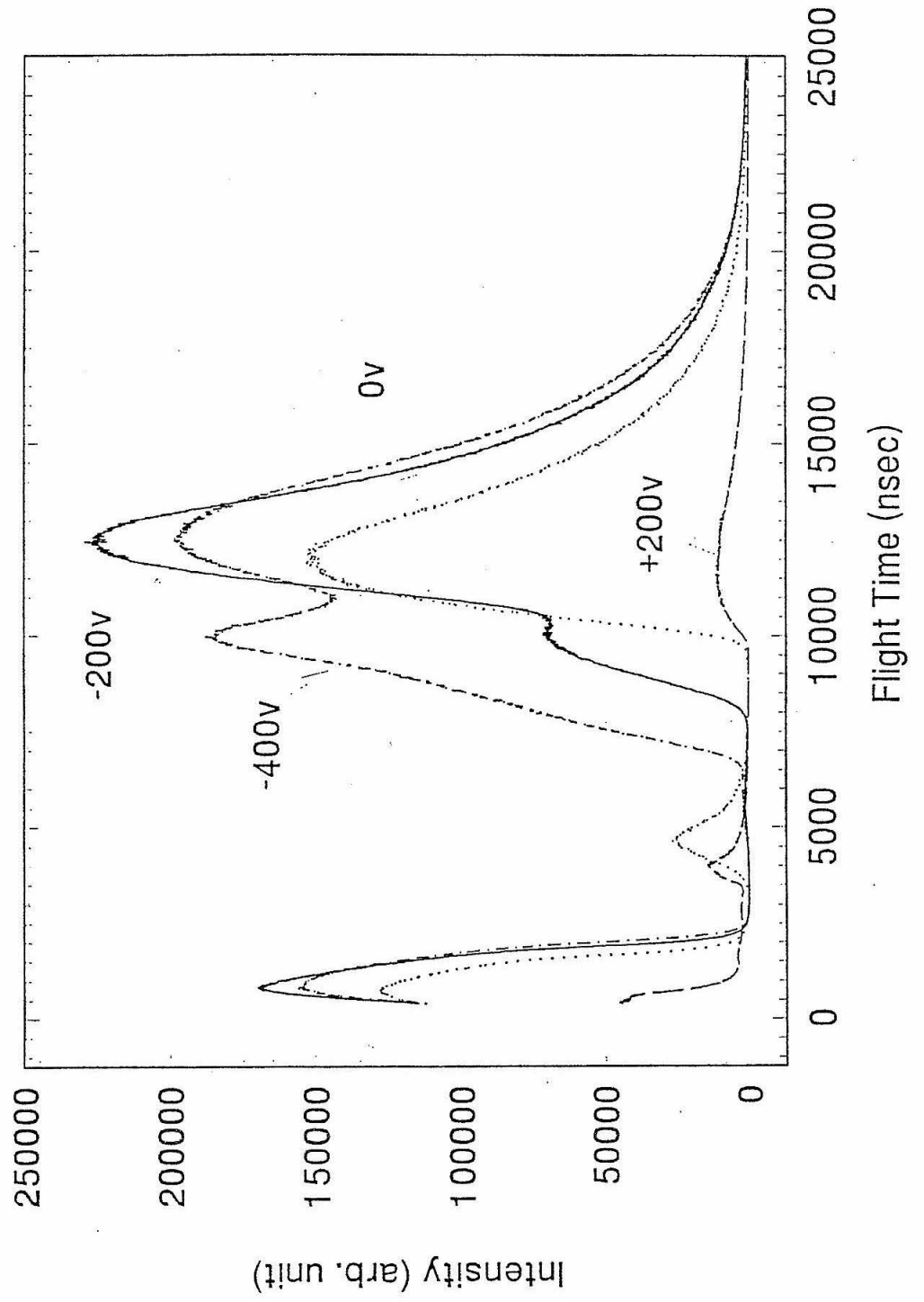


Figure 1-8

Chapter 2

Generation of Charged Helium Droplets by Field Ionization

2. 1. Introduction

Helium clusters and droplets are expected to exhibit novel physics analogous to that observed in the liquid. Charges injected into liquid helium have served as unique probes of elementary excitations in the superfluid. Similarly, charges may provide a method for elucidating the quantum mechanical and coherent properties of helium clusters and droplets. Multi-charged helium droplets¹ are in some ways analogs of multi-electron bubbles² in liquid helium. There have been some theoretical predictions of their properties, but these droplets are not well characterized experimentally. The purpose of the present work is to develop a method for generating a beam of multi-charged helium clusters and droplets. Such a beam could then be applied to study the physics of these particles.

Helium clusters can be produced directly in the vapor phase. In earlier experiments, singly charged species were formed by nucleation around charges introduced into cold vapor.^{3,4} In several recent experimental studies, charged helium clusters have also been produced by generating neutral clusters in a supersonic expansion followed by ionization of the gas phase clusters. Varying the stagnation pressure and temperature behind the nozzle controls the size of the neutral helium clusters. Several methods of ionizing these clusters have been reported: electron bombardment,^{5,6} electron attachment,⁷ and most recently synchrotron radiation.^{8,9} While the supersonic expansion techniques have proved to be very reliable for forming singly charged clusters, multi-charged species possessing more than a few elementary charges have not been reported. Furthermore, the ionic clusters tend to be very small, because the weakly bound van der Waals clusters fragment extensively upon ionization.

Larger multi-charged droplets have been extracted directly from charged liquid helium surfaces by a Rayleigh-Taylor instability mechanism. Boyle and Dahm¹⁰

introduced high charge densities with a beta-emitting source into liquid helium films and extracted droplets into the gas phase with an applied electric field. They reported the formation of gas phase droplets of radius $r = 0.52$ mm and charge $q \sim 10^{-11}$ C. The experiment of Boyle and Dahm was conducted in the temperature range $3.24 \text{ K} < T < 5.13 \text{ K}$, above the lambda point. Volodin and Khaikin¹¹ extended that work by characterizing the surface discharge in superfluid helium at 1.2 K. They measured a threshold of 1900 V/cm above which surface instabilities led to the ejection of liquid jets.

Lo has proposed that multiply charged superfluid helium clusters could be generated by field ionization or field emission of liquid helium II. In this approach, the liquid is charged by applying a high voltage to a sharp tip in the liquid and is then extracted through a nozzle into a vacuum chamber. Field ionization and emission have been elucidated in bulk liquid helium^{12,13} and in liquid helium films.¹⁴ A similar approach, electrostatic spraying, has been applied by Turnbull and coworkers¹⁵ to form charged droplets of other cryogenic liquids such as hydrogen^{16,17} and nitrogen¹⁸.

Of these methods, field ionization charging and electrostatic spray formation of droplets has the most promise for generating beams of multi-charged helium droplets. Direct ionization of liquid helium will yield clusters that are significantly larger and possess higher charge states than clusters formed by ionization of supersonic expansions, while the electrostatic spray methods should generate currents that are orders of magnitude higher than those possible with beta-ray emitting sources.

Here we describe the generation of multi-charged positive liquid helium droplets by field ionization and electrostatic spraying. We discuss the mechanism for droplet formation and compare the observed behavior with that of droplet formation with liquid nitrogen.

2. II. Apparatus

2. II .a. Overview

The apparatus consisted of a cryogenically cooled electrostatic spraying source (Figure 2-1). The source was assembled at the bottom of a modified optical cryostat, which could maintain the source at temperatures as low as 1.8 K. The source was composed of three major parts: the source body, which contained the liquid reservoir, a glass capillary, and a glass droplet cell. Liquid flowed from the reservoir through the capillary and into the droplet cell. The liquid was ionized inside the capillary by a tungsten needle positioned with its tip slightly recessed from the nozzle. Droplets were ejected from the nozzle into the droplet cell, a glass cylinder sealed to the outer face of the nozzle-mount. A metal cap on the opposite end of the glass tube served to seal the droplet cell and to function as a Faraday cup. Droplets formed in the cell were viewed through the glass by a camera coupled to a microscope.

2. II. b. Cryostat

The source was attached to the bottom of a two-stage RMC model CT-610-.1 liquid-helium cryostat. The 4.2 K first stage of the cryostat was designed to be continuously fed with liquid helium. The second stage was a ^4He pot that could be pumped to achieve 1.5 K. The stages were connected through a needle valve, which was designed to regulate the liquid flow. After the needle valve, the tubing was split in two lines, one to the second stage and another to the source.

Three layers of radiation shields surrounded the source to minimize radiative heating. The second and outer shields had glass windows to allow viewing of the source, while blocking some IR radiation. The cryostat was kept inside a diffusion-pumped vacuum chamber maintained at pressures below 10^{-7} Torr.

2. II. c. Source

The source body consisted of a cylindrical disk (3.8 cm in diameter) and a block of dimensions 2.54 cm × 2.54 cm × 1.14 cm machined from a single piece of OFHC copper. The source was mounted to the helium pot with the surface of the cylindrical disk flush with the bottom of the pot. The source chamber consisted of a 1.475 cm in diameter hole bored 5 mm deep into the front face of the block. On the back of the source block there were a high voltage feed-through and two 1.59 mm in diameter stainless steel tubes, one a pump-out line and the other a pressure sensing line. Liquid cryogen was fed from the first stage of the cryostat through a stainless-steel tube (1.59 mm inner diameter) into the source chamber through an inlet opening on the disk.

The source chamber was capped with an invar nozzle-mount, which was sealed to the source body with an indium seal. The nozzle-mount had two holes connecting the front face of the nozzle-mount to the side of the piece, for the pumping and pressure sensing lines. In the center of the nozzle-mount there was a hole for the glass nozzle, which was sealed to the nozzle-mount piece with epoxy. The glass nozzle was formed by heating a glass capillary with a flame, stretching it, and then, after cooling, breaking the tip at the desired inner diameter of 60-80 μm . The tungsten needle ($d = 50 \mu\text{m}$) with a tip of radius $r \approx 0.4 \mu\text{m}$ was inserted into the capillary such that the tip was kept slightly (0-100 μm) recessed from the orifice in order to prevent arcing.

2. II. d. Droplet cell

The droplet chamber consisted of a glass cylinder, 13 mm inner diameter and 15.5 mm in length. Both ends of the cylinder were sealed with indium gaskets. One end was sealed to the invar nozzle-mount and the other to an invar cap.

2. III. Experimental procedure

2. III. a. Overview

A schematic of the experiment is illustrated in Figure 2–2. Liquid helium flowed from the source chamber, through the capillary, and into the droplet cell. Both source chamber and droplet cell were pumped to maintain a pressure difference across the nozzle. As the liquid flowed through the nozzle, the electric field due to the high potential of the needle charged the liquid. The charged droplets were sprayed into the droplet chamber, where they could be observed with a microscope. Total current was measured on a faraday cup.

2. III. b. Temperature control

The first stage of the continuous flow cryostat was maintained at 4.2 K. Liquid helium from the first stage was leaked through a flow regulating needle valve, and then teed off to the second stage of the cryostat, and to the source. On the back of the source, there were one pumping and one pressure sensing tubes, which were connected to a flow control valve followed by a mechanical pump and a MKS 626 absolute pressure transducer, respectively. By controlling the vapor pressure of helium inside the source, the temperature could be varied. The temperature of the source was monitored with a silicon diode in thermal contact with the source body. The diode readout was monitored through a LakeShore model DRC-91C temperature controller. The temperature reading could be verified with the vapor pressure measurement.

2. III. c. Flow control

Liquid flow from the source chamber to the droplet cell was controlled by regulating the pressure difference across the nozzle. There were two stainless steel

tubes connected to droplet cell for pumping and pressure measurement of the droplet chamber respectively. By adjusting the pumping rates from the source and the droplet chamber independently, the pressure drop across the nozzle could be adjusted from negative to positive several hundred Torr (at negative pressure, the droplet cell was at a higher pressure than the source). The differential pressure across the nozzle was measured with a MKS 233B differential baratron. A MKS 250D pressure-controlling unit controlled the pressure difference between source and droplet chamber. The controlling unit drove a flow-controlling valve located on the cell pump out line.

2. III. d. Field ionization

Field ionization was induced by raising the needle to a positive dc potential. Current from a dc power supply passed through a 60 M Ω current-limiting resistor and an ammeter, both in series with the needle. A 200 M Ω to 200 k Ω voltage divider was connected after the 60 M Ω ballast to monitor the discharge on an oscilloscope. The voltage could be raised as high as 12 kV, above which the connectors would arc.

A sharp tip was made by electrochemically etching 50 μm in diameter tungsten wire. Scanning electron microscope (SEM) images (Figure 2-3a) indicated that the needle prior to use had a radius of curvature of 0.4 μm or less. The tip became dull after several hours of operation, as seen in the SEM image in Figure 2-3b. Higher voltages were generally required as tip wear increased. The needle was replaced after each run.

2. III. e. Measurements

The ion current impinging on the Faraday cup (invar cap) was measured with a Keithley model 485 picoammeter. The sensitivity of the ion current measurement was on the order of 1 nA. The invar cap could be raised to high voltages to verify charging by deflecting the charged particles.

The helium droplet formation was recorded with a long-distance microscope (Titan Tool model TZOVA) and a CCD camera (Cohu model 4110) which provided spatial resolution of up to 2 μm . The droplet was backlit by an AMETEK (model 1967) strobe, which could be operated from 1 to 30000 flashes per minute.

2. III. f. Liquid nitrogen experiments

The liquid nitrogen experiments were performed in the same apparatus using a similar procedure. With nitrogen as the coolant, the temperature ranged between 67 to 77 K, depending on the pressure maintained in the source. Our objective was to provide a benchmark for comparing the liquid helium results with the electrostatic spraying behavior of other cryogenic liquids observed previously. The experiment was similar to that of Woosley *et al.*¹⁸, except that in their apparatus the capillary and fluid flow were directed vertically downward.

2. IV. Results

2. IV. a. Liquid helium

Three variables were changed independently to study the field ionization process: the source temperature, the pressure difference across the nozzle, and the

needle voltage. Liquid helium ionization was characterized at three temperatures: 1.8, 2.2, and 3.5 K. At each temperature, pressure difference and voltage were independently varied to produce different spraying conditions. At 2.2 K two distinct flow modes were observed, depending on the pressure difference across the nozzle. The measurements at 3.5 K were intended to characterize the electric discharge at higher temperatures. Measurements below the lambda transition point of helium were performed at 1.8 K.

2. IV. a. 1. Temperature = 2.2 K

At 2.2 K and at pressure differences across the nozzle of less than 2 Torr, liquid flowed slowly out of nozzle and wetted the outside of the capillary. Large drops ($r > 0.5$ mm) formed either on the tip or on the lower side of the capillary, as seen in Figure 4a. The drops occasionally burst due to fluctuations of the pressure difference, which were on the order of 0.5 Torr. Once voltage was applied to the needle, the drop on the nozzle tip grew. If the drop was hanging on the side of the capillary, it moved to the front of the capillary tip. Upon applying voltages of 2–4 kV (depending upon needle condition), the drop exploded into a shower of charged particles (Figure 2–4b). Since pressure fluctuations ($\geq 25\%$) were relatively high, no data was acquired in this pressure difference regime.

When the pressure difference across nozzle was greater than 2 Torr, we observed a steady jet of liquid streaming out of the source (Figure 5a). The application of voltage to the needle did not affect the jet until a threshold was reached. At the threshold, which ranged from 1.75 to 3.25 kV depending on needle tip condition, a “shower-like” explosion appeared in the jet (figure 5b) and ~ 100 nA of ion current were detected on the Faraday cup. The explosion expanded radially from the centerline of

the jet, as seen in Figure 5b. The smallest droplets that could be identified from the images were of the order of 1–10 μm in diameter.

A weak, highly localized glow was observed on the needle tip at these high currents, characteristic of a glow discharge. Parts of the glass nozzle were also found to glow. The weak glows on the glass were only seen when the room lights in the laboratory were turned off. By further increasing the voltage ~ 1 kV above the ionization threshold, arcing would occur. The highest stable ion current was about 400 nA. If the voltage was reduced after entering the glow regime, the high ion current remained until a cut off of 0.5-1 kV below the original threshold.

The liquid helium explosions in the glow regime were always pulsed, as seen in figure 5b. We often observed several bursts in sequence within a single camera frame. The rate of pulsing increased as the voltage increased. However, no pulsing of the discharge voltage was observed when monitored on the oscilloscope. By examining a large number of sequences and from the calculated flow rate, we estimated that the pulse period was of the order of 1–30 μs .

We were able to deflect the trajectories of the particles by applying a high voltage potential ($V = \pm 900$ V) to the Faraday cup, which was located 0.7–1.0 cm from the needle tip. Figure 2–6a shows an explosion with no voltage on the cap. Applying a positive potential on the Faraday cup reflected the particles, which were scattered within the droplet chamber (Figure 2–6b). Negative potentials tended to destabilize the jet by accelerating the jet towards the plate. This enhanced acceleration led to fluctuations on the surface of the jet (Figure 2–6c).

Further increase in the needle potential, above the glow regime, increased the ion current until an arc occurred between the needle tip and the cap or nozzle-mount.

The arc led to a violent explosion of the liquid, followed by cessation of flow. The voltage had to be reduced before the flow of liquid helium was reestablished. The arc was characterized by much higher currents (on the order of 10 μA) with large fluctuations, on the order of 1 μA .

2. IV. a. 2. Temperature = 3.5 K

At 3.5 K and $\Delta P = 5$ Torr, a higher threshold potential (8–10 kV) was required to create the same sudden increase in ion current and shower-type explosion effects that were observed at the lower temperature of 2.2 K. Several runs were performed at both temperatures to confirm that the increase in threshold voltage was not due to erosion of the needle tip.

2. IV. a. 3. Temperature = 1.8 K

At a source pressure of 11 Torr, the liquid helium equilibrium temperature is approximately 1.8 K, which is ~ 0.4 K below the lambda point of helium. We observed that against a negative pressure gradient ($\Delta P = -4.0 \pm 0.5$ Torr) liquid helium flowed out the nozzle and wetted the glass surface with voltage off (Figure 2–7a). Above $V \sim 2$ kV, the liquid was driven out of the nozzle in the form of large droplet ($r > 100 \mu\text{m}$). The droplets were irregular in shape (Figure 2–7b), indicating that the droplet surface was highly unstable in the presence of charges. In contrast to the experiments above 2.2 K, no shower-explosion behavior was observed at this temperature.

2. IV. b. Liquid nitrogen

The liquid nitrogen experiments were conducted at $T = 70 \pm 1$ K. Liquid nitrogen displayed a low-flow mode at small pressure differences ($\Delta P < 25$ Torr), and a jet mode at large pressure differences ($\Delta P > 25$ Torr).

2. IV. b. 1. Low-flow conditions

At pressure differences of 15-25 Torr across the nozzle, liquid nitrogen wetted the capillary when no voltage was applied, as depicted in Figure 2–8a. By applying a high voltage to the needle, a stable liquid nitrogen drop formed around the nozzle capillary (Figure 2–8b). The drop induced by the electrostatic force increased in size as the applied voltage increased. Drops as large as 0.5 mm in radius were formed with needle voltages of 9 kV, above which fragmentation would occur. At voltages higher than 5 kV, the droplet started to distort by forming a wide conical tip, and a protuberance appeared at the tip of the drop. Surface oscillations of the drop were observed, but were insufficient to cause fragmentation. Above 9 kV, depending on needle conditions, the protuberance broke loose from the large stable drop to form a thin jet of liquid (Figure 2–8c).

2. IV. b. 2. Jet flow

At pressure differences between 35 and 50 Torr and $V = 0$ to 5 kV, a jet of liquid flowed from the nozzle. After a certain length, the jet broke into a sequence of droplets with the jet length depending on the pressure difference (Figure 2–9a depicts such a pressure-driven jet of liquid nitrogen, with the voltage off). At needle voltages higher than 5 kV, we observed the effects of charged-induced instability: the length for

breakdown of the jet into droplets was shortened, and the size of the droplets decreased (Figures 2–9b and 2–9c), in accordance with the observations of Turnbull and co-workers.¹⁵ A Taylor cone was clearly observable in front of the nozzle tip. Typically, the jet diameter was about 50 μm and the droplets, which broke up from the jet one at a time, had sizes ranging from 100 to 250 μm in diameter, depending on the applied voltage. In contrast to the irregular shape of charged liquid helium II droplets, liquid nitrogen droplets were close to spherical. The current measured on the Faraday cup was approximately 3 nA. At very high voltages ($V > 10$ kV), arcing from the needle to the source body was observed. Arcing usually led to chaotic behavior of the jet and to currents of several μA .

2. V. Discussion

2. V. a. *Electrostatic spraying*

The charging of liquid helium and nitrogen was evident when a voltage was applied to the needle. Even at relatively low voltages, wetting of the glass capillary was inhibited (most likely due to charging of the glass surface) and a “stable” droplet formed on the nozzle tip. At higher voltages, droplet formation was induced and measurable currents were collected for both liquids; however, the behavior of helium and of nitrogen were different. In the case of helium, we observed pulsed explosions of liquid droplets or jets into showers of fine droplets. Charging of the droplet fragments was verified by observing their deflection upon applying a voltage potential to the collecting cap. The electro-spraying of nitrogen was characterized by the formation of a Taylor cone at the nozzle tip. Instabilities of the cone led to breakup of the jet into single charged particles several hundred microns downstream of the nozzle.

The instabilities of electrified jets and droplets were studied as early as 1882 by Lord Rayleigh.¹⁹ By considering the balance of surface tension and coulomb repulsion, Rayleigh derived an equation to predict the maximum charges sustainable on a droplet or on a cylindrical jet, above which instabilities lead to breakup. In the case of the cylindrical jet, Rayleigh obtained the following equation:

$$(q/l)_{\text{RL}} = (6 \pi^2 \gamma \epsilon_0 a)^{1/2}, \quad (2-1)$$

where γ is the surface tension of the liquid, a is the diameter of the cylindrical jet, ϵ_0 is the electric permittivity of medium surrounding the jet, and $(q/l)_{\text{RL}}$ is the Rayleigh charge limit per length of the jet. Empirically, it has been found that breakup of a charged cylindrical jet will occur at or below the Rayleigh limit.²⁰

In order to compare with the Rayleigh limit for liquid helium and liquid nitrogen under our experimental conditions, we had to estimate the charge per unit length. This quantity was predicted from the ratio of the observed current to the flow rate:

$$(q/l)_{\text{exp}} = \frac{I}{Q} \frac{\pi a^2}{4} \quad (2-2)$$

We measured the current I , but were unable to directly measure the liquid volumetric flow rate Q , which we therefore computed numerically. Because the dimensions of the capillary were narrow (the inner diameter of the capillary tapered from 450 μm to 70 μm with a 50 μm wire inside), viscous forces dominated flow. The estimated Reynolds number was on the order of 10^6 , and we therefore treated the flow as laminar. By modeling the nozzle as an annulus with exponentially contracting outer wall (glass inner

diameter) and straight inner wall (needle diameter), we were able to numerically calculate the flow rate. The equation for the pressure drop of laminar flow in an annulus is

$$\Delta P = \frac{8\mu Q \Delta L}{\pi(R)^4} \left[\frac{1 - \kappa^4}{\ln(\kappa^{-1})} - \frac{[1 - \kappa^2]^2}{\ln(\kappa^{-1})} \right]^{-1}, \quad (2-3)$$

where ΔP is the pressure drop across a length ΔL , μ is the viscosity, Q is the flow rate, R is the radius of the glass nozzle, and κ is the ratio of the outer wall diameter to the inner wall diameter. The flow equation was solved by difference. In the numerical routine the nozzle was divided into infinitesimal sections, and the pressure drop was calculated for each segment from equation (2-3). The pressure was summed over all sections and compared to the experimentally set pressure difference across the nozzle. The flow rate was iterated until the total pressure drop converged to the experimentally measured pressure difference.

Results are tabulated in Table 2-1. We find that in our experiments the liquid helium jets have charge densities ~ 50 times greater than the Rayleigh limit. In contrast, the experimental charge per length for the liquid nitrogen jets is comparable in magnitude to the computed Rayleigh limit. These results are consistent with, and provide an explanation for, the experimental observations. We would expect that any helium jet of dimension 100 μm would undergo coulomb explosion, fragmenting into many small droplets and that a Taylor cone would not be observed. On the other hand, the surface charging of liquid nitrogen jets is of the critical magnitude to affect jet stability; thus, we would expect to observe droplets formed from Rayleigh-Taylor instabilities.

In the case of liquid nitrogen, the greater surface tension of the liquid (see Table 2–1) balances the repulsion between the surface charges, allowing the formation of a stable drop of order 0.5 mm on the nozzle tip. By increasing the voltage one can visually observe the propagation of instabilities on the liquid surface, the formation of a protuberance, and the breakage of the jet into droplets.

The Rayleigh limit as calculated above is a simple model for the charge of a stationary cylinder. It does not account for the stabilization or destabilization effects induced by the acceleration of the jet due to the electric field of the needle or fluid motion. Turnbull²¹ has studied surface instabilities of electrified jets of insulated liquids with a more detailed model. He introduces a first-order perturbation onto the equations of motion, continuity, and electric potential for an equilibrated liquid jet in order to simulate jet instabilities (growth rate of perturbations) as a function of the wavelength of the surface oscillations. Turnbull identifies the charge density on the surface of the jet, and the presence of a tangential field along the jet, due to the electric field of the needle, as the main effects leading to stabilization or destabilization of the jet. For short wavelengths oscillations ($\lambda \sim 2\pi r$, where r is the jet radius), which we observe in our nitrogen jets, the model developed by Turnbull indicates that the tangential electric field tends to stabilize the jet surface while the surface charge destabilizes the jet. Taken together, both surface charging and tangential fields stabilize short wavelength oscillations because they produce a shear force in the direction of the jet. In contrast, our observations show that by applying a voltage to the jet, there is a reduction in jet length. This indicates that we are in a regime where destabilization of the jet by the surface charge is more effective than stabilization by the tangential field.

In the case of liquid helium, since the charge density far exceeds the Raleigh limit, explosions occur at the point of charge injection. A long wavelength ($\lambda \geq r$)

hydrodynamic analysis of jet instabilities such as Turnbull's is no longer valid. The coulomb repulsion effect dominates the surface tension term and leads to explosion of the jet into several smaller droplets ($r < 10 \mu\text{m}$). Two main factors contribute to the dramatic differences between helium and nitrogen: the very low surface tension of liquid helium, about two orders of magnitude smaller than that of nitrogen, and the higher current observed in helium, about two orders of magnitude larger than that observed in nitrogen. The heat dissipated into the jet may also play a role in the abrupt explosion of helium. We estimate an upper limit on the average electrical power dissipated at the needle of $I \times V \sim 0.4 \text{ mW}$, which is sufficient energy to vaporize liquid helium at the flow rates we observe.

The coulomb explosions we observe in helium are of a regular pulsed nature. However, there is no evidence of pulsing behavior from the waveform of the high voltage supplied to the needle. We also observe glowing at the needle and on one or more points on the glass tip while ionization takes place. These observations suggest that ionization may be occurring both at the needle tip and at charged points on the glass surface.

2. V. b. Field ionization mechanism of charging

Field emission and field ionization of cryogenic liquids (He, H₂, N₂, O₂, and Ar) have been studied by Gomer and Halpern using a point-to-plane field emission tube.^{12,13} Our results were similar to those obtained by Gomer and Halpern in the existence of a sharp onset, ($V = 1.3 \text{ V/\AA}$ in Gomer's work) at which currents of the order of μA set in. They also observed self-sustaining discharges when the voltage was reduced until a sharp cutoff ($V = 0.64 \text{ V/\AA}$ in Gomer's work).

The electrical breakdown of liquid helium^{22,23,24} and other cryogenic liquids^{25,26} have been extensively studied by research groups interested in the dielectric properties of helium and other cryogenic liquids as insulators. In these studies, however, little attention was given to the mechanism of ionization.

2. V. b. 1. Higher currents in liquid helium

The model presented by Gomer and Halpern describes field ionization in terms of electron tunneling from the atom to the electrode. In their experiments, they observed currents from discharges in liquid helium higher than those for other cryogenic liquids. They explained the higher current in liquid helium in terms of the possibility of ionizing avalanches, the higher mobility of ions in liquid helium, and the formation of gas bubbles.

The greater probability of charge multiplication (avalanching) presents an explanation for the higher current in helium. Charge multiplication can take place in the liquid through ion impact ionization when the ions are allowed to obtain enough translational energy before colliding. In liquid nitrogen, some kinetic energy of the accelerated ions can be converted into vibrational and rotational modes of the liquid molecules through inelastic collisions. This energy conversion mechanism impedes the ions of reaching sufficient kinetic energies for ion impact ionization within one mean free path. Helium ions, on the other hand, are much hotter because of the lack of energy quenching mechanisms. The higher current in helium can also be explained in terms of the ion mobility. Gomer measured helium and nitrogen ion mobilities and found that helium ion had a mobility ten times higher than nitrogen ion.²⁷

The lower heat of vaporization of helium (~ 50 times lower than for nitrogen) can also be related to the higher current measured in helium. The energy associated with

the hot ions can create low-density bubble sites. Avalanching followed by discharging occurs when the bubbles grow to a certain size limit, at which the free length is sufficient for ions to create multiple charging. Since the heat of vaporization is lower, formation of bubbles in liquid helium is more likely.

2. V. b. 2. Temperature dependence

The temperature dependence of helium I discharges can be understood in terms of the bubble mechanism. Gerhold, in his study of dielectric breakdown of cryogenic gases and liquids, has pointed out that during bubble formation the dielectric strength decreases rapidly from that of the liquid to that of the vapor until the Paschen minimum is reached, where breakdown takes place. The discharge inside a bubble is therefore similar to a gas phase discharge. The dielectric strength of saturated helium vapor increases by a factor of ~ 7 from 2.2 K to 3.5 K.^{22,28} This change in dielectric strength may in part explain why the threshold voltage is higher at 3.5 K than 2.2 K.

2. V. c. Superfluid helium

We have obtained preliminary results on the charging of superfluid helium at 1.8 K flowing against small negative pressure gradients. The behavior of superfluid helium differs markedly from normal helium at 2.2 K. In the absence of an electric field, the flow of superfluid helium through the capillary against a pressure gradient is a manifestation of the well-known "Fountain Effect" of helium II. This mass transport results from the flow of the Bose condensate to compensate for entropy differences between thermodynamic states of the liquids on each side of the capillary. This superleak of helium II continuously drives liquid out of nozzle until the chemical potentials are balanced across the nozzle. Since the surface tension is low for

superfluid helium, we observe wetting on the capillary exterior and the formation of large, stationary drops on the capillary tip.

With modest electrical potentials (2 kV on the needle), a jet emerges due to the presence of charges on the jet and the electric field from the needle. We observe hydrodynamic Rayleigh-Taylor instabilities leading to the formation of large droplets ($r > 100 \mu\text{m}$) of irregular shape, in contrast to the coulomb explosions and formation of fine particles seen at 2.2 K.

The observation of Rayleigh-Taylor instabilities instead of coulomb explosion suggests that the surface charge density in the present case is much lower than in the case of jets of normal liquid helium, despite the fact that field ionization currents tend to be higher at lower temperatures. This qualitative difference can readily be explained if the helium is below the superfluid transition. In this case, the superfluid component of the helium II will exhibit inviscid flow. The “superleak” through the capillary leads to liquid flow rates that can be orders of magnitude greater than the viscosity-limited flow of normal helium. The higher flow rates would significantly reduce surface charge densities for a given current. However, we did not measure the current in these preliminary experiments and therefore cannot estimate the surface charge densities. The irregular shape of the droplets can also be taken as evidence for superfluidity. Helium II is characterized by a lower surface tension, which leads to the irregular shape of the droplets in the jet.

2. VI. Conclusions

We have generated positively charged droplets by field ionization of liquid helium using an electrostatic spraying apparatus. A comparison of these results with those on liquid nitrogen indicates a qualitative difference in the respective mechanisms of droplet

formation. We have found that electrostatic spraying of liquid helium at 2.2 K results in a coulomb explosion forming a spray of fine droplets with currents of 0.1–0.4 μA , two orders of magnitude greater than currents detected for liquid nitrogen. Electrical breakdown occurs at ≈ 2 kV for helium, significantly less than the voltages (≈ 8 kV) required for liquid nitrogen. Ionization of liquid nitrogen, like insulating cryogenic liquids such as hydrogen and argon, exhibits classic Rayleigh-Taylor instability. Charging leads to the formation of a Taylor cone or jet; droplets with dimensions similar to the jet are formed sequentially downstream by instabilities.

The difference between the behavior of liquid helium and liquid nitrogen lies in the much higher currents obtained from field ionization in liquid helium. The resulting surface charge density greatly exceeds the Rayleigh limit for jets of dimension $a \approx 100$ μm . The observed coulomb explosions in liquid helium are a direct consequence of the excess in surface charge density.

2. VII. References

1. G. A. Williams and M. M. Salomaa, *J. Low Temp. Phys.* **57** 539 (1984).
2. M. M. Salomaa and G. A. Williams, *Phys. Rev. Lett.* **47** 1730 (1981).
3. G. Akinci and J. A. Northby, *Phys. Rev. Lett.* **42** 573 (1979).
4. P. Hautojarvi, K. Rytsölä, P. Tuovinen, A. Vehanen and P. Jauho, *Phys. Rev. Lett.* **38** 842 (1977).
5. J. Gspann and H. Vollmar, *J. Low Temp. Phys.* **45** 343 (1981).
6. H. Buchenau, J. P. Toennies and J. A. Northby, *J. Chem. Phys.* **95** 8134 (1991).
7. J. A. Northby, C. Kim and T. Jiang, *Physica B* **197** 426 (1994).
8. M. Joppien, R. Muller and T. Möller, *Z. Phys. D* **26** 382 (1993).
9. R. Fröchtenicht, U. Henne, J. P. Toennies, A. Ding, M. Fieber-Erdmann and T. Drewello, *J. Chem. Phys.* **104**, 2548 (1996).
10. F. P. Boyle and A. J. Dahm, *J. Low Temp. Phys.* **23** 477 (1976).
11. A. P. Volodin and M. S. Khaikin, *JETP Lett.* **30** 572 (1979).
12. B. Halpern and R. Gomer, *J. Chem. Phys.* **51** 1048 (1969).
13. B. Halpern and R. Gomer, *J. Chem. Phys.* **51** 1031 (1969).
14. B. Halpern and R. Gomer, *J. Chem. Phys.* **51** 5709 (1969).
15. K. Kim and R. J. Turnbull, *J. Appl. Phys.* **47** 1964 (1976).
16. J. P. Woosley, R. J. Turnbull and K Kim, *IEEE Trans. Ind. Appl.* **IA-18** 314 (1982).
17. J. P. Woosley, R. J. Turnbull and K Kim, *J. Appl. Phys.* **64** 4278 (1988).
18. J. P. Woosley, and R. J. Turnbull, *Rev. Sci. Instrum.* **48** 254 (1977).
19. L. Rayleigh, *Philos. Mag.* **14** 184 (1882).

20. When Q/I exceeds the Rayleigh limit, breakdown or Coulomb explosion occurs.
21. R. J. Turnbull, *IEEE Trans. Ind. Appl.* **28** 6 1432 (1992).
22. J. Gerhold, *Cryogenics* **12** 370 (1972).
23. J. Gerhold, *IEEE Trans. Elect. Ins.* **24** 155 (1989).
24. C. Blank and M. H. Edwards, *Phys. Rev.* **119** 50 (1960).
25. J. Gerhold, *Cryogenics* **19** 571 (1979).
26. H. M. Jones and E. E. Kunhardt, *J. Phys. D* **28** 178 (1995).
27. R. Gomer, *Acct. Chem. Res.* **5** 41 (1972).
28. W. Keller, *Phys. Rev.* **97** 1 (1955).
30. E. K. William, *Helium-3 and Helium-4* (New York: Plenum Press) 1969.
31. D. R. Lide, *CRC Handbook of Chemistry and Physics* 71st edn (CRC Press) 1990-91.

TABLE 2-1 Comparison of the charge per unit length for He and N₂ (C/m) computed for the experimental source conditions (equation 2-2), and the Rayleigh limits (equation 2-1). The calculated flow rate and velocity and some relevant physical properties are also included.

	$q/_{EXP}$	$q/_{RL}$	$q/_{EXP}/q/_{RL}$	Q	v	Viscosity	Surface tension
	(experimental)	(Rayleigh limit)	(ratio)	(m ³ /s)	(cm/s)	(μPa/s)	(N/m)
He	1×10^{-7}	2×10^{-9}	50	2.7×10^{-9}	70	3.85 ^{a)}	3.301×10^{-4} ^{b)}
N ₂	9×10^{-9}	1×10^{-8}	1.1	3.1×10^{-10}	8.0	203.9 ^{b)}	1.053×10^{-2} ^{b)}

a) Ref. 30

b) Ref. 31

TABLE 2-1

2. VIII. Figure captions

Figure 2-1 Detailed schematic of the source, droplet cell and cryostat.

Figure 2-2 Schematic of the apparatus.

Figure 2-3 Scanning electron microscope images of typical tungsten tips. (a) An etched tip prior to use. The radius of the tip is approximately $0.4 \mu\text{m}$. (b) A tip after a single run in liquid helium.

Figure 2-4 Liquid helium at $T = 2.2 \text{ K}$, $\Delta P = 2 \text{ Torr}$. (a) No voltage applied to the needle tip. A drop clinging to the capillary is apparent. The burst of fluid emerging from the nozzle is induced by pressure fluctuations. (b) $V = 2 \text{ kV}$. A spray of fine charged droplets is observed. The drop on the capillary exterior has shrunk.

Figure 2-5 Liquid helium at $T = 2.2 \text{ K}$, $\Delta P = 5 \text{ Torr}$. (a) No voltage applied to the needle. A stable jet with a diameter of $130 \mu\text{m}$ emerges from the nozzle. (b) $V = 2 \text{ kV}$. A pulsed coulomb explosion is apparent.

Figure 2-6 Effect of charging the Faraday cup. $T = 2.2 \text{ K}$, $\Delta P = 5 \text{ Torr}$, and $V = 2.5 \text{ kV}$. (a) No voltage is applied to the Faraday cup. The jet surface is relatively smooth and there is no sign of deflected particles. (b) $V_{\text{Fc}} = +900 \text{ V}$ is applied to the Faraday cup. The droplet fragments are deflected back and scattered. (c) $V_{\text{Fc}} = -900 \text{ V}$ on the Faraday cup. The charged droplets are accelerated toward the cup and instabilities on the jet surface are produced.

Figure 2-7 Droplet formation in He II. $T = 1.8 \text{ K}$, and $\Delta P = -4 \text{ Torr}$. (a) $V = 0 \text{ V}$, (b) $V = 1.75 \text{ kV}$. Large, irregularly shaped droplets ($200\text{-}300 \mu\text{m}$) are formed.

Figure 2-8 The effect of charge on liquid N₂. $T = 70$ K, $\Delta P = 20$ Torr. (a) $V = 0$ V. Wetting of the capillary is observed. (b) $V = 5$ kV. The drop bound to the tip expands and a Taylor cone is seen. (c) $V = 10$ kV. A small jet is ejected.

Figure 2-9 The effect of charge on liquid nitrogen spraying, $T = 70$ K, $\Delta P = 40$ Torr. (a) No voltage is applied to the needle. (b) $V = 5$ kV. (c) $V = 8$ kV. The jet length is shortened and the droplets become slightly smaller as the needle voltage is increased.

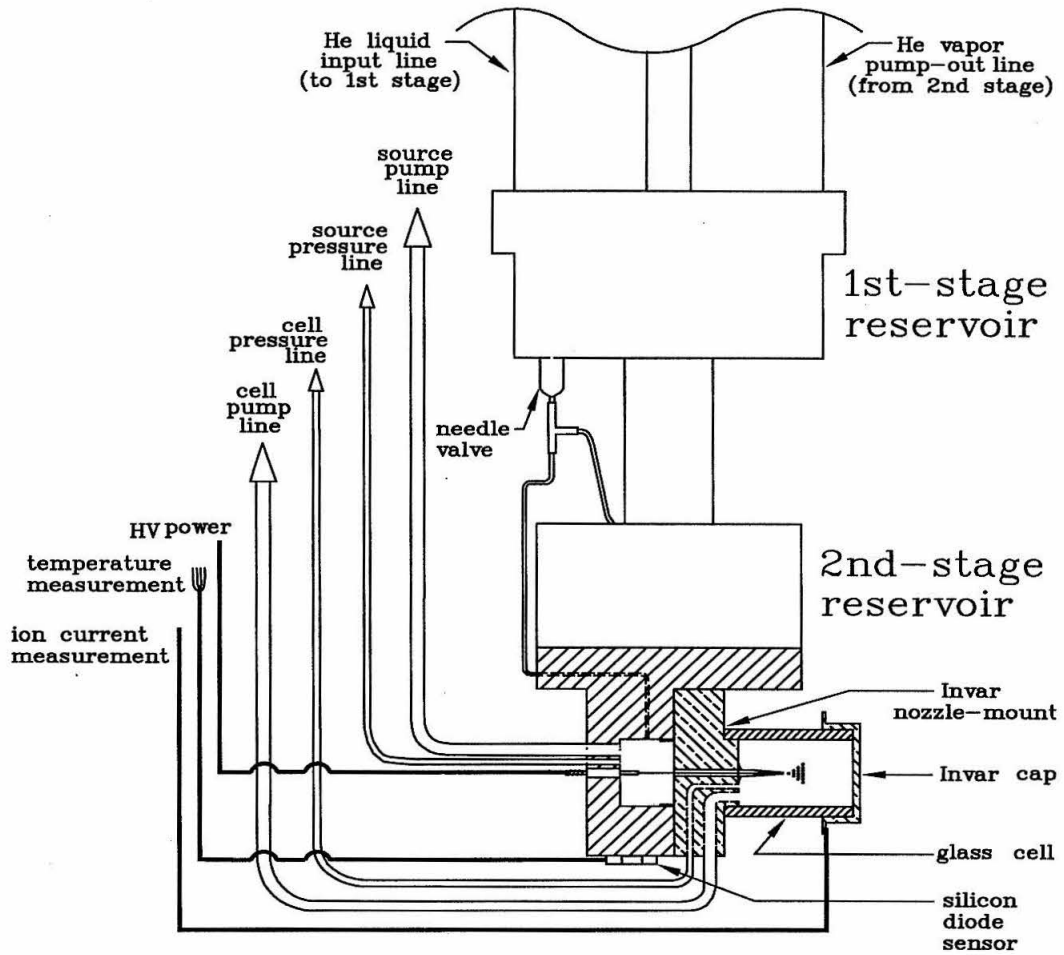


Figure 2-1

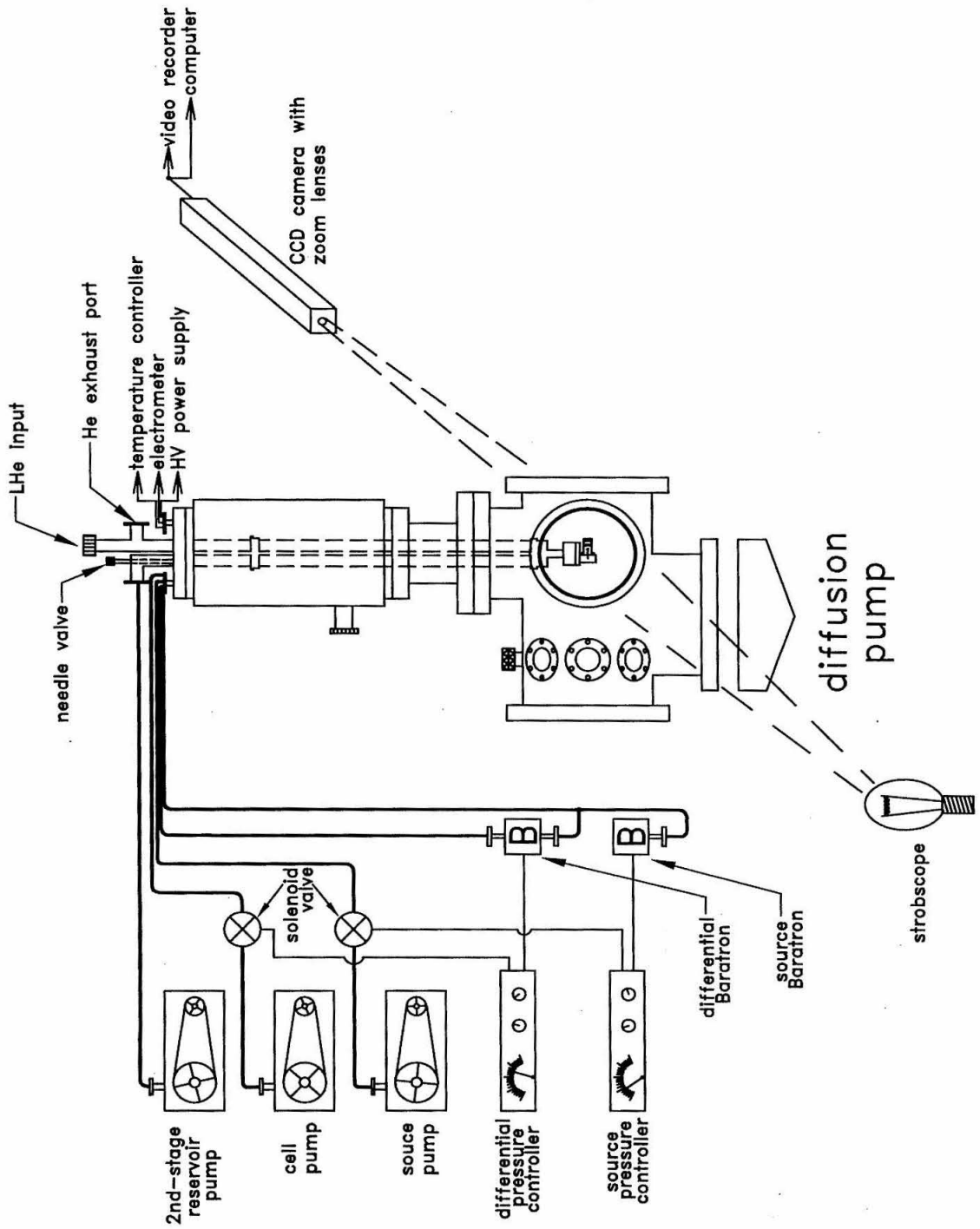


Figure 2-2

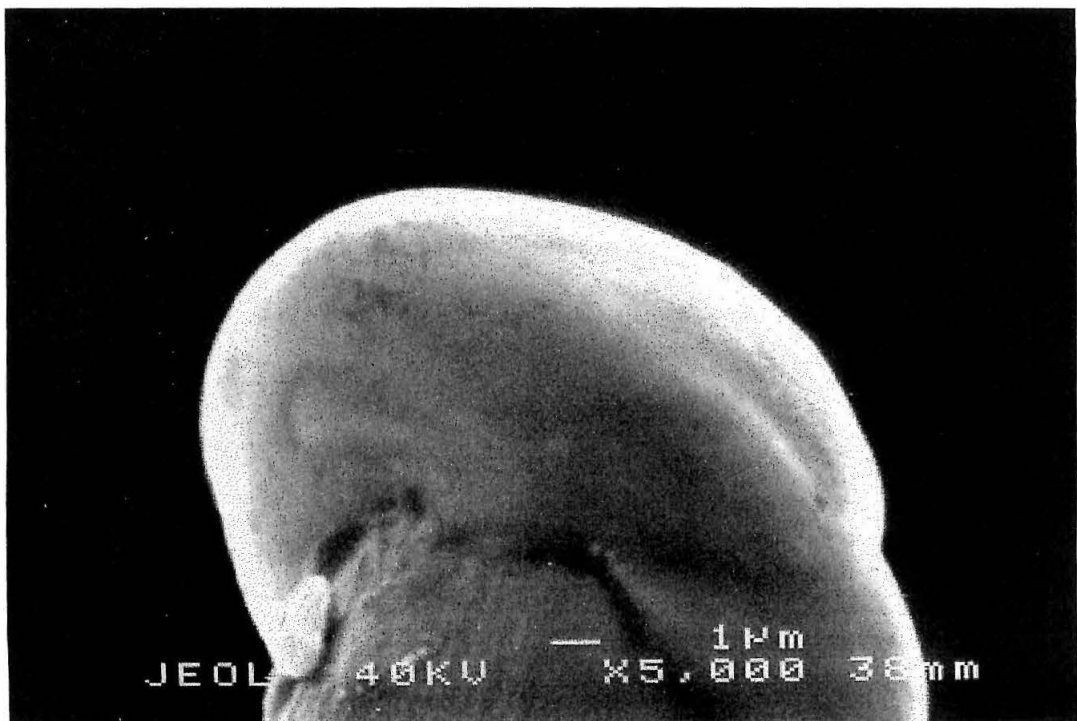
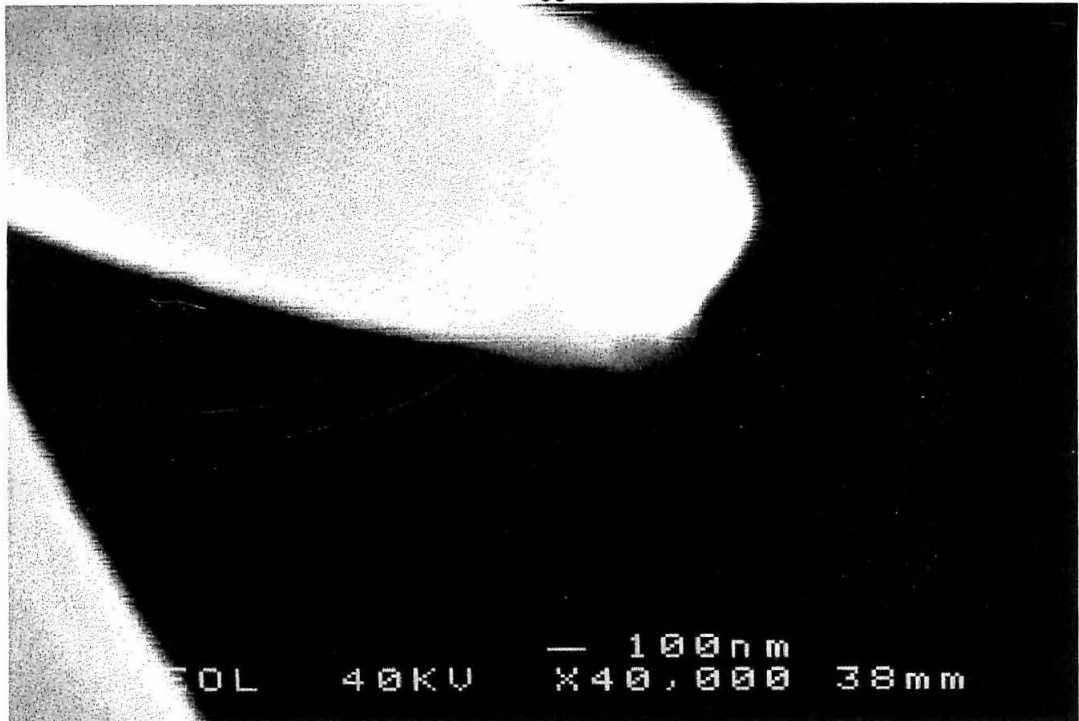


Figure 2-3

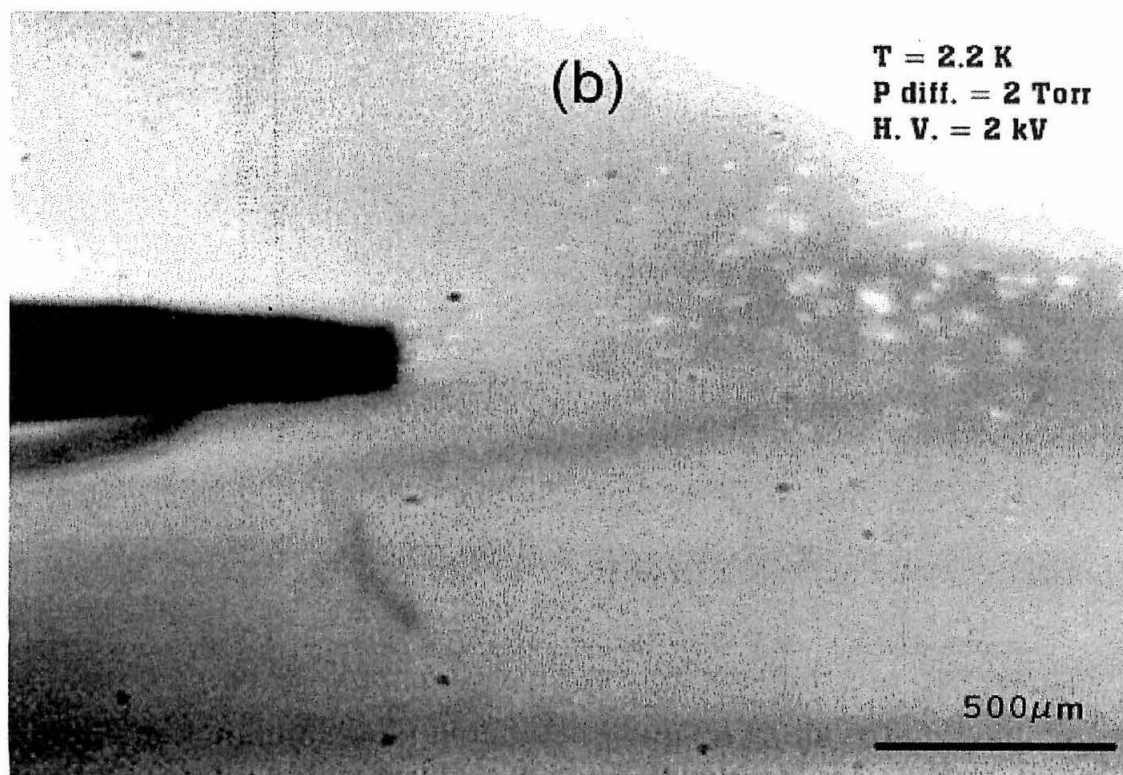
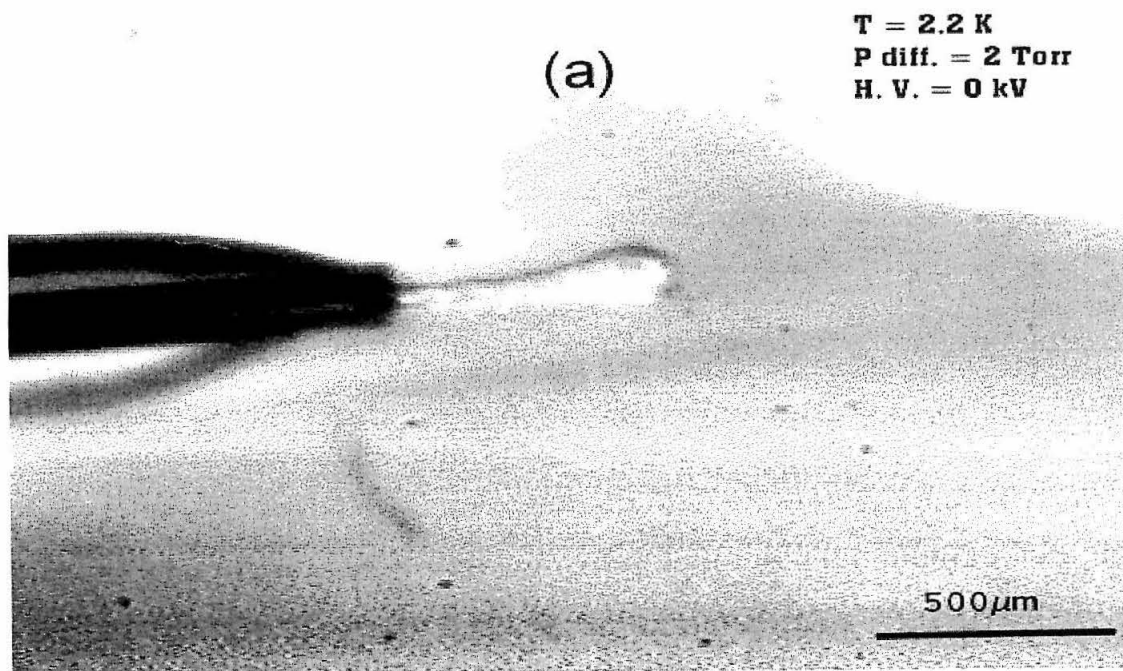


Figure 2-4

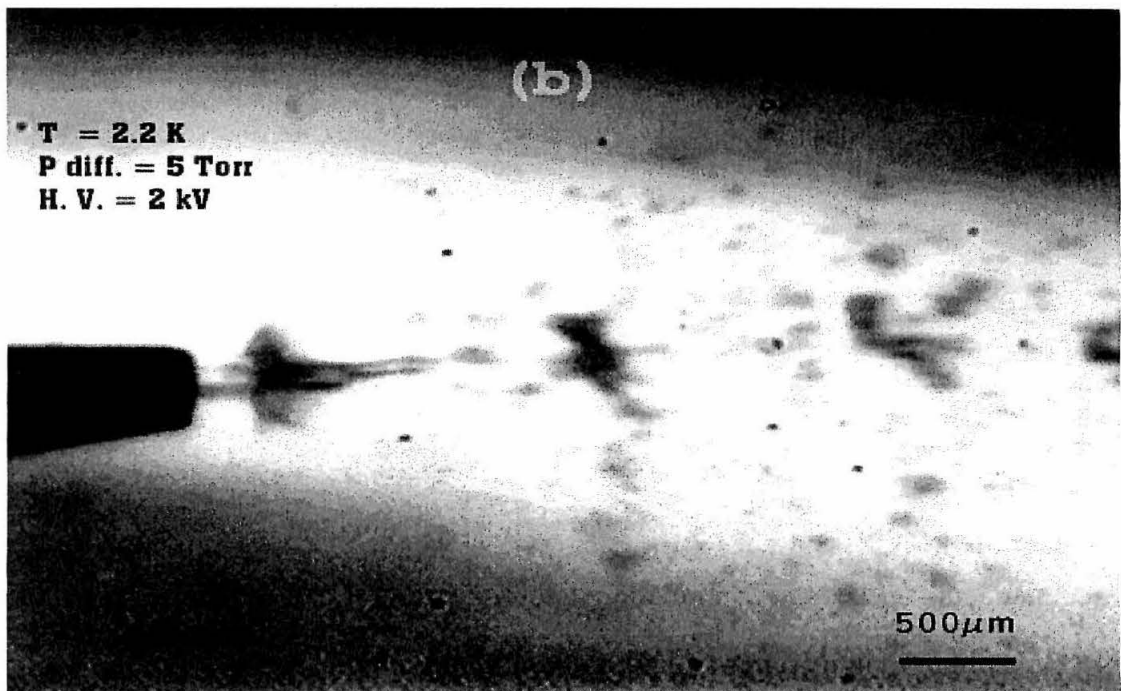
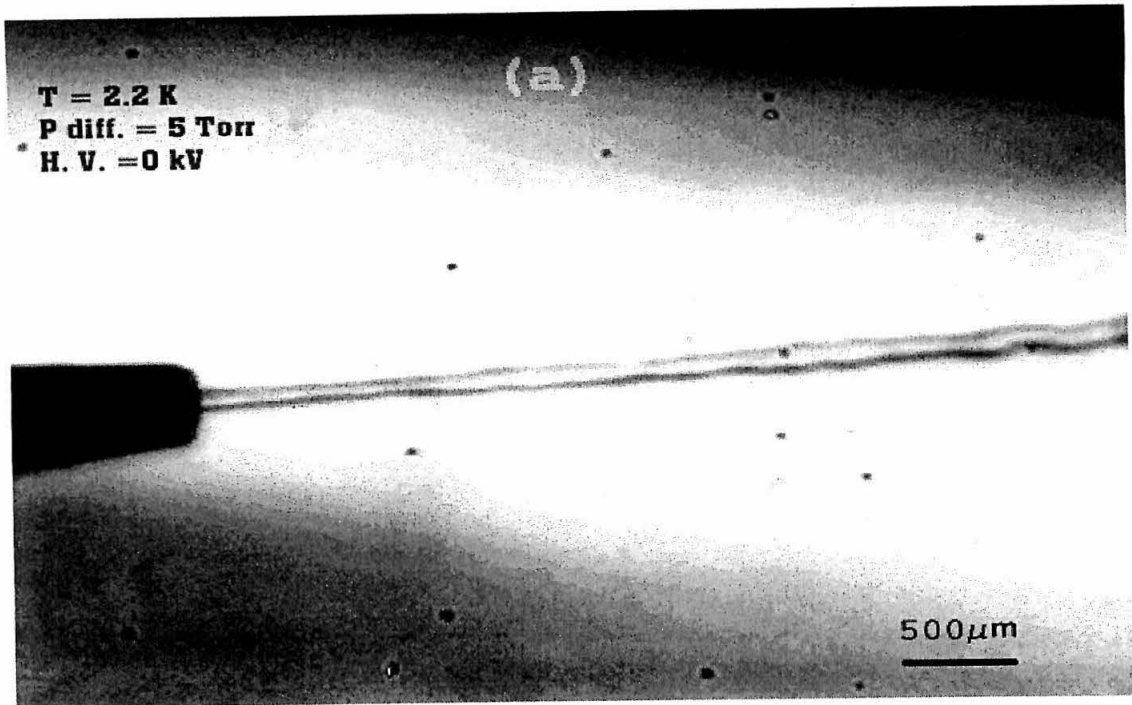


Figure 2-5

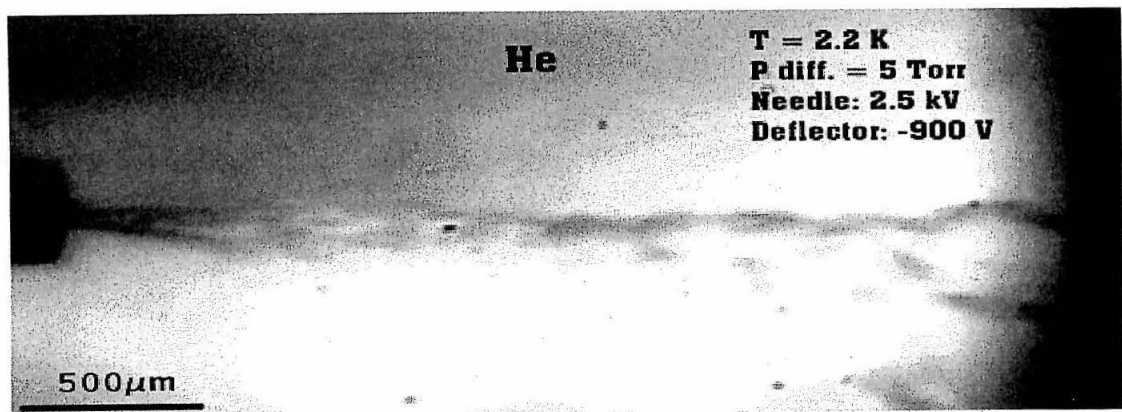
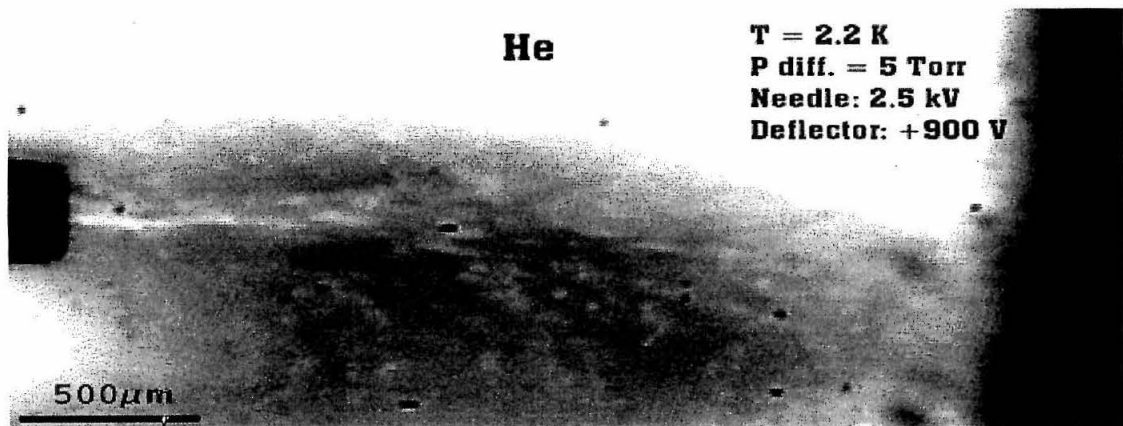
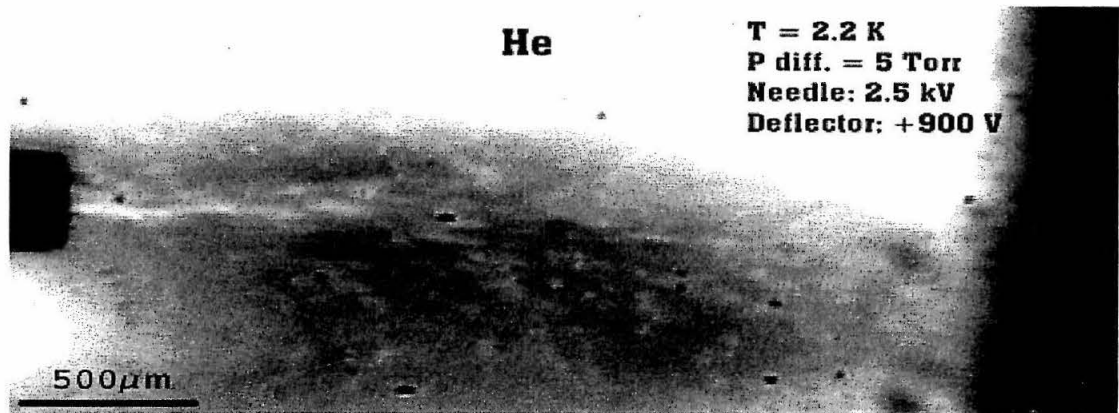


Figure 2-6

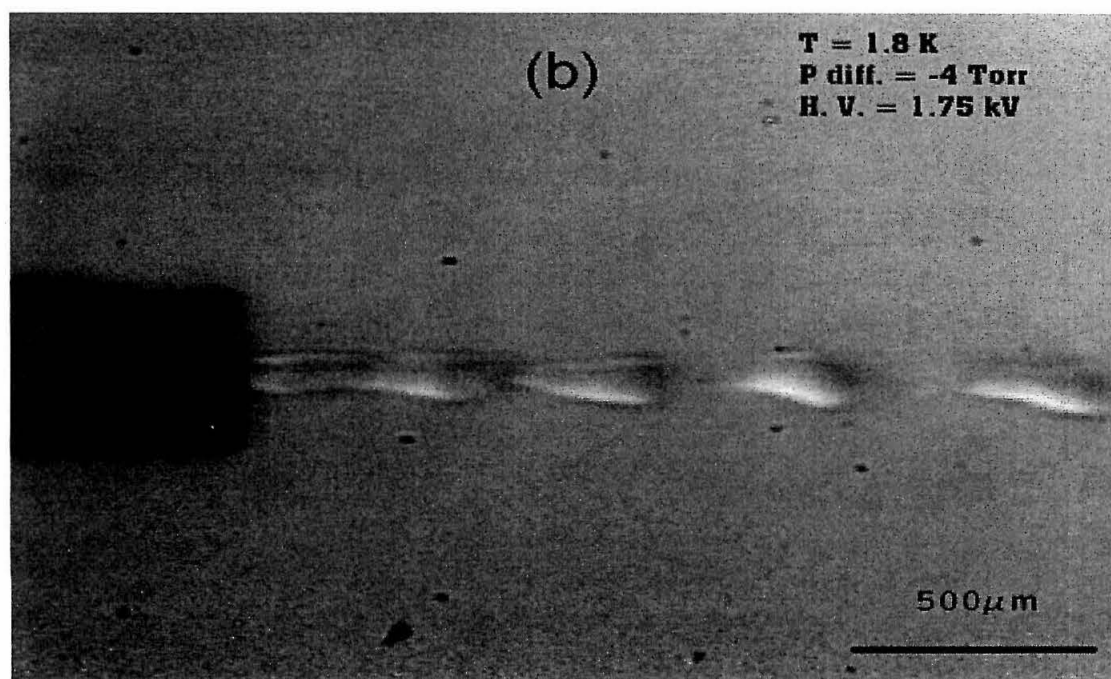
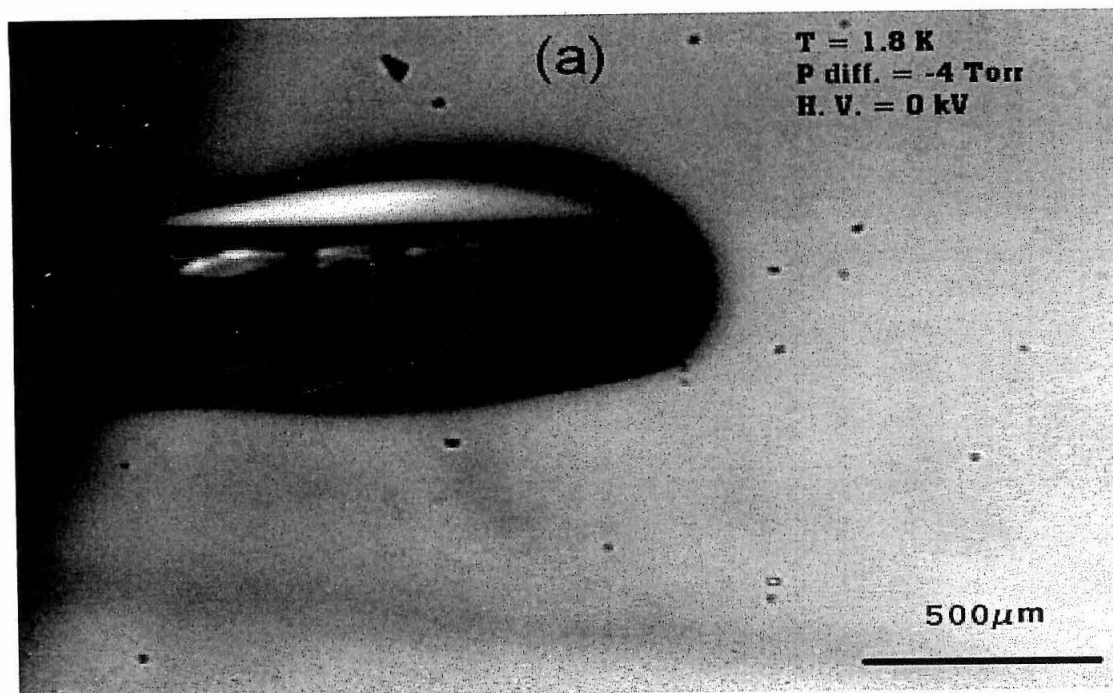


Figure 2-7

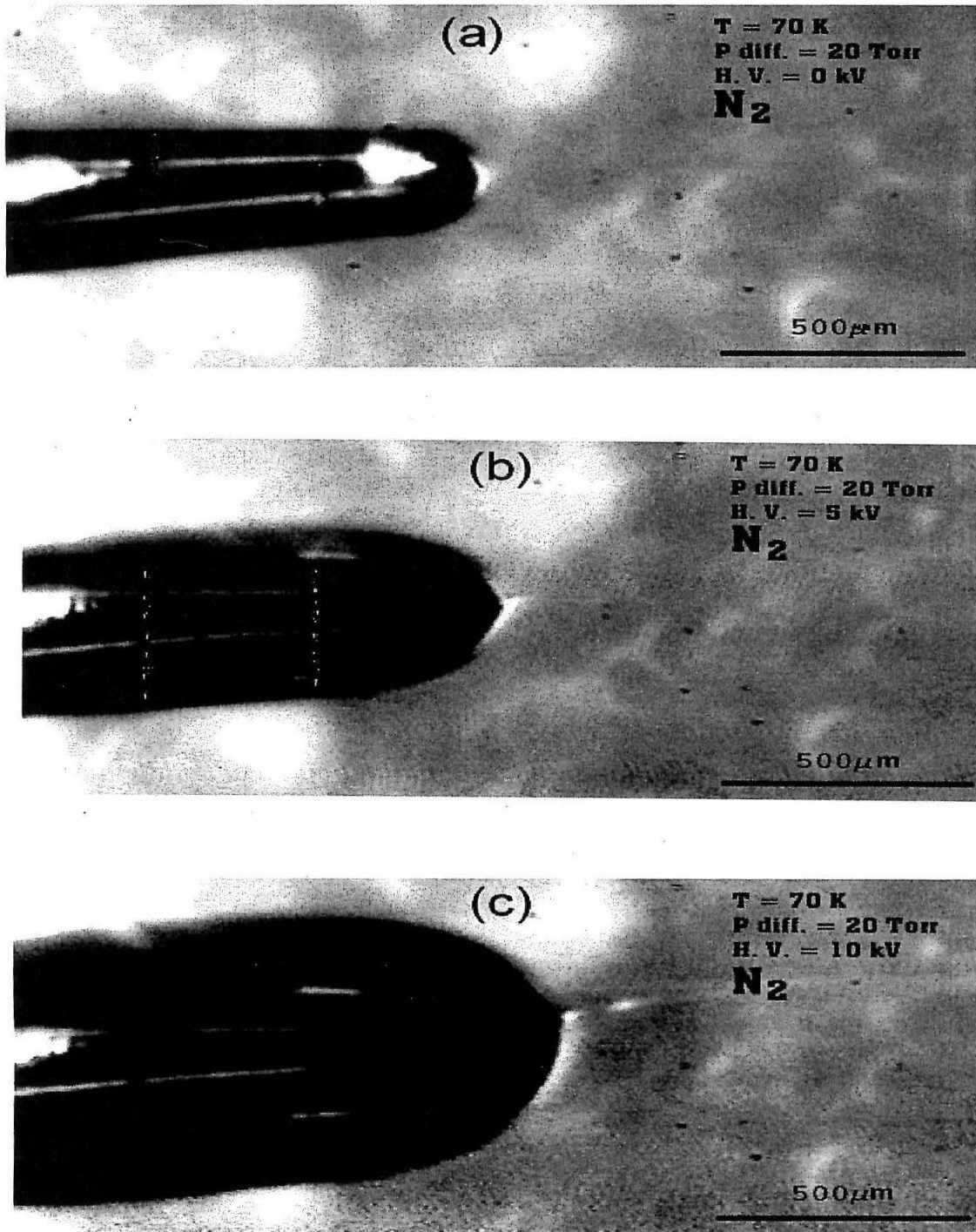


Figure 2-8

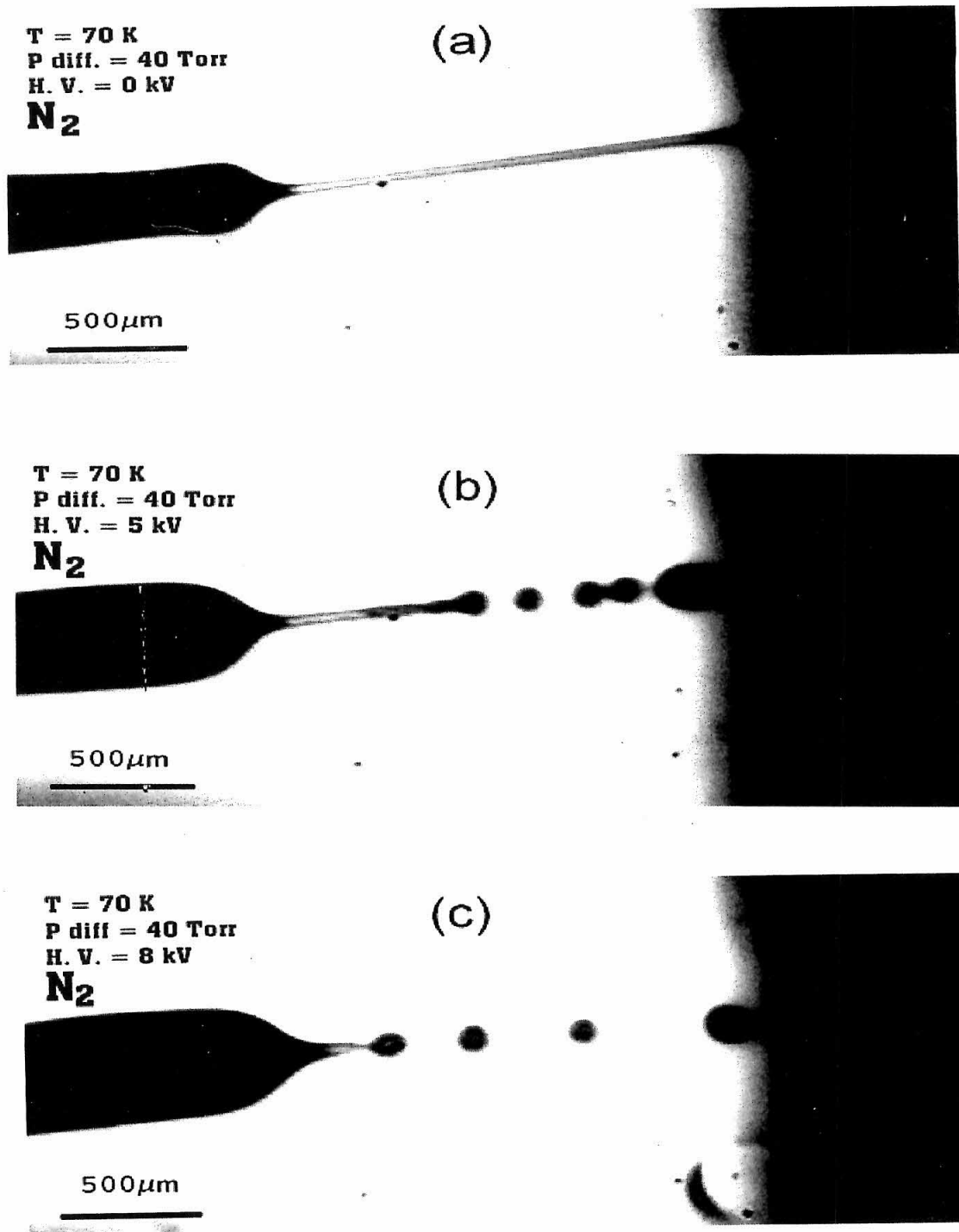


Figure 2-9

Chapter 3

Electronic Spectroscopy of the Alkaline-Earth

Halide Cluster Ca_2Cl_3

3. I. Introduction

Salt clusters are model systems for understanding ionic interactions. Their properties can often be calculated using simple electrostatic interactions to describe the attractive potentials. Alkali halide clusters have received much attention, because they are the simplest of the ionic salts.¹ Clusters as small as 40 atoms are predicted to have cubic structures characteristic of the bulk salt crystal. Smaller clusters however, can have several distinct isomers, including planar square lattice fragments and three-dimensional bridged structures. In contrast, alkaline-earth halide clusters are poorly studied. Bulk CaCl_2 salt has a rutilelike structure, in which the Cl atoms form a hexagonal closest packed structure and the Ca atoms fill octahedral holes in alternating rows.² The structures of small alkaline-earth halide clusters, as well as their transition to bulklike geometries with increasing size are not known.

The structures of alkaline-earth dihalides have been the subject of some controversy.³ Klemperer and colleagues demonstrated the existence of nonzero dipole moments in electric deflection experiments.^{4,5} There have since been numerous investigations concerning the factors governing the propensity for linear versus bent geometries.^{3,6,7,8} Polarization and d-hybridization appear to play important roles. The "dimer" species M_2X_4 have been computed to have many isomers, generally with two or more halogen atoms bridging the metal centers.⁶

Salt clusters with a closed shell ionic framework and outer shell electrons, such as Na_2F are termed excess-electron clusters. These radical clusters are suitable for spectroscopic investigation, because they possess bound-to-bound optical transitions. These transitions have been observed for the alkali halide clusters of composition $\text{Na}_n\text{F}_{n-1}$. Theoretical and experimental work on these small alkali halide

clusters^{9,10,11,12,13,14,15} show that, depending on the structure and size of the cluster, the excess electron can be localized in a lattice vacancy, around a sodium atom, or in delocalized surface or bulk states.

The analogous clusters of alkaline-earth halides have not been studied. However, diatomic alkaline-earth halides, which can be treated as an ionic $M^{2+}X^{-}$ core and an electron, have been investigated for decades.^{16,17,18,19} Field and coworkers have developed a zero-parameter one electron model based on ligand-field theory that describes the electronic states of these diatomics with semiquantitative accuracy. This picture also forms the basis for the pure precession model^{20,21,22,23} have developed for describing spin-rotation coupling in complexes of alkaline-earth metal atoms with polyatomic ligands. Alternatives include extension of Rittner's polarization model.^{24,25,26,27,28} Jungen and coworkers²⁹ have developed more accurate calculations of Rydberg states using multichannel quantum defect theory, which treats interaction of the electron with the ionic core by scattering methods.

The diatomic CaCl is typical of the alkaline-earth halides. Excited electronic states have been observed from $16\,093\text{ cm}^{-1}$ and higher.³⁰ The electronic states of CaCl arise from Ca^{+} free ion states in the field of the Cl^{-} ligand. The lowest lying transitions of the atomic ion Ca^{+} are $(3d_{3/2})^1 \leftarrow (4s_{1/2})^1$ at $13\,650.19\text{ cm}^{-1}$, and $(4p_{1/2})^1 \leftarrow (4s_{1/2})^1$ at $25\,191.51\text{ cm}^{-1}$. The presence of the chloride ion leads to extensive mixing and shifting of the free Ca^{+} atomic states. For example, the first excited state of CaCl, the $A\ ^2\Pi$ state at $16\,093\text{ cm}^{-1}$, is predominantly $4p$ in character rather than $3d$, but it contains mixtures of other Ca^{+} orbitals as well.

Ca_2Cl_3 is the smallest neutral polyatomic alkaline-earth halide that can be modeled as an unpaired electron bound to a framework of closed shell ions, Ca^{+2} and

Cl^- . In analogy with small alkali halide clusters, there may be several isomers, which could be linear, planar, and/or bridged. The unpaired electron may be localized on one Ca^+ , as in CaCl , or it may be shared between the two Ca^{+2} ions. The nature of the charge distribution should influence the energetics of the different isomers. Like CaCl , Ca_2Cl_3 should have transitions in the visible or ultraviolet (UV), which allow direct spectroscopic detection.

In this work we present an optical spectrum of the alkaline-earth halide cluster Ca_2Cl_3 detected by resonance enhanced multiphoton ionization (REMPI) spectroscopy. Quantum chemistry calculations using density functional theory (DFT) are used to locate minimum energy isomers and to determine their energies, vibrational frequencies, and excited states. By comparing the observed spectrum to the predicted properties we can unambiguously assign the spectrum.

3. II. Apparatus

The experimental apparatus will only be briefly described. Details will be published elsewhere.³¹ Ca_2Cl_3 was produced by laser ablation of calcium metal in a supersonic molecular expansion of a CCl_4/Ar mixture. The neutral molecules were formed in the ablation plasma, expanded into vacuum, and skimmed into a second region to form a molecular beam. Subsequently, the molecules were resonantly excited and then ionized by simultaneous pulses from two lasers in a 1+1' REMPI process. Ionization occurred in the extraction region of a time-of-flight (TOF) mass spectrometer. The ions were separated in time and collected on a microchannel plate detector. The spectra were obtained by scanning the excitation photon frequency while integrating the desired mass peak.

The CCl_4 (Aldrich, 99+%) was entrained in argon carrier gas by placing a bubbler filled with room temperature CCl_4 liquid on the gas line. The pressure in the gas line was 9.3 bar. The gas was pulsed into the source vacuum chamber by a piezoelectric driven valve at 19 Hz in 180 μs long pulses. After the valve seal, the gas traveled through a 13 mm channel. The calcium rod was placed immediately at the exit of the channel (see Figure 3–1). The calcium rods were machined from 99.8% pure ingots of calcium (Alfa Aesar). The rod was ablated by 25 mJ pulses of 1.064 μm light from a Nd:YAG (Continuum: Surelight I) laser focused to a 0.5 mm diameter spot. The rod was spun at 1 rpm and translated vertically.

The gas pulse expanded into a vacuum chamber held at an average pressure of 8×10^{-5} Torr (base pressure 2×10^{-7} Torr). The jet was then skimmed 7.5 cm from the nozzle to form a molecular beam in a second vacuum region kept at 1.5×10^{-6} Torr. The rotational temperature of diatomic CaCl produced under these conditions was typically 7–10 K. The molecular beam was crossed by the laser beams 20.3 cm from the tip of the skimmer.

The excitation step was performed by visible radiation from a Nd:YAG (Continuum NY61-20) pumped tunable dye laser (Continuum TDL51). DCM dye was used to generate photons in the 15 110 to 16 000 cm^{-1} range. The dye laser beam was slightly focused to a 5 mm diameter spot. The linewidth of the dye laser was 0.1 cm^{-1} . Observed band intensities varied over four orders of magnitude. A wide range of fluences were needed to prevent saturation. Pulse energies were varied from 1 μJ to 10 mJ with neutral density filters as needed. When recording unsaturated spectra, the power dependence of each band was first measured to determine the saturation limit. The bands were then scanned in the linear regime.

An excimer laser (Lamda Physik EMG101) was used for the ionization step. The 308 nm, 20 ns pulses were focused into a 2×4 mm rectangular spot, overlapping with the dye laser beam. The ionization took place in the extraction region of a Wiley-McLaren TOF mass spectrometer. The ions were accelerated to an energy of 3 keV, mass separated in a 1.0 m TOF tube, and detected by dual chevron microchannel plates (Galileo Electro-Optics/Burle FTD-2003). The signal was amplified by a Comlinear CLC401 amplifier. Mass spectra were recorded with a LeCroy 8818A transient digitizer. To collect an optical spectrum, ion signal of the selected mass peak was integrated (SRS 250 Gated Integrator), digitized (Keithley Metrabyte DAS1602 Acquisition board), and recorded as a function of dye laser frequency.

3. III. Experimental results

3. III. a. TOF mass spectrum

Figure 3–2 displays a typical TOF mass spectrum. The most prominent features in the spectrum are Ca^+ and CaCl^+ ion peaks. CaO^+ and CaOH^+ also appear in the spectrum as minor features. Four peaks are observed for Ca_2Cl_3^+ , as can be seen in the inset in Figure 3–2. Ca_2Cl_3^+ peaks are observed only when the excitation photon is in resonance with a Ca_2Cl_3 transition, while Ca^+ and CaCl^+ peaks are observed even without resonant excitation. The spectrum shown in Figure 3–2 is obtained when the excitation laser is tuned to the Ca_2Cl_3 0-0 transition at $15\,350.8\text{ cm}^{-1}$. The intensity of Ca_2Cl_3^+ is approximately 0.07 relative to the CaCl^+ intensity at this frequency.

The four mass peaks of Ca_2Cl_3^+ are assigned to the four possible combinations of the chlorine isotopes: $\text{Ca}_2\text{}^{35}\text{Cl}_3$ (185 amu), $\text{Ca}_2\text{}^{35}\text{Cl}_2\text{}^{37}\text{Cl}$ (187 amu), $\text{Ca}_2\text{}^{35}\text{Cl}\text{}^{37}\text{Cl}_2$ (189

amu) and $\text{Ca}_2\ ^{37}\text{Cl}_3$ (191 amu). The observed intensity ratio of the peaks, 1:0.84:0.31:0.039, agrees well with that predicted by the natural isotope abundance, 1:0.96:0.31:0.033.

3. III. b. REMPI spectra of Ca_2Cl_3

Visible 1+1' REMPI spectra were obtained for each of the four isotopomers of Ca_2Cl_3 in the range from 15 110 to 16 000 cm^{-1} . Unsaturated scans of $\text{Ca}_2\ ^{35}\text{Cl}_3$ and $\text{Ca}_2\ ^{35}\text{Cl}_2\ ^{37}\text{Cl}$ were acquired with 0.12 cm^{-1} step size. The signals of $\text{Ca}_2\ ^{35}\text{Cl}\ ^{37}\text{Cl}_2$ and $\text{Ca}_2\ ^{37}\text{Cl}_3$ were near the detection noise limit when unsaturated. We therefore scanned these spectra under saturating conditions (35 mJ/cm^2) and a typical step size of 0.6 cm^{-1} to locate the band frequencies.

The overall spectra of the four isotopomers are similar, but differ in detail. A REMPI spectrum of $\text{Ca}_2\ ^{35}\text{Cl}_3$ is shown in Figure 3–3(a). Three of the bands are shown in detail in Figure 3–4(a), 3–4(b), and 3–4(c). All spectra are dominated by a single intense band at 15 350.8 cm^{-1} and a series of significantly weaker vibronic bands up to 640 cm^{-1} to the blue. The bands of the higher-mass isotopomers are slightly redshifted (0.0 to 6.8 cm^{-1}), with the magnitude of the red shift increasing with increasing frequency and mass. For $\text{Ca}_2\ ^{35}\text{Cl}_2\ ^{37}\text{Cl}$ and $\text{Ca}_2\ ^{35}\text{Cl}\ ^{37}\text{Cl}_2$, several of the observed bands are also split.

There are no extended progressions; however, the spectrum repeats itself. The second strongest band at 15 616.7 cm^{-1} , is the origin for a set of approximately nine bands with a spectral pattern that is nearly identical (in spacings) to the main bands observed in the first 270 cm^{-1} . The relative intensities are roughly similar as well. The last band in the sequence, at 15 881 cm^{-1} , may be an overtone of the mode giving rise to the 15 616.7 cm^{-1} band.

All bands in the spectra have partially resolved structure, which is dominated by two components split by approximately $0.8 \pm 0.2 \text{ cm}^{-1}$. The splitting is consistent throughout the spectrum. It is similar for both $\text{Ca}_2^{35}\text{Cl}_3$ and $\text{Ca}_2^{35}\text{Cl}_2^{37}\text{Cl}$, and appears to be the same for the $\text{Ca}_2^{35}\text{Cl}^{37}\text{Cl}_2$ and $\text{Ca}_2^{37}\text{Cl}_3$ bands, as well. Figure 3–4(a) shows the splitting in the 0-0 band at $15\,350.8 \text{ cm}^{-1}$ for both $\text{Ca}_2^{35}\text{Cl}_3$ (solid line) and $\text{Ca}_2^{35}\text{Cl}_2^{37}\text{Cl}$ (dotted line). The overall width is comparable to that expected from the rotational contour of a molecule of this size at 7 K - 10 K.

3. III. b. 1. Spectrum of $\text{Ca}_2^{35}\text{Cl}_3$

In the spectrum of $\text{Ca}_2^{35}\text{Cl}_3$, we observe 46 weak vibronic bands located from 29 to 632 cm^{-1} to the blue of the origin. The band intensities vary by more than four orders of magnitude. The 21 most intense bands were scanned under unsaturated conditions, but the weaker bands had to be collected at higher laser powers due to lower signal to noise ratio.

Table 3–I lists the frequencies and intensities of the bands, as well as frequencies relative to the first band. The intensities of the weaker bands are listed as weak or very weak; these bands are likely to be saturated.

Figure 3–3(a) shows the 21 unsaturated bands, with the weaker vibronic bands scaled up by 36 times relative to the strongest band. The dominant band at $15\,350.8 \text{ cm}^{-1}$, which is furthest to the red, is henceforth assigned as the origin (0-0) band. The second strongest band, at $15\,616.7 \text{ cm}^{-1}$, is 40 times smaller than the origin, and the third strongest band, at $15\,478.1 \text{ cm}^{-1}$, is 300 times smaller. Many of the weaker bands are barely discernible on a linear scale. All bands are therefore shown in Figure 3–3(b)

on a semilogarithmic stick spectrum. The weaker bands detected under saturated conditions are shown as dotted lines.

3. III. b. 2. Spectrum of $\text{Ca}_2^{35}\text{Cl}_2^{37}\text{Cl}$

The band frequencies recorded for $\text{Ca}_2^{35}\text{Cl}_2^{37}\text{Cl}$ are listed in Table 3-II, together with intensities and vibrational frequencies. The spectrum is nearly identical to that taken for $\text{Ca}_2^{35}\text{Cl}_3$. All the same bands are present in the $\text{Ca}_2^{35}\text{Cl}_2^{37}\text{Cl}$ spectrum. However, the bands exhibit small red shifts as large as 4.4 cm^{-1} relative to the frequencies of the $\text{Ca}_2^{35}\text{Cl}_3$ bands, and some of the bands are split into two components. The shifts, $\Delta\nu^{187}$, and the splittings are also listed in Table 3-II.

Figure 3-5 shows a portion of the spectra of $\text{Ca}_2^{35}\text{Cl}_3$ (solid line) and $\text{Ca}_2^{35}\text{Cl}_2^{37}\text{Cl}$ (dotted line) from $15\,570$ to $15\,640\text{ cm}^{-1}$. These spectra were collected in a single scan, and thus some of the bands are saturated. The shifts and splittings seen here are representative of those observed throughout the spectrum of $\text{Ca}_2^{35}\text{Cl}_2^{37}\text{Cl}$. The isotope shifts in the region shown in this figure range from 0.0 to 2.1 cm^{-1} . The intensities of the $\text{Ca}_2^{35}\text{Cl}_2^{37}\text{Cl}$ bands are comparable to those of the $\text{Ca}_2^{35}\text{Cl}_3$ isotopomer bands, with the exception of the $\text{Ca}_2^{35}\text{Cl}_2^{37}\text{Cl}$ band at $15\,623.4\text{ cm}^{-1}$, which is nine times stronger.

The magnitudes of the redshifts and splittings increase with increasing frequency. This trend can be seen in Figure 3-4, where the spectra of $\text{Ca}_2^{35}\text{Cl}_3$ (solid line) and $\text{Ca}_2^{35}\text{Cl}_2^{37}\text{Cl}$ (dotted line) are overlaid for three bands. The splitting of the origin band is less than 0.1 cm^{-1} at the origin, 2.0 cm^{-1} for the second strongest band at $15\,616.7\text{ cm}^{-1}$, and 4.4 cm^{-1} for the band furthest to the blue at $15\,881.0\text{ cm}^{-1}$.

Ten of the bands observed in the $\text{Ca}_2^{35}\text{Cl}_3$ spectrum are split into two components in the $\text{Ca}_2^{35}\text{Cl}_2^{37}\text{Cl}$ spectrum. Typically, one of the split components of Ca_2

$^{35}\text{Cl}_2\ ^{37}\text{Cl}$ is shifted a few wavenumbers to the red, and the other component exhibits little or no shift relative to the $\text{Ca}_2\ ^{35}\text{Cl}_3$ band. In Figure 3–5, three of the six bands of $\text{Ca}_2\ ^{35}\text{Cl}_3$ are split into two bands in the $\text{Ca}_2\ ^{35}\text{Cl}_2\ ^{37}\text{Cl}$ spectrum. The band observed at $15\ 577.3\ \text{cm}^{-1}$ in the $\text{Ca}_2\ ^{35}\text{Cl}_3$ spectrum splits into the bands at $15\ 575.5$ and $15\ 577.0\ \text{cm}^{-1}$ in the $\text{Ca}_2\ ^{35}\text{Cl}_2\ ^{37}\text{Cl}$ spectrum. Similarly, the band at $15\ 628.9\ \text{cm}^{-1}$ splits into the $15\ 626.8$ and $15\ 628.3\ \text{cm}^{-1}$ bands. For the stronger band in the spectrum at $15\ 616.7\ \text{cm}^{-1}$, the split is not completely discernable and the nonshifted component appears as a shoulder to the shifted component. Figure 3–4(b) shows the $15\ 616.7\ \text{cm}^{-1}$ band in closer detail. The intensity of the shifted component is approximately twice as intense as the nonshifted. The addition of the intensity of both components is comparable to that of the $\text{Ca}_2\ ^{35}\text{Cl}_3$ band.

3. III. b. 3. Spectra of $\text{Ca}_2\ ^{35}\text{Cl}\ ^{37}\text{Cl}_2$ and $\text{Ca}_2\ ^{37}\text{Cl}_3$

The spectra recorded for $\text{Ca}_2\ ^{35}\text{Cl}\ ^{37}\text{Cl}_2$ and $\text{Ca}_2\ ^{37}\text{Cl}_3$ display the same trends as the spectra of the lighter isotopomers. Due to lower signal to noise, these spectra were taken under saturated conditions. All of the intense bands were observed, but weaker bands were undetected. The red shifts are larger for the heavier the isotopomers. Table 3–III and Table 3–IV list the observed bands for $\text{Ca}_2\ ^{35}\text{Cl}\ ^{37}\text{Cl}_2$ and $\text{Ca}_2\ ^{37}\text{Cl}_3$, along with the vibrational frequencies relative to the origin and the frequency shifts relative to the $\text{Ca}_2\ ^{35}\text{Cl}_3$ bands.

The spectrum of $\text{Ca}_2\ ^{35}\text{Cl}\ ^{37}\text{Cl}_2$ has splittings similar to those of the di-substituted isotopomer, $\text{Ca}_2\ ^{35}\text{Cl}_2\ ^{37}\text{Cl}$. Three of the stronger peaks at $15\ 574$, $15\ 613$ and $15\ 739\ \text{cm}^{-1}$ have discernible splittings. No splitting of bands is observed in the spectrum of $\text{Ca}_2\ ^{37}\text{Cl}_3$.

3. IV. Quantum chemistry calculations

3. IV. a. Density functional theory (DFT) calculations

Ab initio calculations using the Gaussian98³² software package were performed to aid in assigning the spectra. Geometries were optimized and vibrational frequencies calculated using the B3LYP density functional theory (DFT) method and the 6-311+G(3df) basis set. Optimized ground state energies were computed at the MP2(FC)/6-311+G(2df) level. Excited electronic state properties were calculated using the configuration interaction-singles (CIS) method and, where possible, symmetry constrained B3LYP method.

Three stable isomers of Ca_2Cl_3 were found: a C_{2v} planar V-shaped structure (V), a C_{2v} planar ring, and a D_{3h} trigonal bipyramid. The calculated geometries are shown in Figure 3–6. The ring is the lowest energy structure of the three. The bipyramid structure is 31.7 kJ/mol higher in energy than the ring, and the V structure is 76.7 kJ/mol higher in energy than the ring structure. Vibrational frequencies and excited electronic state calculations were performed for the three structures. Tables 3–V and 3–VI list the coordinates, energies, vibrational frequencies, and the excited electronic states for these geometries.

3. IV. a. 1. Planar C_{2v} V structure

We initially attempted to find a linear isomer, but both $D_{\infty h}$ and $C_{\infty v}$ forms were transition states. Upon lifting all symmetry constraints, the geometry relaxed to the C_{2v} V structure (Figure 3–6(a)). In this planar isomer the Ca atoms in two Ca-Cl moieties are bound to a central, but off-axis chlorine atom, Cl(1), and appear to be slightly bound to each other as well. The Ca-Cl bond lengths are $r_1=2.459 \text{ \AA}$ in the CaCl(2) subgroups

and a somewhat longer $r_2 = 2.661 \text{ \AA}$ between the Ca atoms and Cl(1). For comparison, the Ca-Cl distance is 2.437 \AA in CaCl,²⁷ 2.20 \AA in CaCl⁺,¹⁶ and 2.74 \AA in the hydrophilite salt structure of CaCl₂(s).³³ The Ca-Ca bond distance is 3.716 \AA , which is closer than the 4.277 \AA distance in the ground state of the Ca₂ dimer.³⁴ The identical calcium atoms share equally the unpaired electron. This suggests the formation of a partial σ bond between the Ca atoms.

In this geometry, there are two distinct chlorine sites, the central atom Cl(1) and the outer atoms Cl(2). The Ca₂³⁵Cl₂³⁷Cl and Ca₂³⁵Cl³⁷Cl₂ isotopomers each have two possible isomers, with C_{2v} and C_s symmetries, depending on which chlorine atoms are substituted.

The nine fundamental vibrational modes for the V structure range from 3.8 to 387.4 cm^{-1} . Five excited electronic states, 2B_1 , 2B_2 , 2A_1 , 2A_1 , and 2A_2 were calculated, with the corresponding vertical transitions ranging from 2.18 to 4.55 eV at the CIS level of theory.

3. IV. a. 2. Trigonal bipyramid D_{3h} structure

In the bipyramid structure, the calcium atoms lie above and below the plane of the three chlorine atoms. Each calcium atom bonds to all three chlorine atoms. The Ca-Cl distance (r_1) is 2.663 \AA , while the Cl-Cl distance (r_2) is 3.593 \AA . The distance between the calcium atoms is 3.361 \AA , which is closer than in the V structure. The unpaired electron is equally shared between both calcium atoms.

We calculated six vibrational modes, three of which are degenerate, for the ground state of the bipyramid structure with frequencies ranging from 112.7 to 293.5 cm^{-1} . Six excited electronic states were calculated, of which two are degenerate. The

$^2A_2''$ state, at 0.04 eV above the ground state, is significantly lower than the other states. Transitions to the higher states (Table 3–VI) range from 1.77 to 2.50 eV at the CIS level of theory. Because this isomer has D_{3h} symmetry, Jahn-Teller distortion will occur for the degenerate excited electronic states. In addition, pseudo-Jahn-Teller effects may occur, because all states occur in nearly degenerate pairs of prime and double-prime symmetry, which will be mixed by breaking the symmetry to form a C_{3v} structure.

3. IV. a. 3. Planar C_{2v} ring structure

The ring structure (Figure 3–6(c)) has a four-member ring with Cl(2) and Cl(3) bridging the two Ca(1) and Ca(2) atoms. The third chlorine atom, which we denote as the terminal or tail Cl(1), extends from Ca(1) as a tail from the ring. Ca(1) is thus bound to three Cl atoms. The Ca–Cl distances are 2.651 Å (r_2) and 2.666 Å (r_3) in the ring structure and 2.463 Å (r_1) for the tail Ca(1) – Cl(1) bond. The Ca – Ca distance is 3.883 Å. The dissociation energy to CaCl₂ and CaCl products is 1.727 eV at the B3LYP level.

Unlike the V and the bipyramid isomers, the unpaired electron is localized on just one calcium atom, Ca(2). The Mulliken spin density on this atom at the B3LYP level is 99.7%. Thus, the structure appears to be a classical ionically bound cluster composed of Ca⁺¹, Ca⁺², and three Cl⁻ ions. The chromophore is the Ca⁺¹ radical ion.

Fundamental vibrational frequencies range from 29 to 381 cm⁻¹ for the ground state C_{2v} ring. Two of the three lowest frequency modes are B_1 out-of-plane bends. Three modes are B_2 out-of-plane bends, and the remaining modes are A_1 symmetry. The highest frequency mode, ν_9 , is the Ca-Cl tail stretch.

There are two distinct chlorine sites, the terminal Cl(1) and the two ring Cl(2) sites. This leads to two isotopomers for both the mono- (Ca₂³⁵Cl₂³⁷Cl) and di-substituted

(Ca₂³⁵Cl³⁷Cl₂) forms. If both ring chlorine atoms are the same isotope, the structure has C_{2v} symmetry; if they are different, the symmetry is C_s. In both the mono- and di-substituted isotopomers, some of the observed vibronic bands are slightly shifted relative to those of the Ca₂³⁵Cl₃ isotopomer. For some modes, both isomers have the same redshift. For specific modes where either the tail or the ring chlorines dominate the vibration, the C_{2v} and C_s isomers have different redshifts. For example, the ν₉ mode is predominantly the stretch of the terminal Ca – Cl bond. In the C_{2v} isomer of Ca₂³⁵Cl₂³⁷Cl, the ³⁷Cl is substituted at the tail, and the frequency is shifted; in the C_s structure, the frequency has almost no shift since the tail Cl is a ³⁵Cl atom.

Four excited electronic states — ²B₁, ²B₂, ²A₁ and ²A₂ — were calculated at the CIS level for the ring structure and found to have adiabatic transition energies ranging from 1.75 to 3.06 eV. (Table 3–V). Oscillator strengths are 0.2174, 0.1739, 0.1400, and 0.000, respectively. Excitation to the ²A₂ state is dipole forbidden.

3. IV. b. Excited electronic states of the planar C_{2v} ring isomer

Close agreement between the experimental data and the calculated properties of the C_{2v} ring structure warranted further calculations for this structure. The coordinates, excitation energies and vibrational frequencies were calculated for three of the excited electronic states ²B₁, ²B₂, and ²A₁. (Table 3–V).

Two methods were used to calculate the excited electronic state energies of the C_{2v} ring structure. Table 3–V shows the B3LYP and CIS excited state energies. CIS results are listed for three augmented basis sets, 6-311+G(d), 6-311+G(2d) and 6-311+G(3df). The results do not converge, but the differences between states diminish

with increasing basis sets. The B3LYP energies are significantly lower than the CIS energies.

Geometries and frequencies for the 2B_1 , 2B_2 , and 2A_2 states were calculated with the B3LYP method and the 6-311+G(3df) basis set. CIS calculations were used for the 2A_1 state. Overall, the geometries of the four excited electronic states and the ground state are very similar. Angles and bond lengths vary by less than 3%. Variations in the vibrational frequencies among the states are highest in the ν_1 , ν_3 and ν_5 calculated modes but less than 10% in the other six modes.

3. V. Assignment of spectra

3. V. a. *Isomeric assignment*

The observed pattern of a strong origin and much weaker vibronic bands indicates that there is little change in the geometry and vibrational frequencies between the ground and excited electronic states. There are no extended vibronic progressions in the spectrum, making the assignment less straightforward. We therefore compare the observed spectrum with predictions for the three different minimum energy structures computed by the DFT method.

3. V. a. 1. Planar C_{2v} V structure

The V structure is calculated to be about 34.1 kJ/ mol higher than the lowest energy isomer, the ring structure, at the MP2/6-311+G(2d) level. If this isomer is present, it is metastable. At the DFT level, the vertical excitation energies of the two lowest excited electronic states, the 2B_1 and 2B_2 states, are near the observed transition,

although at the CIS level the transition to the 2B_2 state is 0.9 eV higher. All other states are much higher in energy and therefore unlikely candidates. However, adiabatic energies for the transitions to the 2B_1 and 2B_2 are significantly lower than the vertical energies, indicating large geometry changes upon excitation. The electronic spectrum should therefore have a broad Franck-Condon envelope, contrary to observations. The predicted frequencies of the ground state fundamental modes ν_2 , ν_4 , ν_5 , ν_7 , and ν_9 are in good agreement with some of the observed bands ($\sigma = 4\%$). However, the three strongest observed vibronic bands, at 127.4, 226.5, and 266.0 cm^{-1} , cannot be assigned. The observations are therefore not consistent with assignment to the C_{2v} V structure.

3. V. a. 2. Trigonal bipyramid D_{3h} structure

The bipyramid structure is predicted to be metastable, with energy 76.7 kJ/ mol above the lowest energy isomer at the MP2(FC)/6-311+G(2d,p) level. Five excited electronic states were calculated for the D_{3h} structure. While transitions to two ${}^2A_2''$ states and a ${}^2E'$ state are dipole allowed in D_{3h} symmetry, Jahn-Teller and pseudo-Jahn-Teller distortions will lower the symmetry and render all five transitions allowed. Transitions to the 2E and ${}^2E'$ are predicted to be near the observed transition. However, the lowest predicted vibrational frequency for the ground state is 112.7 cm^{-1} ; in contrast, the five lowest vibrational bands are observed below 110 cm^{-1} . While nonadiabatic interactions can lead to additional low frequency modes and splittings, the resulting geometric distortions should also lead to substantial intensity in higher vibronic bands. The spectrum does not exhibit the complexity one would expect for this structure.

3. V. a. 3. Planar C_{2v} ring structure

The ring structure is the minimum energy isomer calculated. The four lowest electronically excited states, 2B_1 , 2B_2 , 2A_1 , and 2A_2 , all lie within 0.5 eV of the observed transition at both B3LYP and CIS/6-311+G(3df) levels of theory. All of the excited electronic states are predicted to have nearly the same geometry and vibrational frequencies as the ground state. Thus, of the three geometries, only the C_{2v} ring is qualitatively consistent with the observed intensity pattern.

This conclusion is quantitatively borne out in Franck-Condon simulations for three of the transitions, ${}^2B_1 \leftarrow X {}^2A_1$, ${}^2B_2 \leftarrow X {}^2A_1$, and ${}^2A_2 \leftarrow X {}^2A_2$. Simulations were performed using the B3LYP optimized geometries and frequencies. For each of the transitions, the origin band was predicted to be the dominant feature, and the next three strongest bands were the A_1 bands ν_4 , ν_7 , and ν_9 at 123.8, 230.6, and 381.1 cm^{-1} , respectively. The intensity ratios relative to the origin band were calculated to be 1:0.196:0.017:0.001, 1:0.004:0.002:0.004, and 1:0.023:0.105:0.071, for the transitions to the 2B_1 , 2B_2 , and 2A_2 states, respectively. The experimental ratio of the strongest of the allowed bands, the ν_4 mode, to the origin band is 1:0.003. Thus, the Franck-Condon factors for the ring structure are consistent with the observed spectrum, with the transition to the 2B_2 state giving very good agreement.

There are many more bands in the observed spectrum than are predicted by the Franck-Condon simulation. However, the vibronic bands are extremely weak (two to four orders of magnitude less than the origin). Thus, one might expect additional bands that arise from higher order effects resulting from breakdown of the double-harmonic approximation, e.g., Franck-Condon forbidden transitions which gain intensity from

anharmonicity, large-amplitude motion, coordinate dependence of the dipole moment, or vibronic coupling.

A comparison of the predicted and observed vibrational frequencies provides an additional test of the structural assignment. The calculated vibrational frequencies of all excited electronic states are nearly identical with those of the ground state (Table 3–V). Predicted frequencies for eight of the nine fundamental modes (all but ν_5) are in very good agreement with bands observed in the $\text{Ca}_2\text{}^{35}\text{Cl}_3$ spectrum. The average RMS error is 6.9% between observed frequencies and the average of the calculated frequencies (average of the $X\text{}^2A_1$, 2B_1 , 2B_2 , and 2A_2 frequencies computed at the B3LYP level).

Of the three isomers, the C_{2v} ring is therefore the only structure whose spectral properties are consistent with the observed spectrum. Furthermore, the excellent agreement between the predicted and observed vibrational frequencies provides strong quantitative support for this assignment.

3. V. b. Assignment of the excited electronic state

All four of the predicted excited electronic states of the ring isomer have similar vibrational frequencies and geometries, and are thus qualitatively consistent with the observed spectrum. However, we have seen that the observed intensity pattern and the vibrational frequencies are most consistent with assignment to the ${}^2B_2 \leftarrow X\text{}^2A_1$ transition. The Franck-Condon simulation of this transition gives the best agreement with the observed intensities of the few A_1 vibronic bands relative to the origin. Furthermore, the vibrational frequencies of the 2B_2 state at the B3LYP level are closest to the observed frequencies, with a standard deviation of 3%, while the $X\text{}^2A_1$, 2B_1 , and 2A_2 have deviations of 6%, 13%, and 4%, respectively. However, this analysis excludes

consideration of the excited 2A_1 state, for which we cannot perform geometry optimized B3LYP calculations.

The symmetry of the excited electronic state can be determined unambiguously from the rotational structure. We have simulated the rotational band contours of the origin expected for the ${}^2B_1 \leftarrow X\ {}^2A_1$, ${}^2B_2 \leftarrow X\ {}^2A_1$, and ${}^2A_1 \leftarrow X\ {}^2A_1$ transitions. The calculations were done in the rigid rotor approximation, using the B3LYP rotational constants and neglecting spin-rotation fine structure. The contour for the ${}^2B_2 \leftarrow X\ {}^2A_1$ transition, shown in Figure 3–4(a), matches the $15\ 350.8\ \text{cm}^{-1}$ band shape well. This is a *b*-type transition, which has a gap at the origin. In contrast, the ${}^2A_1 \leftarrow X\ {}^2A_1$ transition is an *a*-type transition, which would have a large central *Q* branch. Excitation to the 2B_1 state will give rise to a *c*-type transition, which also possesses strong *Q*-branches. Finally, we can rule out the 2A_2 state, because transitions to this state are dipole forbidden. Furthermore, there are no vibrational modes of A_2 symmetry, so there is no first-order mechanism for a vibronically allowed transition. Thus, from the partially resolved rotational structure we assign this spectrum to the ${}^2B_2 \leftarrow X\ {}^2A_1$ transition.

3. V. c. Assignment of the vibronic bands

3. V. c. 1. Vibronic bands of $\text{Ca}_2\ {}^{35}\text{Cl}_3$

There were 47 bands observed in the spectrum of $\text{Ca}_2\ {}^{35}\text{Cl}_3$. Of these, the 20 most intense and another eight of the weaker features were assigned to fundamental, overtones, and combination bands of the transitions to the 2B_2 excited electronic state of the C_{2v} ring structure. The band assignments, including symmetry and calculated frequencies, are included in Table 3–I. In this table, the vibrational frequencies of the overtone and combination bands are calculated from the observed fundamental

frequencies. Multiple assignments are listed where more than one is possible, and the less likely assignments are given in parenthesis.

The calculated fundamental modes have three symmetries, A_1 , B_1 , or B_2 , as listed in Table 3–V. All modes except ν_5 have been assigned to bands in the spectra. The A_1 symmetry modes observed are ν_4 , ν_6 , ν_7 , and ν_9 . The ν_4 band is the third most intense in the spectrum and about 300 times weaker than the origin. The other three are all of similar intensity, approximately 5000 times weaker than the origin. The B_2 symmetry modes observed are ν_2 and ν_8 . The ν_8 band is the strongest vibronic band after the origin and is about 40 times weaker than the origin. The ν_2 band is approximately 5000 times weaker than the origin. Two B_1 symmetry bands are observed, ν_1 and ν_3 . These bands were just slightly above noise level, even at the highest laser powers, and were therefore several orders of magnitude weaker than the A_1 and B_2 bands.

The other 20 bands we assign comprise overtones and combinations. The frequencies of the overtones and combination bands were computed empirically from the observed fundamental mode frequencies. All assigned combination bands agree to within 5 cm^{-1} with the observed band frequencies. Seven of the bands can be assigned to more than one possible combination. Five of these seven are due to the accidental resonance $3\nu_1 \sim \nu_3$, which is propagated into overtones and combinations such as $4\nu_1 \sim \nu_1 + \nu_3$ and $6\nu_1 \sim 2\nu_3$.

Of the 10 bands observed above $15\,650\text{ cm}^{-1}$, eight arise from the combinations of ν_8 with other fundamental modes including its overtone, $2\nu_8$. These combination bands have B_2 symmetry, with the exception of combinations with ν_2 and the overtone

$2\nu_8$, which are A_1 symmetry. There are therefore from nine to eleven bands of B_2 symmetry observed in the spectrum.

The B_2 modes are not Franck-Condon allowed, yet their intensities are comparable to the Franck-Condon allowed A_1 bands. The B_2 band ν_8 is the second most intense peak after the origin. This suggests that the excited electronic state may have B_2 symmetry, as Herzberg-Teller coupling could explain the vibronically allowed B_2 vibrations. Figure 3-7 shows the relative displacements of the ν_8 normal mode.

3. V. c. 2. Vibronic bands of $\text{Ca}_2^{35}\text{Cl}_2^{37}\text{Cl}$

The spectra of $\text{Ca}_2^{35}\text{Cl}_3$ and $\text{Ca}_2^{35}\text{Cl}_2^{37}\text{Cl}$ are nearly identical, except for the presence of small redshifts and splittings of some of the bands. The shifts are small near the origin, $\leq 0.1 \text{ cm}^{-1}$, and increase to 4.4 cm^{-1} at the highest frequency band. We were able to assign 37 of the 50 observed bands of $\text{Ca}_2^{35}\text{Cl}_2^{37}\text{Cl}$ on the basis of our assignment of the $\text{Ca}_2^{35}\text{Cl}_3$ spectrum. Components of split peaks were assigned to the two possible isomers of $\text{Ca}_2^{35}\text{Cl}_2^{37}\text{Cl}$, which have C_s and C_{2v} symmetry.

The observed bands, the isotopic shifts, and their assignments are listed in Table 3-II, together with predictions for the vibrational mode symmetries, and isotopomer (C_{2v} or C_s) frequencies. As in Table 3-I, the calculated frequencies of the fundamental bands were obtained from the B3LYP/6-311+G(3df) computations, while the predicted frequencies of combination bands and overtones were computed from the observed fundamental frequencies.

The calculated and observed isotopic frequency shifts of $\text{Ca}_2^{35}\text{Cl}_2^{37}\text{Cl}$ are in good agreement. Where splittings are observed, we assign the split components based on the predicted frequency shifts of the C_s and C_{2v} isomers and the relative intensity of

the components. The intensity ratio of the C_s to C_{2v} components is nearly 2:1. Both the shifts and relative intensities are consistent. In the cases where the isomers were unresolved, we have calculated average properties of both isomers.

The isotopic shifts often help to resolve ambiguities where two or more assignments in the $\text{Ca}_2^{35}\text{Cl}_3$ spectrum are possible. For example, the band at $15\,524.8\text{ cm}^{-1}$, which can be assigned to either $\nu_1+\nu_3$ or $6\nu_1$, has a redshift of 1.2 cm^{-1} . The predicted redshift for $\nu_1+\nu_3$ is 0.8 cm^{-1} , while that for $6\nu_1$ is 0.3 cm^{-1} , favoring the $\nu_1+\nu_3$ assignment. The same is true for all bands where the accidental resonance $3\nu_1 \sim \nu_3$ leads to two possible assignments. In all cases, $\nu_1+\nu_3$ or ν_3 progressions are in better agreement with the observed shifts than are the even overtones of ν_1 .

3. V. c. 3. Vibronic bands of $\text{Ca}_2^{35}\text{Cl}^{37}\text{Cl}_2$ and $\text{Ca}_2^{37}\text{Cl}_3$

The assignments of the $\text{Ca}_2^{35}\text{Cl}^{37}\text{Cl}_2$ and $\text{Ca}_2^{37}\text{Cl}_3$ bands are similar to those of $\text{Ca}_2^{35}\text{Cl}_2^{37}\text{Cl}$ and $\text{Ca}_2^{35}\text{Cl}_3$, respectively. The bands of both isotopomers are redshifted, and the shifts are largest for the heaviest isotopomer, $\text{Ca}_2^{37}\text{Cl}_3$. In three of the bands of $\text{Ca}_2^{35}\text{Cl}^{37}\text{Cl}_2$, isotopic splittings are observed. No splitting is observed in the $\text{Ca}_2^{37}\text{Cl}_3$ spectrum. The bands observed for $\text{Ca}_2^{35}\text{Cl}^{37}\text{Cl}_2$ and $\text{Ca}_2^{37}\text{Cl}_3$ are listed in Tables 3–III and 3–IV.

3. VI. Discussion

Ca_2Cl_3 has a strong origin at $15\,350.8\text{ cm}^{-1}$ (651.2 nm) and several weak but sharp vibronic bands with partially resolved rotational contours. Of the three minimum energy isomers found in the DFT calculations, a C_{2v} planar ring form is the only structure

that qualitatively and quantitatively agrees with the observed spectrum. We have assigned this spectrum to a ${}^2B_2 \leftarrow X {}^2A_1$ electronic transition of Ca_2Cl_3 of the planar C_{2v} ring geometry. The geometry and frequencies of this isomer are predicted to remain unchanged upon excitation to electronic states accessible in this spectral region. This prediction is in agreement with the prominent origin band in the observed spectrum, which is ~ 40 times more intense than the second strongest band. Franck-Condon simulations reproduce the intensity pattern, with excellent agreement for the ${}^2B_2 \leftarrow X {}^2A_1$ transition. In contrast, DFT calculations predict large changes upon excitation to the lowest states of the other isomers, the C_{2v} V structure and the D_{3h} trigonal bipyramid. The observed vibrational band spacings are in good agreement with the vibrational frequencies calculated for the ring structure, with the 2B_2 state giving the best fit. The partially resolved rotational contour matches well with a simulated b -type (B_2) transition of the ring structure, consistent with a ${}^2B_2 \leftarrow {}^2A_1$ electronic transition. The observed vibronic band spacings are in good agreement with the vibrational frequencies calculated for the ring structure, with the 2B_2 state giving the best fit.

The ν_8 band at $15\,616.7\text{ cm}^{-1}$ has a special role in this transition. It is the second strongest feature in the spectrum, despite the fact that it is not Franck-Condon allowed. Although the band is 40 times less intense than the origin, it is an order of magnitude larger than the next strongest vibronic band (a Franck-Condon allowed A_1 mode). Furthermore, most of the bands above $15\,650\text{ cm}^{-1}$ are combinations of the ν_8 band with the lower frequency vibronic bands originating from the 0-0 origin. The main spectral pattern is repeated above $15\,650\text{ cm}^{-1}$. Intensities and band positions reproduce the spectrum of the lower frequency bands combined to ν_8 .

Almost all of the Franck-Condon forbidden bands, including the ν_8 band and most of the subsequent combination bands, are of B_2 symmetry. These bands most likely gain intensity through the dependence of the transition dipole moment operator on the Q_8 normal mode, which can be estimated from the first term in a Taylor series expansion:

$$\begin{aligned} \langle B_2, \nu_8' | \mu(Q_8) | X A_1, \nu''=0 \rangle &\approx \langle B_2 | \mu_{el,0} | X A_1 \rangle \langle \nu_8' | X \nu''=0 \rangle + \\ &\langle B_2 | \partial \mu / \partial Q_8 | A_1 \rangle \langle \nu_8' | Q_8 | X A_1, \nu''=0 \rangle. \end{aligned} \quad (1)$$

The first term on the right-hand side is the standard Franck-Condon approximation. The second term is the integral of the derivative of the electronic dipole moment operator over the electronic wave functions, times an integral of the normal coordinate Q_8 over the upper and lower vibrational wavefunctions. For $\nu_8'=1$, the first term is zero.

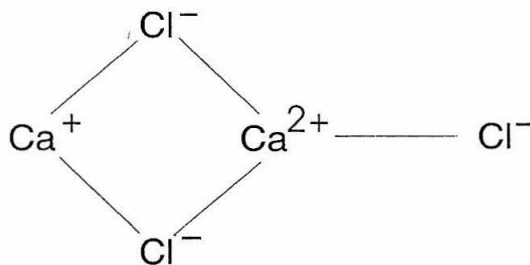
We have modeled the structure seen in each band as partially resolved rotational band contours; however, the molecule is a doublet, and spin-orbit or spin-rotation effects should also give rise to fine structure. Spin-orbit coupling should be small, as this is a nonplanar molecule for which the spin-rotation coupling is effectively the residual spin-orbit interaction.²³ Bernath and coworkers at Waterloo have observed spin-rotation splittings of $> 1 \text{ cm}^{-1}$ in CaX (X=ligand) molecules. The pure precession model for the spin-rotation parameters in doublet CaX molecules gives:^{20,22}

$$\epsilon_{aa} \approx \frac{4\Lambda^2 AA_{so}}{E(^2B_1) - E(^2B_2)} \quad (2)$$

We can estimate the magnitude of the spin-rotation interaction, if we assume a $B_2 - B_1$ splitting of 1300 cm^{-1} (the minimum consistent with our data) and the free Ca^+ ion

spin-orbit coupling of 158 cm^{-1} . In this case, we find that $\epsilon_{aa} \approx -0.03 \text{ cm}^{-1}$, much less than the splitting of the bands or the resolution of the experiment. The larger splittings seen in the systems (such as CaNH_2) studied by Whitham and Jungen and by Bernath and co-workers result from the large A rotational constants. Thus, the observed “splitting” of $\approx 1 \text{ cm}^{-1}$ in Ca_2Cl_3 is not spin-rotation fine structure, although fine structure effects may alter somewhat the predicted shapes of the rotational band contours.

The DFT calculations predict that 99.7% of the electron spin density resides on the Ca(2) atom, which possesses a charge of almost +1. Ca_2Cl_3 can thus be thought of as an ionic salt cluster of the form:



Alternatively, Ca_2Cl_3 can be considered as a Ca^+ ion bound to a CaCl_3^- ligand. The stabilization of this structure originates in the stability of the CaCl_3^- , which in turn arises from the strong attraction between the doubly charged calcium cation and the three chloride anions. The lack of any geometry change upon excitation of the Ca^+ electron indicates that the unpaired electron does not participate in any valence bonding; hence, the bonding is entirely ionic.

Localization of the unpaired electron on Ca(2) suggests that the electronic states of Ca_2Cl_3 are those of the Ca^+ ion mixed and shifted in the field of the remaining ions. A

population analysis of the orbital composition of the ground and 2B_2 states shows that the transition is from a largely Ca^+ 4s-like ground state (57% 4s, 19% 4p, 11% 3s and other) to a mostly Ca^+ 4p-character 2B_2 state (45% 4p, 28% 5p, and some contribution from Cl 4p and 5s orbitals).

Our results suggest that the Ca_2Cl_3 cluster and its low-lying excited states can be treated with a semiempirical one-electron model. One approach is to extend the ligand-field theory developed by Field and coworkers for diatomic alkaline-earth halides. The model Hamiltonian starts with free Ca^+ ion states as the zeroth order basis set and introduces a polarizable closed-shell spherical anion in cylindrical symmetry. Such a model is well suited for the ring structure, which contains the Ca^+ ion, if the polyatomic CaCl_3^- ligand is treated correctly. More generally, a pseudo-potential Hamiltonian could be used to describe a single electron moving in the field produced by two Ca^{2+} atomic ions and three Cl^- ions; such a model should be capable of treating all isomers of Ca_2Cl_3 .

We can contrast Ca_2Cl_3 , an alkaline-earth halide radical cluster, to the alkali halide cluster series M_nX_{n-1} , which also possess an excess electron. In Na_3F_2 for instance, Sence and co-workers^{11,13} have shown that the unpaired electron is not tightly bound to a single metal atom, but is in a diffuse wave function around a tail Na⁺ atom or a vacancy on an F atom. The broad features seen in the Na_3F_2 spectrum contrast with the sharp lines observed in Ca_2Cl_3 , where the electron is tightly bound to the Ca(2) atom. Excitation of the diffuse electron in Na_3F_2 is predicted to lead to large changes in the charge distribution and hence large geometry changes; thus, the overall Franck-Condon envelope is predicted to be broad and the vibronic spectra should be congested. In

addition, spectra with varying degrees of broadening have been reported for Na_2F ;¹⁵ the differences have been attributed to temperature effects.

The electronic structures of the V and bipyramid isomers differ from the ring isomer. In the ring form, the unpaired electron is localized on the Ca(2) atom, but in the higher energy V and bipyramid isomers, the Ca atoms are equivalent and share the unpaired electron. There is significant Ca - Ca bonding in the V isomer, which deviates significantly from linearity due to attraction between the Ca atoms. In the D_{3h} structure, the 0.04 eV splitting between the ground $^2A_1'$ state and the low-lying $^2A_2''$ state ($4s \sigma$ and σ^* bonding orbitals, respectively) is a direct measure of the bonding interaction between the Ca atoms, though this may be mediated by the bridging chlorine atoms. Both isomers are predicted to be metastable minima, but their energies are close to that of the ring structure, and higher level calculations are needed to confirm the relative energetics. These isomers may be formed in the nonequilibrium conditions of a supersonic jet, even if they are metastable. The CIS and DFT calculations predict that these isomers have electronic transitions in the visible or ultraviolet that lead to significant changes in cluster geometry. These spectra are expected to have strong Franck-Condon progressions.

The planar C_{2v} ring and D_{3h} bridged structures of Ca_2Cl_3 , which are nearly the same energy, are analogous to geometries found by Levy and Hargittai for Ca_2Cl_4 from B3LYP/cc-pVTZ calculations.⁶ They find that the lowest energy form of Ca_2Cl_4 is a doubly bridged (D_{2h}) structure with a planar four-member ring and two Cl⁻ tail atoms. A triply bridged (C_{3v}) isomer, similar to the D_{3h} structure presented in this work, but with the additional Cl atom in a Ca-Cl tail bond, lies only 10 kJ/mol higher. Thus, smaller alkaline-earth clusters appear to have multiple low-lying isomers, with similar structural motifs,

with competition among geometries with multiple bridging halides. Unlike the M_2X_4 dimers, however, open-shell clusters such as Ca_2Cl_3 possess electronic spectra. Since metastable isomers are readily formed and trapped in supersonic beams, the spectroscopy of radical alkaline-earth halide clusters may allow us to examine bonding and structures of various isomers of Ca_2Cl_3 and larger radical clusters.

The current work opens up many new possible directions in the spectroscopy of alkaline-earth halides. Higher level calculations of the potential energy surfaces of Ca_2Cl_3 are underway to obtain more accurate energetics and to identify reaction pathways for isomerization. Our Ca_2Cl_3 spectra have laser-limited resolution and it may be possible to obtain more detailed spectroscopic parameters from higher resolution spectra. Finally, our results suggest that one can investigate larger Ca_nCl_{2n-1} clusters, as well as the trends with substitution of other halides and other alkaline-earth metals.

3. VII. Conclusions

Spectra of the four Ca_2Cl_3 isotopomers were observed in the visible region from 15 350 to 16 000 cm^{-1} . With the aid of DFT calculations, we assigned the spectra to the ${}^2B_2 \leftarrow X {}^2A_1$ transition of the C_{2v} ring geometry isotopomers. The intensity pattern, the vibrational frequencies, and the rotational band contour were in very good agreement with the data.

Results suggest that the alkaline-earth halide excess-electron clusters may possess sharp, vibrationally and rotationally resolved electronic transitions. Thus, unlike closed shell alkaline-earth halides such as $CaCl_2$ or Ca_2Cl_4 or excess-electron alkali halide clusters. The electronic spectra can provide detailed structural information of

these salt clusters and serve as a rigorous test of semiempirical models. Such spectra would allow us to address questions concerning the importance of multiple bridging halides, the role of delocalization and metal-metal bonding, and the influence of nonadiabatic effects, e.g., Jahn-Teller distortion.

3. VIII. References

1. T. P. Martin, *Phys. Rep.* **95** 167 (1983).
2. J. Lima-de-Faria, *Structural Mineralogy: an introduction* (Dordrecht, Boston, 1994), pp. 87.
3. M. Kaupp, P. v. R. Schleyer, H. Stoll, H. Preuss, *J. Am. Chem. Soc.* **113** 6012 (1991).
4. L. Wharton, R. A. Berg, W. J. Klemperer, *J. Chem. Phys.* **39** 2023 (1963).
5. A. Buchler, J. L. Stauffer, W. J. Klemperer, *J. Am. Chem. Soc.* **86** 4544 (1964).
6. J. B. Levy and M. Hargittai, *J. Phys. Chem. A* **104** 1950 (2000).
7. M. Hargittai, *Chem. Rev.* **100** 2233 (2000).
8. T. C. Devore and J. L. Gole, *Chem. Phys.* **241** 221 (1999).
9. U. Landman, D. Scharf, J. Jortner, *Phys. Rev. Lett.* **54** 1860 (1985).
10. E. C. Honea, P. Labastie, M. L. Homer, and R. L. Whetten, *Phys. Rev. Lett.* **64** 2933 (1989).
11. G. Durand, F. Spiegelmann, Ph. Poncharal, P. Labastie, J. -M. L'Hermite, and M. Sence, *J. Chem. Phys.* **110** 7884 (1999).
12. G. Rajagopal, R. N. Barnett, A. Nitzan, U. Landman, E. C. Honea, P. Labastie, M. L. Homer, R. L. Whetten, *Phys. Rev. Lett.* **64** 2933 (1990).
13. P. Labastie, J. -M. L'Hermite, Ph. Poncharal, M. Sence, *J. Chem. Phys.* **103** 6362 (1995).
14. T. Sugai and H. Shinohara, *Chem. Phys. Lett.* **281** 57 (1997).
15. D. T. Vituccio, R. F. W. Herrmann, O. Golonzka, W. E. Ernst, *J. Chem. Phys.* **106** 3865 (1997).

16. S. F. Rice, H. Martin, R. W. Field, *J. Chem. Phys.* **82** 5023 (1985).
17. N. A. Harris and R. W. Field, *J. Chem. Phys.* **98** 2642 (1993).
18. R. W. Field and C. M. Gittins, *J. Chem. Phys.* **106** 10379 (1997).
19. N. Honjou, G. F. Adams, D. R. Yarkony, *J. Chem. Phys.* **79** 4376 (1983).
20. C. J. Whitham and Ch. Jungen, *J. Chem. Phys.* **93** 1001 (1990).
21. Z. Morbi, C. Zhao, P. F. Bernath, *J. Chem. Phys.* **106** 4860 (1997).
22. Z. Morbi, C. Zhao, J. W. Hepburn, P. F. Bernath, *J. Chem. Phys.* **108** 8891 (1998).
23. C. N. Jarman and P. F. Bernath, *J. Chem. Phys.* **98** 6697 (1993).
24. E. S. Rittner, *J. Chem. Phys.* **19** 1030 (1951).
25. D. L. Hildenbrand, *J. Chem. Phys.* **48** 1657 (1968).
26. T. Törring, W. E. Ernst, J. Kändler, *J. Chem. Phys.* **90** 4927 (1989).
27. S. L. Davis, *J. Chem. Phys.* **89** 1656 (1988).
28. L. Klynning and H. Martin, *Phys. Scr.* **24** 33 (1981).
29. S. Raouafi, G. H. Jeung, C. Jungen, *J. Mol. Spectrosc.* **196** 248 (1999).
30. K. P. Huber and G. Herzberg, *Constants of Diatomic Molecules* (Van Nostrand, New York, 1979), pp. 116-125.
31. J. M. Spotts, Ph. D. Thesis, California Institute of Technology (1999).
32. M. J. Frisch, G. W. Trucks, H. B. Schlegel, G. E. Scuseria, M. A. Robb, J. R. Cheeseman, V. G. Zakrzewski, J. A. Montgomery, Jr., R. E. Stratmann, J. C. Burant, S. Dapprich, J. M. Millam, A. D. Daniels, K. N. Kudin, M. C. Strain, O. Farkas, J. Tomasi, V. Barone, M. Cossi, R. Cammi, B. Mennucci, C. Pomelli, C. Adamo, S. Clifford, J. Ochterski, G. A. Petersson, P. Y. Ayala, Q. Cui, K. Morokuma, D. K. Malick, A. D.

Rabuck, K. Raghavachari, J. B. Foresman, J. Cioslowski, J. V. Ortiz, B. B. Stefanov, G. Liu, A. Liashenko, P. Piskorz, I. Komaromi, R. Gomperts, R. L. Martin, D. J. Fox, T. Keith, M. A. Al-Laham, C. Y. Peng, A. Nanayakkara, C. Gonzalez, M. Challacombe, P. M. W. Gill, B. Johnson, W. Chen, M. W. Wong, J. L. Andres, C. Gonzalez, M. Head-Gordon, E. S. Replogle, and J. A. Pople, Gaussian 98, Revision A.5.

33. K. Sahl, *Acta Cryst.* **19** 1027 (1965).

34. W. J. Balfour and R. F. Whitlock, *Can. J. Phys.* **53** 472 (1975).

TABLE 3-I Observed vibronic transitions of $\text{Ca}_2^{35}\text{Cl}_3$ ($m/e = 185$ amu). ν^{185} are the observed vibrational frequencies with respect to the origin. Bands are assigned to the ${}^2B_2 \leftarrow {}^2A_1$ electronic transition of the C_{2v} planar ring structure. Predicted vibrational frequencies are from B3LYP/6-311+G(3df) calculations. Combination bands are calculated with the observed fundamental vibrational frequencies.

Frequency / cm^{-1}	ν^{185} / cm^{-1}	Relative intensity ^a	Assignment ^b	Calculated frequencies		
				Fundamental (DFT) / cm^{-1}	Combination bands empirical ^{b,c} / cm^{-1}	
15 350.8	0.0	1 000.0	0 - 0			
15 380.6	29.8	w	ν_1	29.9		
15 402.2	51.5	0.1	ν_2	47.4		
15 409.9	59.1	0.1	$2\nu_1$		59.6	
15 440.0	89.3	w	ν_3	88.8		
15 453.2	102.5	w	$2\nu_2$		102.9	
15 468.0	117.3	1.7	$\nu_1 + \nu_3, (4\nu_1)$		119.1, (119.2)	
15 478.1	127.4	3.3	ν_4	123.8		
15 526.0	175.3	1.2	$2\nu_3, (6\nu_1)$		178.6, (178.8)	
15 533.0	182.3	w				
15 539.0	188.3	w	$2\nu_1 + \nu_4$		187.0	
15 546.0	195.3	w				
15 577.3	226.5	0.3	ν_6			
15 589.7	239.0	0.8	$2\nu_1 + 2\nu_3, (8\nu_1)$	230.6		
15 596.2	245.5	0.2	ν_7	247.3		
15 605.1	254.4	1.4	$2\nu_4$			
15 616.7	266.0	23.4	ν_8	260.3		
15 625.2	274.5	0.2				
15 628.9	278.2	0.7	$\nu_2 + \nu_6$		278.0	
15 640.0	289.3	w				
15 642.0	291.3	w				
15 648.0	297.3	w				
15 653.0	302.3	w				
					238.4, (238.2)	
					254.7	

TABLE 3-I

TABLE 3-I (Continuation)

Frequency / cm ⁻¹	ν^{185} / cm ⁻¹	Relative intensity ^b	Assignment ^b	Calculated frequencies	
				Fundamental (DFT) / cm ⁻¹	Combination bands empirical ^{b,c} / cm ⁻¹
15 669.0	318.3	w	$\nu_2 + \nu_8$	A ₁	317.4
15 677.0	326.3	w	$2\nu_1 + \nu_8$	B ₂	325.6
15 695.0	344.3	w		A ₁	
15 704.0	353.3	w		A ₁	
15 708.0	357.3	w		A ₁	
15 716.6	365.9	0.1	$2\nu_2 + \nu_8$	B ₂	368.9
15 725.0	374.3	w			
15 732.7	382.0	0.1	ν_9	A ₁	381.1
15 733.5	382.8	0.1	$\nu_1 + \nu_3 + \nu_8, (4\nu_1 + \nu_8), (3\nu_4)$	B ₂ , B ₂ , A ₁	385.1, (385.2), (382.2)
15 742.9	392.2	0.4	$\nu_4 + \nu_8$	B ₂	393.3
15 745.0	394.3	w			
15 791.8	441.0	0.1	$2\nu_3 + \nu_8, (6\nu_1 + \nu_8)$	B ₂	444.6, (444.8)
15 794.0	443.3	w	$\nu_2 + \nu_4 + \nu_8$	A ₁	445.0
15 803.1	452.4	0.1	$2\nu_6$	A ₁	453.1
15 828.0	477.3	w			
15 835.0	484.3	w			
15 841.0	490.3	w	$\nu_6 + \nu_8, 2\nu_7$	B ₂ , A ₁	492.5, 491.8
15 855.0	504.3	w			
15 871.0	520.3	0.1	$2\nu_4 + \nu_8$	B ₂	520.8
15 881.0	530.3	0.6	$2\nu_8$	A ₁	532.0
15 890.0	539.3	w		A ₁	
15 899.0	548.3	w			
15 903.0	552.3	w			
15 983.0	632.3	w			

^a w, weak; vw, very weak. Bands with intensity not quantified due to saturation.

^b Assignments in parentheses are less likely based on poor agreement with isotopomer shifts.

^c Combination bands calculated using the experimentally observed fundamental frequencies.

TABLE 3-I (cont.)

TABLE 3-II Observed vibronic transitions of $\text{Ca}_2^{35}\text{Cl}_2^{37}\text{Cl}$ ($m/e = 187$ amu). ν^{187} are the vibrational frequencies with respect to the origin. $\Delta\nu^{187}$ are the shifts observed relative to the frequencies of the bands of $\text{Ca}_2^{35}\text{Cl}_3$. $\Delta\nu^{\text{calc}}$ are the DFT calculated shifts. Combination bands are calculated with the observed fundamental vibrational frequencies. Split bands are assigned to the C_{2v} or C_s isomers of $\text{Ca}_2^{35}\text{Cl}_2^{37}\text{Cl}$.

Frequency / cm^{-1}	ν^{187} / cm^{-1}	Relative Intensity ^a	$\Delta\nu^{187}$ / cm^{-1}	$\Delta\nu^{\text{calc,b,c}}$ / cm^{-1}	Assignment ^b	Calculated Frequencies	
						isomer	Combination bands empirical ^{b,d} / cm^{-1}
15 350.8	0.0	1 000.0			0-0		
15 380.4	29.6	vw	0.0	0.1	ν_1	B_1/A''	
15 402.0	51.3	0.1	0.2	0.3	ν_2	B_2/A'	
15 409.5	58.8	0.2	0.4	0.1	$2\nu_1$	A_1/A'	59.3
15 439.1	88.3	vw	0.0	0.4	ν_3	B_1/A''	
15 453.2	102.5	w	0.0	0.6	$2\nu_2$	A_1/A'	102.5
15 467.3	116.5	1.7	0.7	0.5, (0.2)	$\nu_1 + \nu_3, (4\nu_1)$	A_1/A'	117.9, (118.4)
15 477.3	126.5	3.6	0.8	0.6	ν_4	A_1/A'	
15 524.8	174.0	1.8	1.2	0.8, (0.3)	$2\nu_3, (6\nu_1)$	A_1/A'	176.6, (177.6)
15 538.4	187.7	vw	0.6	0.7	$2\nu_1 + \nu_4$	A_1/A'	186.6
15 566.8	216.0	w					
15 575.5	224.7	0.4	1.8	2.2	ν_6	A'	
15 577.0	226.3	0.2	0.3	1.8	ν_6	A_1	
15 579.8	229.0	w					
15 584.7	234.0	w					
15 587.8	237.0	0.7	1.9	1.5, (0.4)	$2\nu_1 + 2\nu_3, (8\nu_1)$	A_1/A'	234.4, (234.3)
15 594.8	244.0	0.2	1.4	1.5	ν_7	A_1/A'	
15 603.7	253.0	1.4	1.2	1.3	$2\nu_4$	A_1/A'	253.1
15 612.3	261.5	w					
15 614.7	264.0	19.5	2.0	1.6	ν_8	A'	
15 616.7	266.0	10.9	0.1	0.8	ν_8	B_2	
15 623.8	273.0	0.9	1.8				
15 626.8	276.0	0.8	2.1	2.3	$\nu_2 + \nu_6$	B_2/A'	277.5

TABLE 3-II

TABLE 3-II (Continuation)

Frequency / cm ⁻¹	ν^{187} / cm ⁻¹	Relative Intensity ^a	$\Delta\nu^{187}$ / cm ⁻¹	$\Delta\nu^{\text{calc b,c}}$ / cm ⁻¹	Assignment ^b	isomer	Combination bands empirical ^{b,d} / cm ⁻¹
15 641.5	290.8	w	0.5				
15 652.5	301.8	w	0.5				
15 667.9	317.2	w	1.1	1.5	$\nu_2 + \nu_8$	A ₁ /A'	317.2
15 674.6	323.9	w	2.4	1.3	$2\nu_1 + \nu_8$	B ₂ /A'	325.2
15 693.2	342.5	w	1.8			A ₁ /A'	
15 701.6	350.9	w	2.4			A ₁ /A'	
15 705.4	354.7	w	2.6			A ₁ /A'	
15 714.0	363.3	4.9E-02	2.6	1.9	$2\nu_2 + \nu_8$	A'	366.4
15 716.6	365.9	1.9E-02	0.6	1.6	$2\nu_2 + \nu_8$	B ₂	368.4
15 722.7	372.0	w	2.3				
15 730.2	379.5	2.4E-02	2.4	1.9	ν_9	A ₁	
15 732.6	381.9	1.4E-02	0.1	0.2	ν_9	A'	
15 730.9	380.2	2.4E-02	2.6	2.2, 1.7, 2.0	$\nu_1 + \nu_3 + \nu_8, 4\nu_1 + \nu_8, 3\nu_4$	B ₂ B ₂ A ₁	381.9, 380.5, 380.0
15 733.5	382.8	9.3E-03	0.0	1.2, 1.1, 1.8	$\nu_1 + \nu_3 + \nu_8, 4\nu_1 + \nu_8, 3\nu_4$	B ₂ B ₂ A ₁	383.8, 382.4, 382.2
15 740.7	390.0	0.3	2.2	2.2	$\nu_4 + \nu_8$	A'	391.4
15 742.9	392.2	0.2	0.0	1.5	$\nu_4 + \nu_8$	B ₂	393.3
15 743.2	392.5	w	1.8				
15 788.6	437.9	4.6E-02	3.2	2.7, (1.8)	$2\nu_3 + \nu_8, (6\nu_1 + \nu_8)$	A'	438.0 (441.6)
15 791.6	440.9	2.6E-02	0.2	1.4, (1.2)	$2\nu_3 + \nu_8, (6\nu_1 + \nu_8)$	B ₂	439.9 (442.6)
15 799.4	448.7	3.8E-02	3.7	4.4	$2\nu_6$	A'	449.4
15 803.1	452.4	5.0E-02	0.0	3.7	$2\nu_6$	A ₁	452.5
15 840.1	489.4	w	0.9	3.2, 3.0	$\nu_6 + \nu_8, 2\nu_7$	B ₂ , A ₁ /A'	492.2, 488.0
15 868.6	517.9	0.1	2.4	2.8	$2\nu_4 + \nu_8$	A'	517.1
15 869.7	519.0	0.1	1.3	2.1	$2\nu_4 + \nu_8$	B ₂	520.6
15 876.6	525.9	0.5	4.4	3.2	$2\nu_8$	A'	528.0
15 881.0	530.3	0.3	0.0	1.6	$2\nu_8$	A ₁	531.8

105

TABLE 3-II (cont.)

^a w, weak; vw, very weak. Bands with intensity not quantified due to saturation.^b Assignments in parentheses are less likely based on poor agreement with isotopomer shifts.^c From DFT calculations. For the bands with unresolved splittings we report the average shift of the C_{2v} and C_s isomers.^d Calculated using the experimentally observed fundamental frequencies.

TABLE 3-III Observed vibronic transitions of $\text{Ca}_2^{35}\text{Cl}^{37}\text{Cl}_2$ ($m/e = 189$ amu). ν^{189} are the vibrational frequencies with respect to the origin. $\Delta\nu^{189}$ are the shifts observed relative to the frequencies of the bands of $\text{Ca}_2^{35}\text{Cl}_3$. $\Delta\nu^{\text{calc}}$ are the DFT calculated shifts. Combination bands are calculated with the observed fundamental vibrational frequencies. Split bands are assigned to the C_{2v} or C_s isomers of $\text{Ca}_2^{35}\text{Cl}^{37}\text{Cl}_2$.

Frequency / cm^{-1}	ν^{189} / cm^{-1}	$\Delta\nu^{189}$ / cm^{-1}	$\Delta\nu^{\text{calc a,b}}$ / cm^{-1}	Assignment ^a	isomer	Combination bands empirical ^{a,c} / cm^{-1}
15 351	0			0 - 0		
15 402	51	1	1	ν_2	B_2/A'	
15 409	58	1	0	$2\nu_1$	A_1/A'	
15 452	102	1	1	$2\nu_2$	A_1/A'	102
15 467	116	1	0, (0)	$\nu_1 + \nu_3, (4\nu_1)$	A_1/A'	116, (116)
15 477	126	1	1	ν_4	A_1/A'	
15 524	174	2	2, (1)	$2\nu_3, (6\nu_1)$	A_1/A'	174, (174)
15 574	223	3	4	ν_6	A_1	
15 575	224	2	4	ν_6	A'	
15 586	235	4	3, (1)	$2\nu_1 + 2\nu_3, (8\nu_1)$	A_1/A'	232, (232)
15 594	243	2	3	ν_1	A_1/A'	
15 602	251	3	3	$2\nu_4$	A_1/A'	252
15 613	263	3	4	ν_8	B_2	
15 615	264	2	2	ν_8	A'	
15 624	273	2	5	$\nu_2 + \nu_6$	B_2/A'	275
15 625	274	4	4			
15 640	289	0	3	$\nu_2 + \nu_8$	A_1/A'	315
15 664	314	5	3	$2\nu_1 + \nu_8$	B_2/A'	322
15 671	320	6	3		A_1/A'	
15 702	352	6	6		B_2/A'	
15 712	361	5	4	$2\nu_2 + \nu_8$	B_2/A'	366
15 720	370	5	5			

TABLE 3-III

TABLE 3-III (Continuation)

Frequency / cm^{-1}	ν^{189} / cm^{-1}	$\Delta\nu^{189}$ / cm^{-1}	$\Delta\nu^{\text{calc a,b}}$ / cm^{-1}	Assignment ^a	isomer	Combination bands empirical ^{a,c} / cm^{-1}
15 728	377	4	2	ν_9	A_1/A'	
15 731	380	3	3, 3, 4	$\nu_1 + \nu_3 + \nu_8, 4\nu_1 + \nu_8, 3\nu_4$	$B_2, B_2, A_1/A'$	380, 380, 378
15 739	388	4	5	$\nu_4 + \nu_8$	B_2/A'	389
15 743	392	0	3	$\nu_4 + \nu_8$	A'	390
15 786	435	6	6, (4)	$2\nu_3 + \nu_8, (6\nu_1 + \nu_8)$	B_2/A'	438, (438)
15 788	438	6	6, 4	$2\nu_3 + \nu_8, \nu_2 + \nu_4 + \nu_8$	$B_2, A_1/A'$	438, 442
15 800	449	3	8	$2\nu_6$	A_1/A'	446
15 849	498	6				

^a Assignments in parentheses are less likely based on poor agreement with isotopomer shifts.

^b From DFT calculations. For the bands with unresolved splittings we report the average shift of the C_{2v} and C_s isomers.

^c Calculated using the experimentally observed fundamental vibrational frequencies.

TABLE 3-III (cont.)

TABLE 3-IV Observed vibronic transitions of $\text{Ca}_2\text{}^{37}\text{Cl}_3$ ($m/e = 191$ amu). Δv^{191} are the shifts observed relative to the frequencies of the bands of $\text{Ca}_2\text{}^{35}\text{Cl}_3$. Δv^{calc} are the calculated values. Predicted vibrational frequencies are from B3LYP/6-311+G(3df) calculations.

Frequency / cm^{-1}	v^{191} / cm^{-1}	Δv^{191} / cm^{-1}	Δv^{calc} / cm^{-1}	Assignment ^a	Combination bands empirical ^{a,b} / cm^{-1}
15 351	0	0		0-0	
15 401	50	1	1	ν_2	B_2
15 409	58	1	0	$2\nu_1$	A_1
15 452	101	1	2	$2\nu_2$	A_1
15 466	115	2	1, (1)	$\nu_1 + \nu_3, (4\nu_1)$	100 115, (116)
15 476	125	2	2	ν_4	A_1
15 523	172	3	2, (1)	$2\nu_3, (6\nu_1)$	A_1
15 574	223	3	6	ν_6	A_1
15 587	236	3	3, (1)	$2\nu_1 + 2\nu_3, (8\nu_1)$	230, (232)
15 592	241	4	4	ν_7	A_1
15 601	250	4	4	$2\nu_4$	A_1
15 613	262	4	4	ν_8	B_2
15 620	269	4	4		
15 624	273	5	7	$\nu_2 + \nu_6$	B_2
15 727	377	5	4	ν_9	A_1
15 738	388	5	6	$\nu_4 + \nu_8$	B_2
15 785	434	7	6, (5)	$2\nu_3 + \nu_8, (6\nu_1 + \nu_8)$	444, (443)

^a Assignments in parentheses are less likely based on poorer agreement with isotopomer shifts.

^b Calculated using the experimentally observed fundamental frequencies.

TABLE 3-IV

TABLE 3-V Calculated geometries, energies, and vibrational frequencies of the lowest-lying states of the C_{2v} planar ring $Ca_2^{35}Cl_3$ structure. From B3LYP/6-311+G(3df) calculations, unless otherwise noted.

Coordinates	X^2A_1	2B_1	2B_2	2A_1	2A_2	Experiment
r_1 (Å)	2.463	2.463	2.467		2.485	
r_2 (Å)	2.651	2.652	2.644		2.623	
r_3 (Å)	2.666	2.658	2.666		2.731	
α (deg.)	93.0	91.5	92.8		92.3	
β (deg.)	87.3	88.7	87.7		89.9	
<u>Electrostatic parameters</u>						
μ (Debye)	4.582	5.016	5.243		10.413	
α^a	587.379	300.035	569.212		286.257	
<u>Energetics (adiabatic states)</u>						
E_{el} (hartree)	MP2/6-311+G(2d,p)	-2 733.28466				
E_{el} (hartree)		-2 736.21124	-2 736.15985	-2 736.15407		-2 736.14151
E_0 (hartree)		-2 736.20759	-2 736.15656	-2 736.15039		-2 736.13803
ΔE_0 (eV)	(relative to X^2A_1)	0.00	1.389	1.556	1.893	1.9033 ^a
ΔE_{el} (eV)	CIS/6-311+G(d)	0.00	1.925	2.132	2.349	
ΔE_{el} (eV)	CIS/6-311+G(2d)	0.00	1.790	2.042	2.181	3.162
ΔE_{el} (eV)	CIS/6-311+G(3df)	0.00	1.747	2.013	2.142	3.058
ΔE_0 (eV)	CIS/6-311+G(3df)	0.00	1.748	2.014	2.141	3.064

TABLE 3-V

TABLE 3-V (Continuation)

Vibrational frequencies	X^2A_1	2B_1	2B_2	2A_1	2A_2	Experiment
ν_1 (cm^{-1})	30.2	18.4	29.9	37.0 *	30.2	29.8
ν_2 (cm^{-1})	48.8	48.7	47.4	50.6 *	51.6	51.5
ν_3 (cm^{-1})	75.1	86.2	88.8	67.5 *	92.4	89.3
ν_4 (cm^{-1})	116.8	114.1	123.8	118.6 *	114.2	127.4
ν_5 (cm^{-1})	207.7	220.7	205.0	215.4 *	151.6	N/Obs
ν_6 (cm^{-1})	225.6	226.0	230.6	218.6 *	211.6	226.5
ν_7 (cm^{-1})	249.3	250.7	247.3	245.3 *	233.7	245.5
ν_8 (cm^{-1})	265.3	269.1	260.3	263.6 *	263.2	266.0
ν_9 (cm^{-1})	382.1	381.4	381.1	381.3 *	374.4	381.1

^a Observed optical transition^b Trace of polarizability tensor ($\alpha_{xx} + \alpha_{yy} + \alpha_{zz}$)

* CIS/6-311+G(3df)

TABLE 3-V (cont.)

TABLE 3–VI Calculated properties of two higher energy isomers of Ca_2Cl_3 . See Fig. 6 for atom definition. From B3LYP/6-311+G(3df) calculations, unless otherwise noted.

	C_{2v} planar V structure	D_{3h} trigonal bipyramid structure
<u>Coordinates</u>		
r_1 (Å)	Ca(1)-Cl(1)	X^2A_1'
r_2 (Å)	Ca(1)-Cl(2)	2.663
α (deg.)	Ca(1)-Cl(2)-Ca(1)	3.593
β (deg.)	Cl(1)-Ca(1)-Cl(2)	84.9
		77.6
		r_1 (Å)
		r_2 (Å)
		α (deg.)
		β (deg.)
		Ca-Cl
		Cl-Cl
		Cl-Ca-Cl
		Ca-Cl-Ca
<u>Energetics</u>		
E_{el} (hartree)	MP2/6-311+G(2d)	-2 733.27169
ΔE_{el} (kJ/mol)	relative to E_{el} (ring)	34.065
E_{el} (hartree)	B3LYP/6-311+G(2d)	-2 736.19526
E_0 (hartree)	B3LYP/6-311+G(2d)	-2 736.19149
ΔE_0 (kJ/mol)	relative to E_0 (ring)	20.647
<u>Vibrational Frequencies</u>		
ν_1 (cm^{-1})	B_1	E
ν_2 (cm^{-1})	A_2	A_2''
ν_3 (cm^{-1})	A_1	E'
ν_4 (cm^{-1})	B_2	A_1'
ν_5 (cm^{-1})	A_1	E
ν_6 (cm^{-1})	B_2	A_1'
ν_7 (cm^{-1})	A_1	
ν_8 (cm^{-1})	B_2	
ν_9 (cm^{-1})	A_1	
		ν_1 (cm^{-1})
		ν_2 (cm^{-1})
		ν_3 (cm^{-1})
		ν_4 (cm^{-1})
		ν_5 (cm^{-1})
		ν_6 (cm^{-1})
		3.8
		27.0
		35.7
		55.6
		96.0
		207.8
		244.0
		366.3
		387.4

TABLE 3–VI

TABLE 3-VI (Continuation)

C _{2v} planar V structure			D _{3h} trigonal bipyramid structure		
State	ΔE_{el} (eV)	Oscillator Strength	State	ΔE_{el} (eV)	Oscillator Strength
² B ₁	2.1815	0.1735	² A ₂ "	0.040	0.0291
² B ₂	2.8026	0.2698	² E'	1.775	0.2336
² A ₁	3.1789	0.0027	² E"	1.834	0.0000
² A ₁	3.5842	0.1837	² A ₁ '	2.2642	0.0000
² A ₂	4.5466	0.0000	² A ₁ '	2.4432	0.0000
			² A ₂ "	2.505	0.0748

Excited Electronic states CIS/6-311+G(3df) (vertical transitions)

TABLE 3-VI (cont.)

3. IX. Figure captions

Figure 3–1 Laser vaporization source. The calcium rod was ablated at the throat of a supersonic expansion of a CCl_4/Ar mixture.

Figure 3–2 Multiphoton Time-of-Flight (TOF) mass spectrum. Spectrum was recorded by ionizing with 651 nm and 308 nm radiation. Inset: Ca_2Cl_3 isotopomer peaks. Relative intensities of the Ca_2Cl_3 peaks are close to those expected from the natural chlorine isotope abundances.

Figure 3–3 (a) Electronic $1+1'$ REMPI spectrum of $\text{Ca}_2^{35}\text{Cl}_3$ ($m/e = 185$ amu). All bands beyond origin are magnified by X36 (b) Stick spectrum of $\text{Ca}_2^{35}\text{Cl}_3$ plotted on a log scale. Dotted lines indicate weak and very weak bands for which the intensities were not quantified due to saturation.

Figure 3–4 Overlaid vibronic bands of the isotopomers $\text{Ca}_2^{35}\text{Cl}_3$ (185 amu, solid line) and $\text{Ca}_2^{35}\text{Cl}_2^{37}\text{Cl}$ (187 amu, dotted line). (a) Origin at $15\,350.8\text{ cm}^{-1}$ with a simulation of b -type rotational contour at 9 K (offset curve) (b) ν_8 at $15\,616.7\text{ cm}^{-1}$ and (c) $2\nu_8$ at $15\,881\text{ cm}^{-1}$ bands.

Figure 3–5 Comparison of a portion of the spectra of $\text{Ca}_2^{35}\text{Cl}_3$ (185 amu, solid line) and $\text{Ca}_2^{35}\text{Cl}_2^{37}\text{Cl}$ (187 amu, dotted line).

Figure 3–6 Structures of Ca_2Cl_3 predicted by B3LYP/[6-311G+(3df)] density functional theory calculations. (a) C_{2v} planar V, (b) D_{3h} trigonal bipyramid, and (c) C_{2v} planar ring.

Figure 3-7 Displacement for the ν_8 normal mode of the C_{2v} planar ring structure.

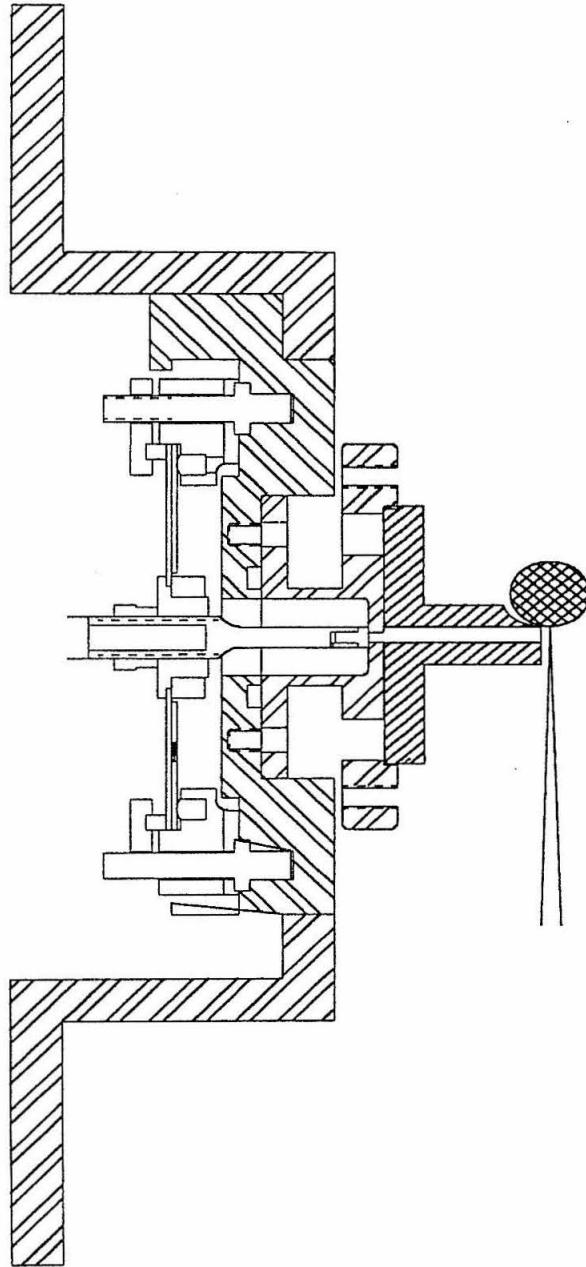


Figure 3-1

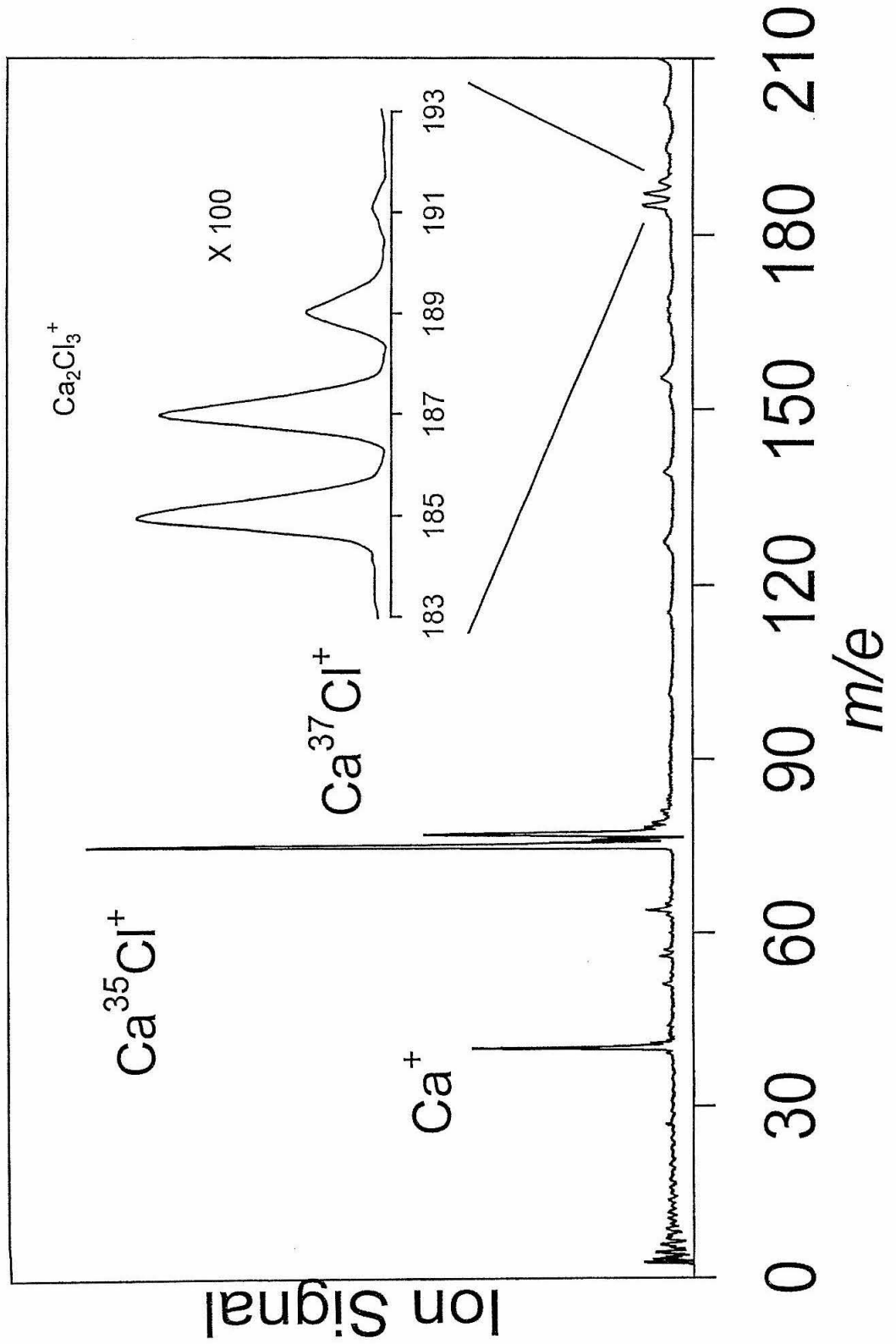
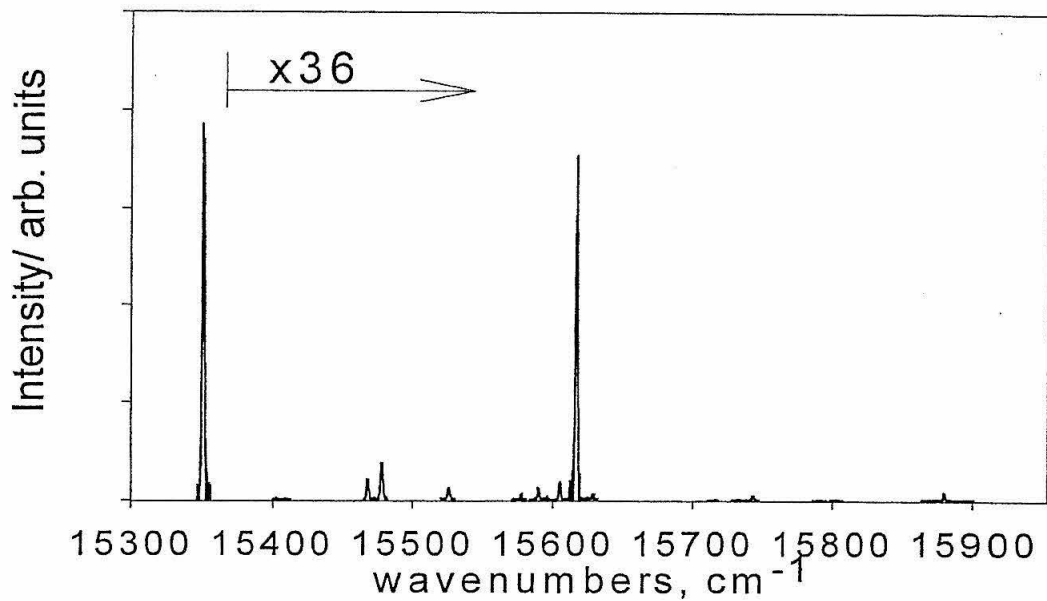


Figure 3-2

(a)



(b)

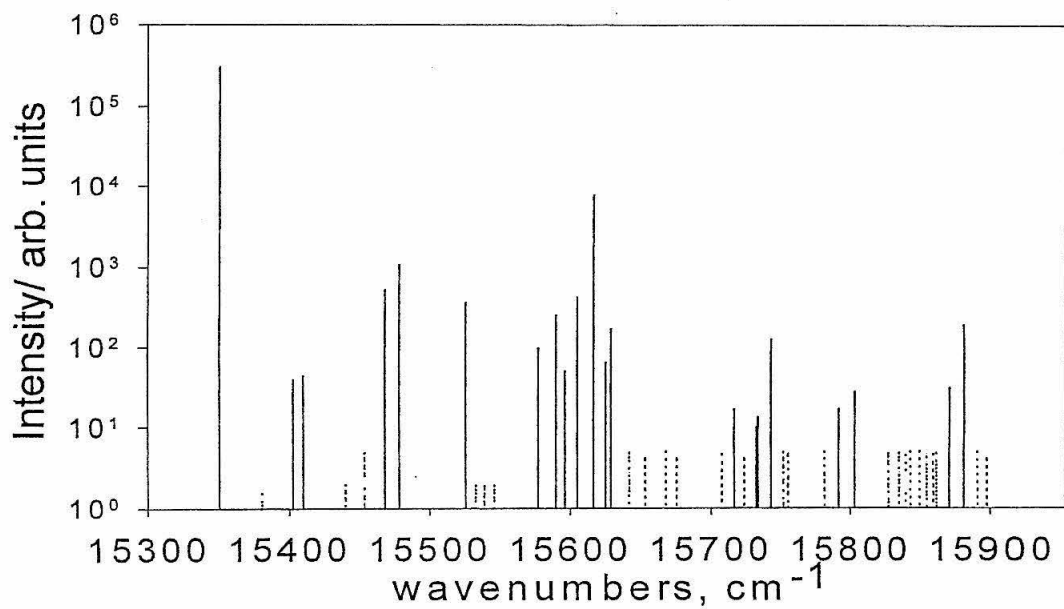


Figure 3-3

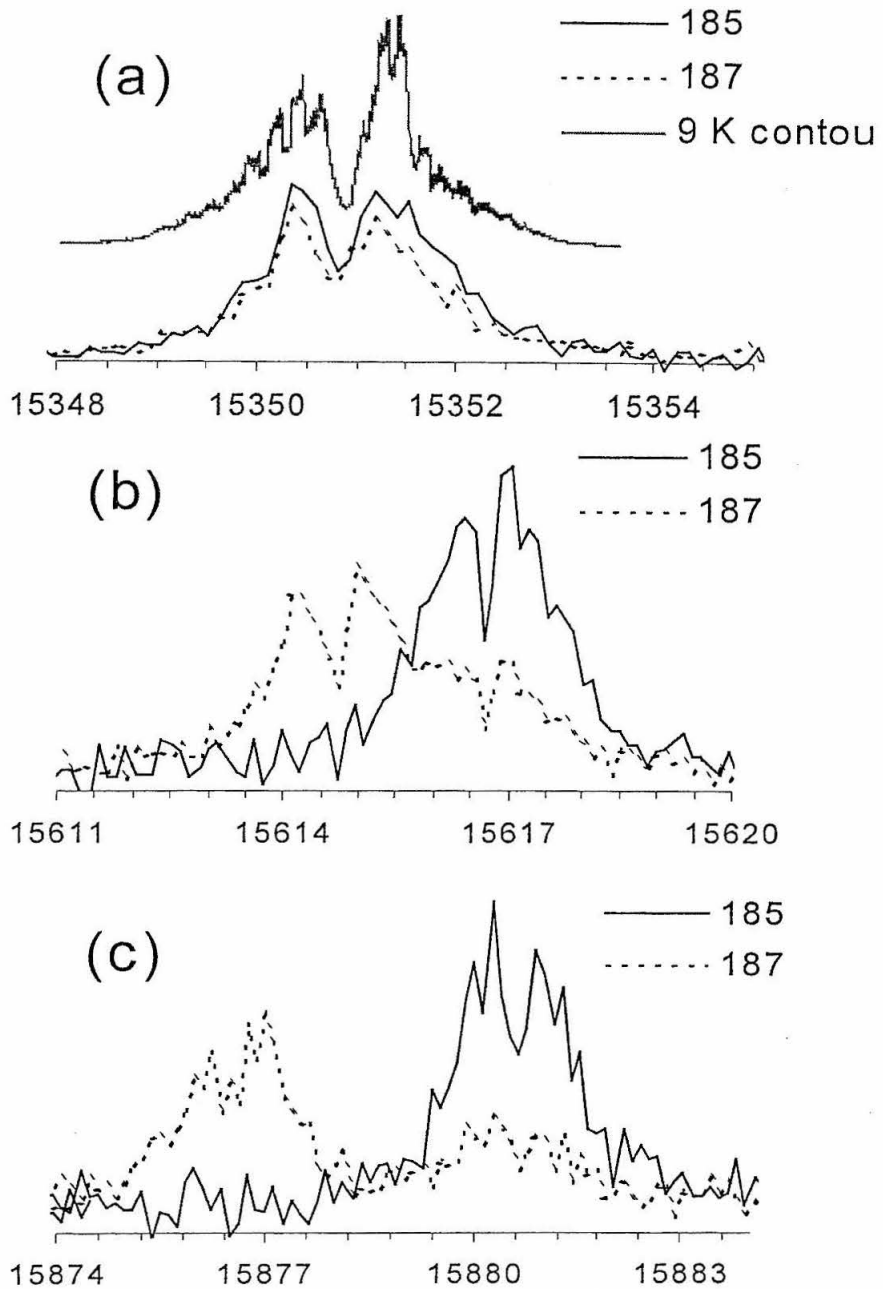


Figure 3-4

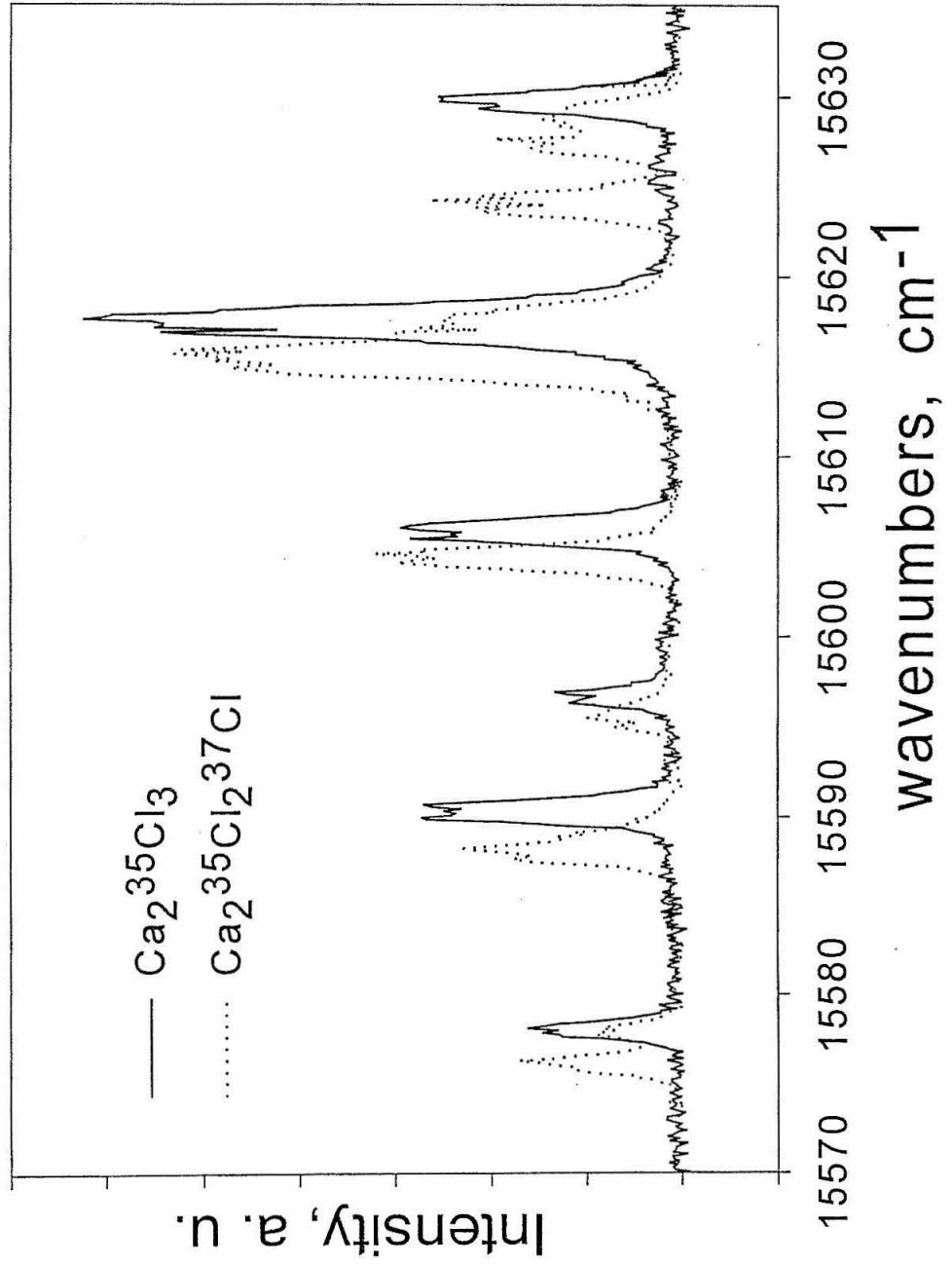


Figure 3-5

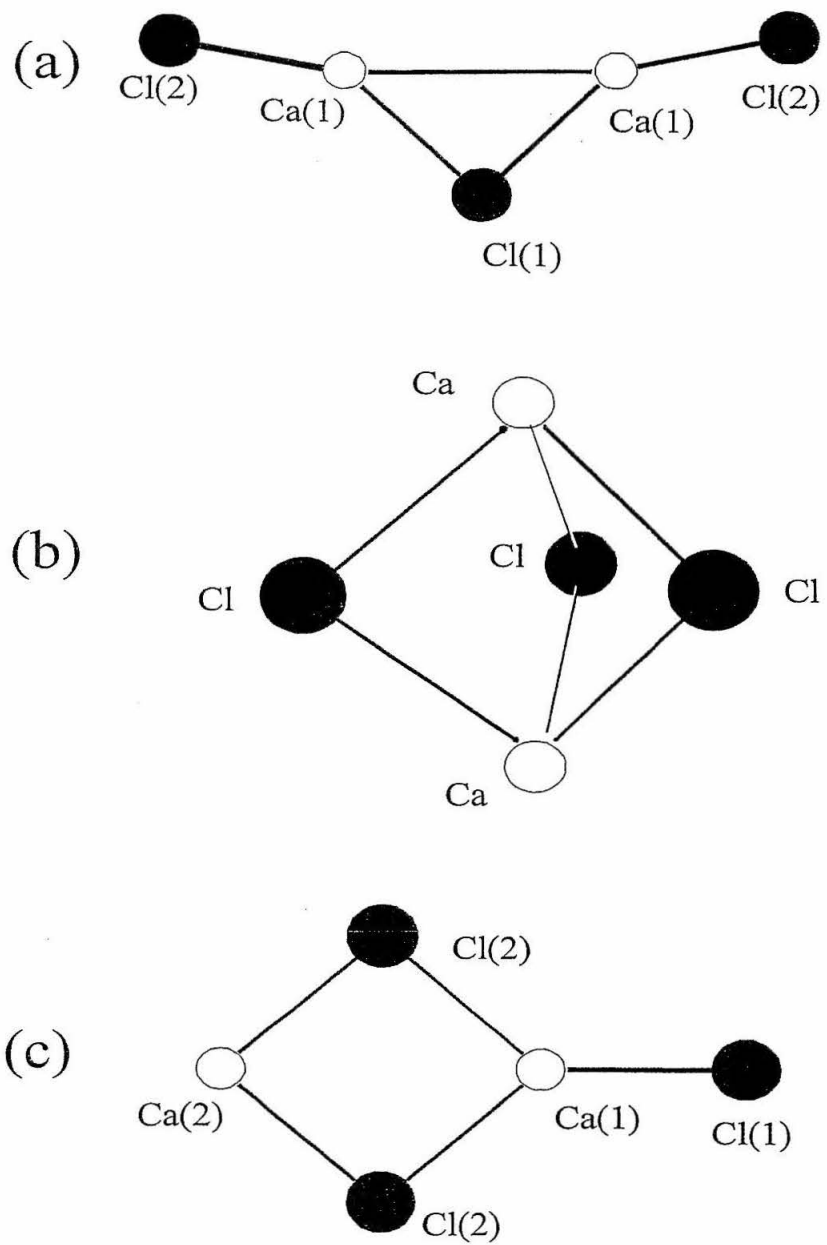


Figure 3-6

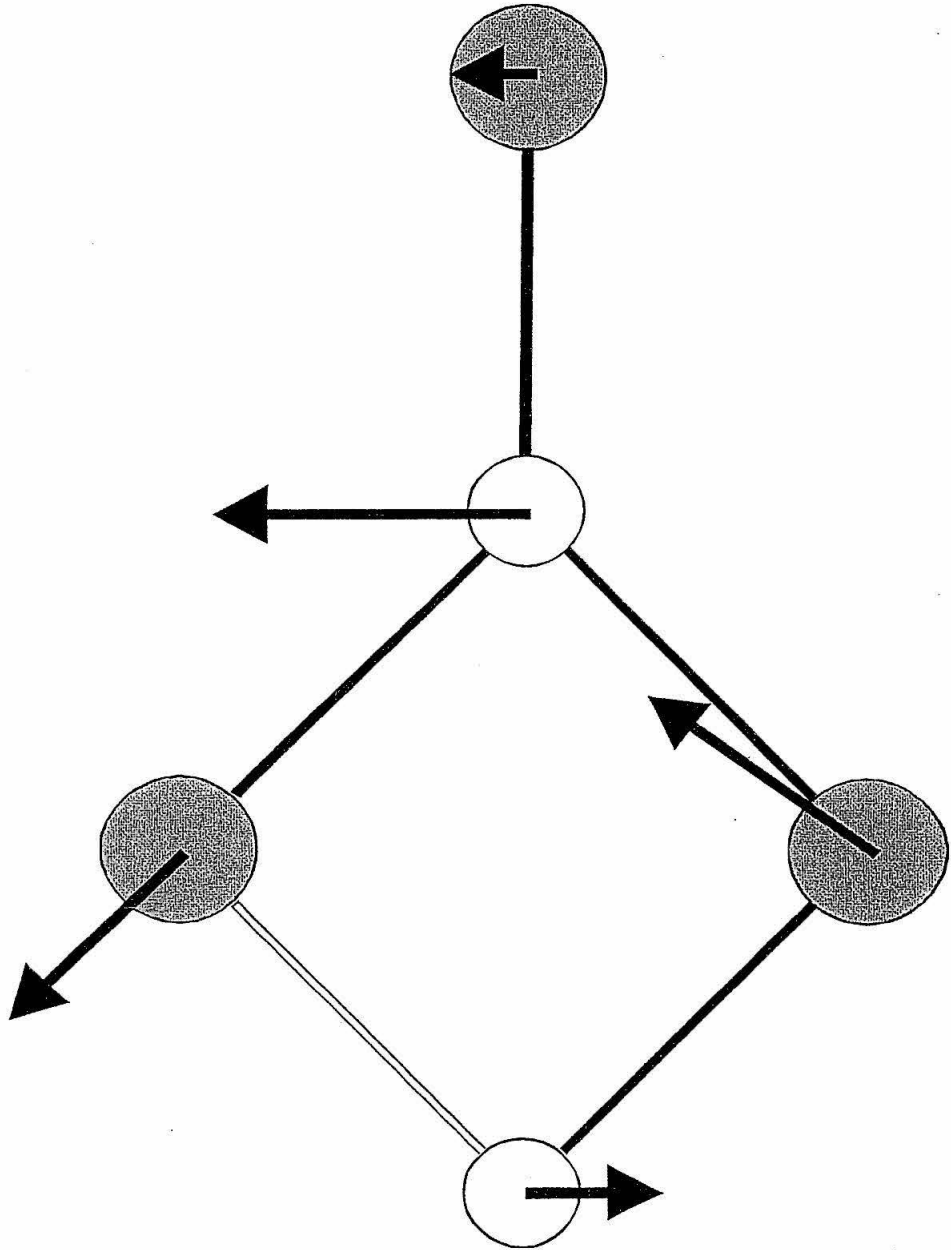


Figure 3-7

Chapter 4

720 nm band system of Ca_2Cl_3 .

4. I. Introduction

Alkaline-earth halide clusters of composition M_nX_{2n-1} , such as Ca_2Cl_3 , possess a non-valence electron. These clusters are model systems for the study of fundamental interactions in salt aggregates. The advantages are the computational tractability via pseudopotential methods and the spectroscopic accessibility of the non-valence electron.

While several groups have studied properties of the alkali halide clusters,^{1,2,3,4,5} there have been few reports of experimental measurements of alkaline-earth halide clusters. The non-valence electron is more likely to be closely bound to the metal centers in the alkaline-earth halides due to the higher charge (+2) of the alkaline-earth atoms. As in the case of the ring geometry of Ca_2Cl_3 , presented in Chapter 3 of this work, the localization of the non-valence electron on one of the Ca atoms led to sharp spectroscopic features.

The sharp features observed in the Ca_2Cl_3 spectra and density functional theory calculations led to the assignment of the spectrum at 650 – 630 nm to the ${}^2B_2 \leftarrow X {}^2A_1$ transition of the ring structure.⁶ Quantum chemistry calculations predict two other accessible excited states for the ring geometry. One 2B_1 state is predicted to be lower than the observed 2B_2 state by 0.15 eV (B3LYP) or 0.2 eV (CIS). A 2A_1 symmetry state higher in energy is also predicted. These three states, the observed 2B_2 , the 2B_1 , and the 2A_1 correspond to the mostly $Ca^{2+} 4p$ character states. The 2A_1 corresponds to the axis of the molecule, 2B_1 to the axis perpendicular to the plane of the ring, and 2B_2 to the axis parallel to the ring. The spectra of the transitions to the 2A_1 and 2B_1 states should be similar to the observed spectra at 650 nm, as the geometry remains largely unchanged for these low lying excited states.⁶ Observation of either of these electronic bands of the C_{2v} ring structure would provide further confirmation of the assignment to the 2B_2 band. It

would also allow the comparison of the Herzberg-Teller coupled B_2 symmetry vibronic bands observed in the 651 nm spectra with the B_1 modes which might be observable in the ${}^2B_1 \leftarrow X {}^2A_1$ transition, and with the absence of B_1 and B_2 modes in the 2A_1 transition.

The study of small metal halide clusters is enriched by the possibility of multiple isomers. For Ca_2Cl_3 , in addition to the C_{2v} ring structure studied,⁶ there are at least three other possible stable geometries, a V-shaped C_{2v} , a distorted trigonal bipyramid C_{3v} , and a rhombus C_s structures. These structures are predicted to have transitions in the visible spectral range and should be amenable to spectroscopic investigation.

The V-shaped structure resembles a linear configuration that is distorted into a V-shape due to Ca – Ca bonding. The excitation of the excess-electron to an excited $4\sigma^*$ repulsive state, or to a p -character excited state may lead to repulsion of the Ca atoms and therefore to a nonadiabatic distortion to a linear conformation.

Recent calculation by Glezakou⁷ and in our group have found that the D_{3h} structure, which is also discussed in Chapter 3 of this work, distorts to a C_{3v} structure. One Ca atom moves closer to the plane containing the three chlorines and the other moves away. (See Figure 4–1) For the symmetric D_{3h} structure the Ca atoms are similar and the non-valence electron is equally shared between them. When distorted to C_{3v} symmetry the electron becomes unequally shared. One may then expect a coupled motion of the electron with the vibration. The D_{3h} and the C_{3v} structures also have degenerate excited states that lead to Jahn-Teller distortion of some of the electronically excited states. In this case the E' states of the D_{3h} structure will distort to C_{2v} symmetry, and the C_{3v} structure will distort to a C_s symmetry rhombus structure. Balasubramanian and coworkers⁸ have calculated similar structures for the mixed pentamer clusters of Al and As.

To address the presence of the ${}^2B_1 \leftarrow X {}^2A_1$ transition of the ring isomer, or transitions of the other three isomers, we conducted 1 + 1' REMPI experiments in the spectral range where we expected to observe some of these transitions: 13 500 – 14 700 cm^{-1} (1.67 – 1.82 eV). The spectra are presented here together with Configuration Interaction-Singles (CIS) and Hartree-Fock (HF) calculations aimed at interpreting the spectra. We performed calculations on a V-shaped C_{2v} structure, a distorted trigonal bipyramidal C_{3v} structure, and a rhombus C_s structure.

4. II. Experiment

The experimental apparatus is the same previously described in Chapter 3 of this work. The scanned region was extended to the 13 500 – 14 700 cm^{-1} visible range. LDS 722 laser dye was used to generate approximately 5 mJ in the 720nm range. 1+1' REMPI spectra were obtained for $\text{Ca}_2 {}^{35}\text{Cl}_3$ and the mono-substituted $\text{Ca}_2 {}^{35}\text{Cl}_2 {}^{37}\text{Cl}$ - isotopomer. In the experiment, the dye laser power was optimized for Ca_2Cl_3 signal. Therefore, it is likely that the spectra are saturated, and that the relative band intensities displayed are not correct.

4. III. Experimental Results

4. III. a. Spectrum of $\text{Ca}_2 {}^{35}\text{Cl}_3$

The spectrum of $\text{Ca}_2 {}^{35}\text{Cl}_3$ is displayed in Figure 4–2. We observe a broad envelope with two distinct regions. The bands from 13 524 cm^{-1} to approximately 13 900 cm^{-1} show a general trend of increasing intensity with wavenumber. The trend is apparent in different scans, however, as stressed above some of the bands may be

saturated. Bands are observed up to $14\,700\text{ cm}^{-1}$. The transition is in sharp contrast to the $15\,351\text{ cm}^{-1}$ band. It was not possible to distinguish an origin of the transition and it was not possible to identify progressions. An attempt of scanning to the red to locate the origin of the band was unsuccessful. The intensity of the absorptions decreased significantly below $13\,500\text{ cm}^{-1}$, below which no bands were observed. The congested spectrum does however suggest some repeated vibrational spacings of approximately 21, 24, 90 and 105 cm^{-1} in the low energy end of the spectrum (below $13\,900\text{ cm}^{-1}$).

4. III. b. Spectrum of $\text{Ca}_2^{35}\text{Cl}_2^{37}\text{Cl}$

The spectrum for $\text{Ca}_2^{35}\text{Cl}_2^{37}\text{Cl}$ is shown in Figure 4–3. The spectrum is similar to the 185 isotopomer in that it is congested, the origin is not apparent and there are no recognizable patterns. By looking at the red shifts of the heavier isotopomer with respect to the lighter, (See Figure 4–4) we observe a reproducible shift of $\sim 4.5\text{ cm}^{-1}$ for most bands on the red side of the spectra (below $13\,900\text{ cm}^{-1}$). For the bands above $13\,900\text{ cm}^{-1}$ the red shift is not clearly discernible.

4. IV. Quantum chemistry calculations

4. IV. a. Ground state geometries

Ab initio calculations were performed using the Gaussian98⁹ software package. Geometries were optimized and vibrational frequencies calculated using the Hartree-Fock (HF) level of theory and the 6-311+G(3df) basis set for the ground state structure. Optimized ground state geometries, energies and frequencies of the C_{2v} planar V, the C_{3v} distorted trigonal bipyramid, and the C_s rhombus are presented in Tables 4–1, 4–2 and 4–3, respectively.

4. IV. a. 1 Ground state of the C_{2v} V-shaped structure

The ground state C_{2v} V structure has been described in Chapter 3 of this work. The structure is shown in Figure 4–1. The geometry, energy and vibrational frequencies are listed in Table 4–1.

4. IV. a. 2 Ground state of the C_{3v} distorted trigonal bipyramid

The D_{3h} symmetry structure has been described in Chapter 3. Briefly, it consists of three Cl atoms at the edges of an equilateral triangle, with both Ca atoms positioned equidistant above and below the plane formed by the Cl atoms. One of the vibrational frequencies, ν_3 , of the D_{3h} structure is a high intensity mode (520 kM/mol) that distorts to the C_{3v} structure by having both Ca atoms translate along the z-axis. One Ca atom moves closer to the Cl atoms, while the other moves apart from the Cl atoms. At the Hartree Fock level and the 6-311G+(3df) basis set, the D_{3h} structure is nearly 33.8 kJ/mol less stable than the C_{3v} symmetry structure. The C_{3v} is therefore 42.9 kJ/mol above the lowest energy C_{2v} ring geometry. According to the higher level calculation of Glezakou and Taylor (ROMP2/SBKJC(d)),⁷ The energy difference is nearly 50 kJ/mol upon relaxation from D_{3h} to the C_{3v} structure. In the HF/6-311G+(3df) calculation, the Ca atom nearer to the chlorines is 1.69 Å from the plane containing the Cl atoms. The other Ca is 2.18 Å away. The electron is mostly localized on the Ca atom that is furthest away from the chlorine atoms. The coefficients for electron spin are 0.847 and 0.158 for each calcium atom. The dipole moment increases to 9.3 D in the C_{3v} structure. The lowest frequency vibration is at 113 cm^{-1} and the highest at 318.5 cm^{-1} .

4. IV. a. 3 Ground state of the C_s rhombus

The rhombus state is reached by distorting the equilateral triangle formed by the three chlorine atoms. A similar distortion in the D_{3h} symmetry structure would lead to a C_{2v} geometry. The rhombus structure optimized was higher in energy than the C_{3v} distorted trigonal bipyramid by 55.1 kJ/mol. Vibrational frequencies are near the frequencies calculated for the C_{3v} structure ranging from 115.6 to 321.5 cm^{-1} .

4. IV. b. Excited electronic states

Excited electronic states of the V and C_{3v} and C_s geometries were calculated using the CIS method with the 6-311+G(3df) basis set. Convergence was reached for the lowest-lying excited states of the V structure, but not for the other two isomers. The best non-converged excited states are listed in Tables 4–2 and 4–3. Vertical transition energies are also included in those tables. The electronic transitions, geometries and vibrational frequencies of the excited states are presented in Tables 4–1 through 4–3.

4. IV. b. 1 Excited electronic states of the C_{2v} V-shaped structure

Table 4–1 lists the geometries, vibrational frequencies and adiabatic transition energies between the ground and lowest excited states of the V structure. The lowest 2B_1 state has geometry close to the ground state, yet with a notable lengthening of the Ca – Ca bond length, which is 3.800 Å in the ground state and 3.969 Å in the 2B_1 excited state. The Cl – Ca – Cl central angle increases correspondingly from 89.0 to 95.5 degrees. The adiabatic excitation energy is 2.18 eV after optimization of the excited state at the CIS/6-311-G(3df) level. The next electronic state calculated is a 2B_2 , which has a vertical transition energy of 2.377 eV. An attempt to optimize the excited state led the calculation toward a linear structure, with a large change in geometry. After breaking

symmetry the state converged to a Σ_u state 0.856 eV above the ground state V. Both V and linear geometries calculated are not stable minima, as they possess imaginary frequencies. Both structures have low frequency modes 30.6, 36.6, 50.5 and 61.5 cm^{-1} in the excited V state and 7.35 cm^{-1} in the linear excited state.

4. IV. b. 2 Excited electronic states of the C_{3v} distorted trigonal bipyramide structure

We calculated the two lowest-lying excited states for the C_{3v} geometry. The first excited state has A_1 symmetry. There are changes in geometry from the ground state to the excited states $\Delta r1 = 0.86$, $\Delta r2 = 0.57$, $\Delta r3 = 0.62$ (angstroms). The same is the case for the second excited state, a doublet E state. The vertical and adiabatic (best non-converged geometry) are 1.75 and 1.71 eV, and 1.83 and 1.83 eV, for the first and second excited states, respectively.

4. IV. b. 3 Excited electronic states of the C_s rhombus structure

We calculated the lowest-lying excited states for the C_s geometry. The first excited state has A' symmetry. There are changes in geometry from the ground state to the excited state. The calculated transition energy (for the best non-converged geometry of the excited state) is 1.95 eV.

4. IV. c. Franck-Condon simulations

A Franck-Condon simulation of the spectrum was calculated for the lowest excited state of the C_{2v} geometry and is presented in Figure 4–5. Since the origin of the band was not discernible in the spectra, the frequency units are offset. The Franck-Condon simulation for the V structure shows a sequence of four vibrations, which are spread over a region of $\sim 1000 \text{ cm}^{-1}$. Since the electronic excited state has a B_1

symmetry it is possible that a B_1 vibration at 33.3 cm^{-1} lights up. This band would not show in this simulation. The simulation agrees qualitatively with the part of the spectrum above $13\,900\text{ cm}^{-1}$, however, it does not show the band density present in the spectrum.

4. V. Discussion

The spectrum at 720 nm differs remarkably from the 650 nm band. As opposed to the dominating origin indicating a vertical transition, a broad congested band with several overlapping peaks characterizes the 720 nm spectrum. The congestion in the spectra is likely to arise from a large change in geometry from the ground state to the excited state. Calculations show that both the V-shaped C_{2v} and the distorted C_{3v} geometries have geometry changes from the ground to the first excited state. Therefore both structures are consistent with the spectra.

The C_{3v} distorted trigonal bipyramid is the most stable of the three structures. It is lower in energy than the C_{2v} structure by 0.352 eV and than the C_s structure by 0.573 eV. According to excitation energies the C_{3v} structure is also in best agreement with the data. The transitions to first and excited states are 1.71 and 1.83 eV, respectively. The experimental value is near 1.70 eV. The C_{2v} structure is also a possible candidate. The lowest B_1 excited state has higher transition energy, 2.18 eV. But the state that converges to linear drops significantly, to 0.86 eV above the ground state C_{2v} . The rhombus geometry has a transition energy to the first excited state of 1.95 eV, which is acceptable within the expected accuracy of the CIS method.

The spectra do not possess well characterized progressions, however, the data suggests some frequencies that are repeated often in the spectrum (below $13\,900\text{ cm}^{-1}$): 24, 50, 63, 90 and 105 cm^{-1} . Without well-defined progressions one cannot ascertain

these are vibrational progressions. If they are, the C_{2v} structure is the only one in agreement with the low frequency modes. Both C_{3v} and C_s symmetry structures have the lowest vibrational frequency at $\sim 115 \text{ cm}^{-1}$. We did not calculate vibrational frequencies of the excited states, but the changes in geometry predicted should not lead to significant changes in the vibrational frequencies. One other possibility is that the Jahn-Teller distortion, which should result in a splitting of the degenerate E symmetry excited states can lead to small vibrational splittings. This possibility was not addressed in the calculations we performed. However, such small vibrational frequency splittings are known to occur in Jahn-Teller distorted excited states.¹⁰

Another possibility is that the markedly different regions of the spectrum (above and below $13\,900 \text{ cm}^{-1}$) may be due to different isomers / excited states. The bands below $13\,900 \text{ cm}^{-1}$ show an increase in intensity with frequency. They also possess a fixed shift of $\sim 4.5 \text{ cm}^{-1}$ between the bands from the 185 and 187 isomers. The spectrum above $13\,900 \text{ cm}^{-1}$ is much more congested, and such patterns are either unresolvable or not present. It is therefore conceivable that several bands are present in this region, including the ${}^2B_1 \leftarrow X {}^2A_1$ transition of the ring geometry.

There are several directions in which to further pursue this problem. Higher level calculations of all possible geometries and excited states, such as in the work of Balasubramanian and coworkers⁸ may lead to a better picture of the excited states of Ca_2Cl_3 . The spectra acquired were also not of sufficient resolution to obtain rotational levels or even contours. The different geometries have distinct rotational coefficients, such that an analysis of the rotational contours of each band may allow a direct assignment, and indicate if more than one isomer is present in the beam. The

preliminary spectra presented in this work should be rescanned with more care for laser power saturation.

4. VI. Conclusion

We have observed a new band of the Ca_2Cl_3 radical cluster around 720 nm. The spectrum is congested and may be due to more than one isomer. HF and CIS calculations have been performed to aid in understanding the spectra. Three geometries were considered in the calculations. While we were unable to assign the data to one of the isomers, we were able to qualitatively compare the spectra with the calculated transitions. Of the three geometries calculated, a stable minimum of the C_{3v} geometry is the lowest energy isomer, only 42.9 kJ/mol above the C_{2v} ring minimum.

4. VII References

1. U. Landman, D. Scharf, and J. Jortner, *Phys. Rev. Lett.* **54** 1860 (1985).
2. G. Rajagopal, R. N. Barnett, A. Nitzan, U. Landman, E. C. Honea, P. Labastie, M. L. Homer, R. L. Whetten, *Phys. Rev. Lett.* **64** 2933 (1990).
3. G. Durand, J. Giraud-Giraud, D. Maynau, F. Spiegelmann, F. Calvo, *J. Chem. Phys.* **110** 7871 (1999).
4. M. Hartmann, J. Pittner, V. Bonacic-Koutecky, *J. Chem. Phys.* **114** 2106 (2001).
5. M. Hartmann, J. Pittner, V. Bonacic-Koutecky, *J. Chem. Phys.* **114** 2123 (2001).
6. J. D. Lobo, A. Deev, C-K. Wong, J. M. Spotts, and M. Okumura, *J. Chem. Phys.* **114** 8913 (2001).
7. V. Glezakou, private communication.
- ⁸ P. Y. Feng, D. Dai, and K. Balasubramanian, *J. Phys. Chem.* **104** 422 (2000).
9. M. J. Frisch, G. W. Trucks, H. B. Schlegel, G. E. Scuseria, M. A. Robb, J. R. Cheeseman, V. G. Zakrzewski, J. A. Montgomery, Jr., R. E. Stratmann, J. C. Burant, S. Dapprich, J. M. Millam, A. D. Daniels, K. N. Kudin, M. C. Strain, O. Farkas, J. Tomasi, V. Barone, M. Cossi, R. Cammi, B. Mennucci, C. Pomelli, C. Adamo, S. Clifford, J. Ochterski, G. A. Petersson, P. Y. Ayala, Q. Cui, K. Morokuma, D. K. Malick, A. D. Rabuck, K. Raghavachari, J. B. Foresman, J. Cioslowski, J. V. Ortiz, B. B. Stefanov, G. Liu, A. Liashenko, P. Piskorz, I. Komaromi, R. Gomperts, R. L. Martin, D. J. Fox, T. Keith, M. A. Al-Laham, C. Y. Peng, A. Nanayakkara, C. Gonzalez, M. Challacombe, P. M. W. Gill, B. Johnson, W. Chen, M. W. Wong, J. L. Andres, C. Gonzalez, M. Head-Gordon, E. S. Replogle, and J. A. Pople, *Gaussian 98*, Revision A.5.
- ¹⁰ T. A. Barckholtz and T. A. Miller, *J. Phys. Chem.* **103** 2321 (1999).

4. VII. Figure captions

Figure 4–1 Structures of Ca_2Cl_3 predicted by HF/[6-311G+(3df)] theory calculations. (a) C_{2v} planar V, (b) C_{3v} distorted trigonal bipyramid, and (c) C_s rhombus.

Figure 4–2 Electronic 1+1' REMPI spectrum of $\text{Ca}_2^{35}\text{Cl}_3$ ($m/e = 185$ amu).

Figure 4–3 Electronic 1+1' REMPI spectrum of $\text{Ca}_2^{35}\text{Cl}_2^{37}\text{Cl}$ ($m/e = 187$ amu).

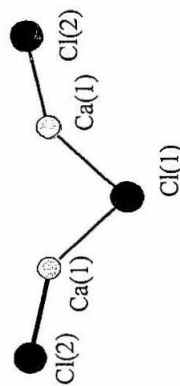
Figure 4–4 Comparison of a portion of the spectra of $\text{Ca}_2^{35}\text{Cl}_3$ (185 amu, solid line) and $\text{Ca}_2^{35}\text{Cl}_2^{37}\text{Cl}$ (187 amu, dotted line).

Figure 4–5 Franck-Condon simulation of the transition to the first excited state of the V-shaped C_{2v} symmetry isomer.

Isomers of Ca_2Cl_3

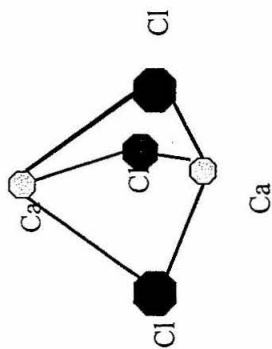
(HF/6-311+G(3df))

C_{2v} planar V-shape



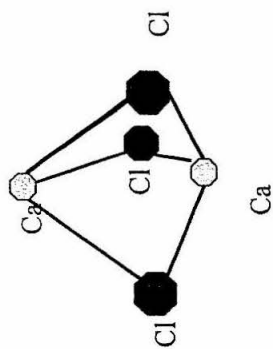
33.8 kJ/mol

C_{3v} distorted bipyramid



0 kJ/mol

C_s rhombus



55.1 kJ/mol

Figure 4-1

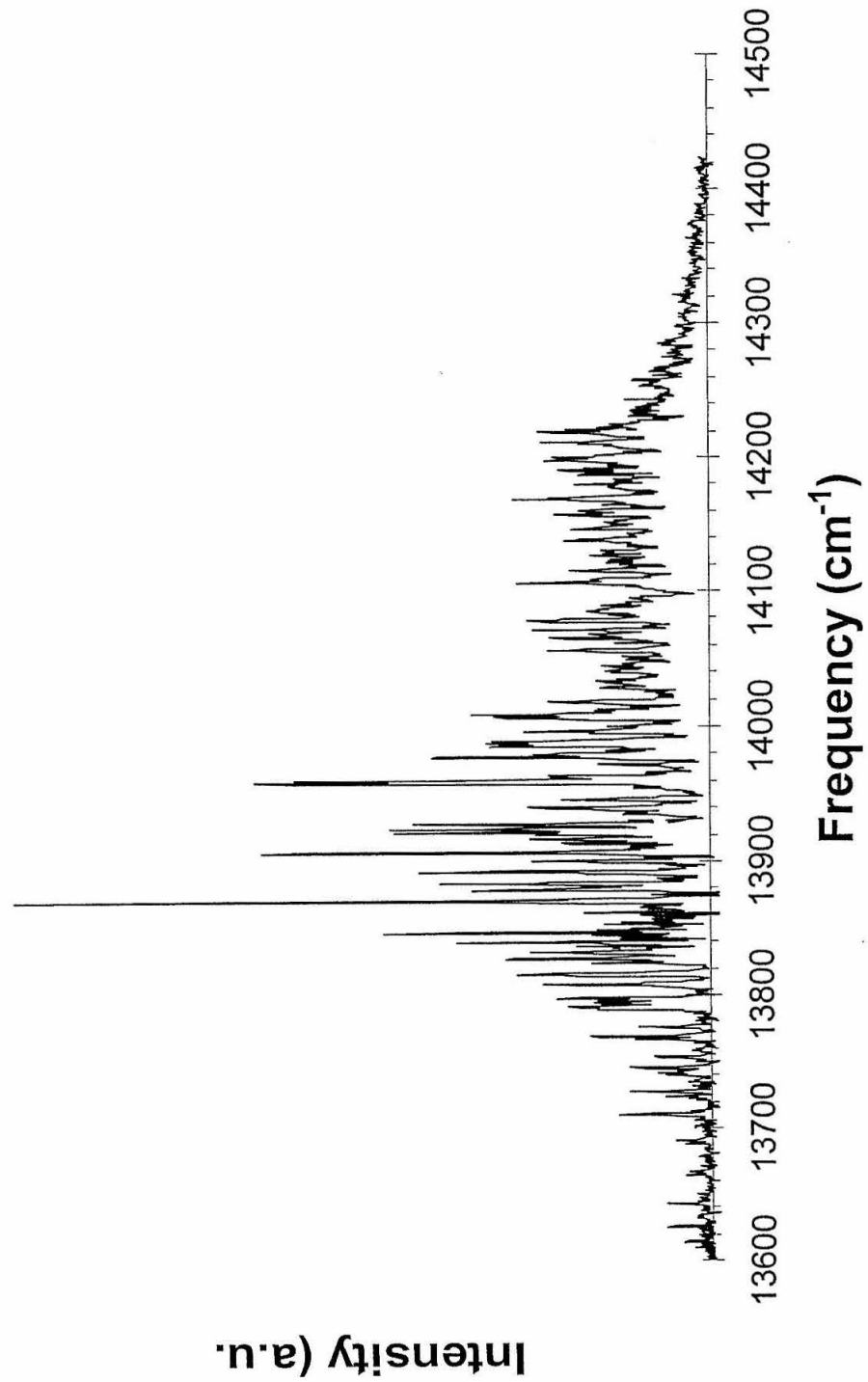


Figure 4-2

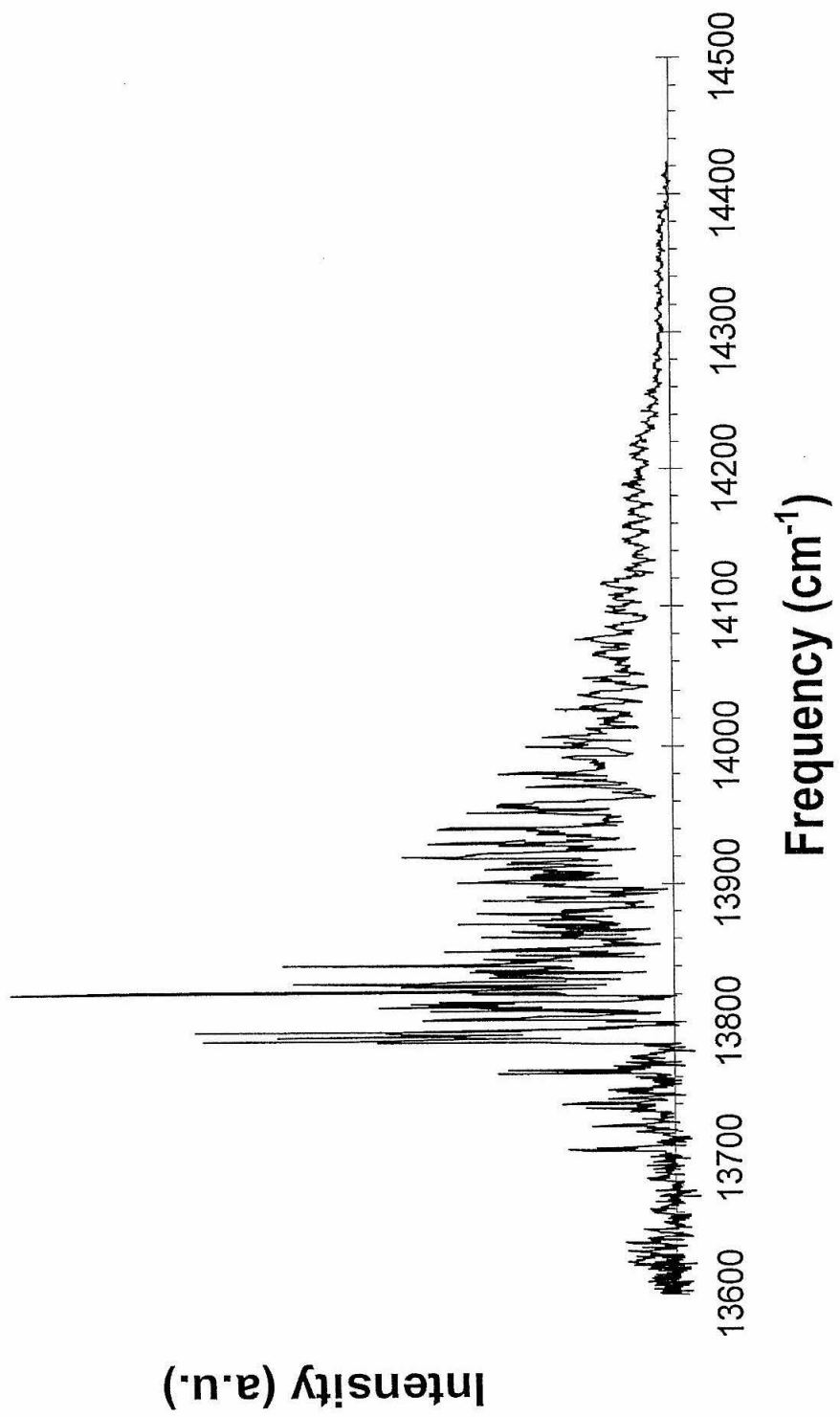


Figure 4-3

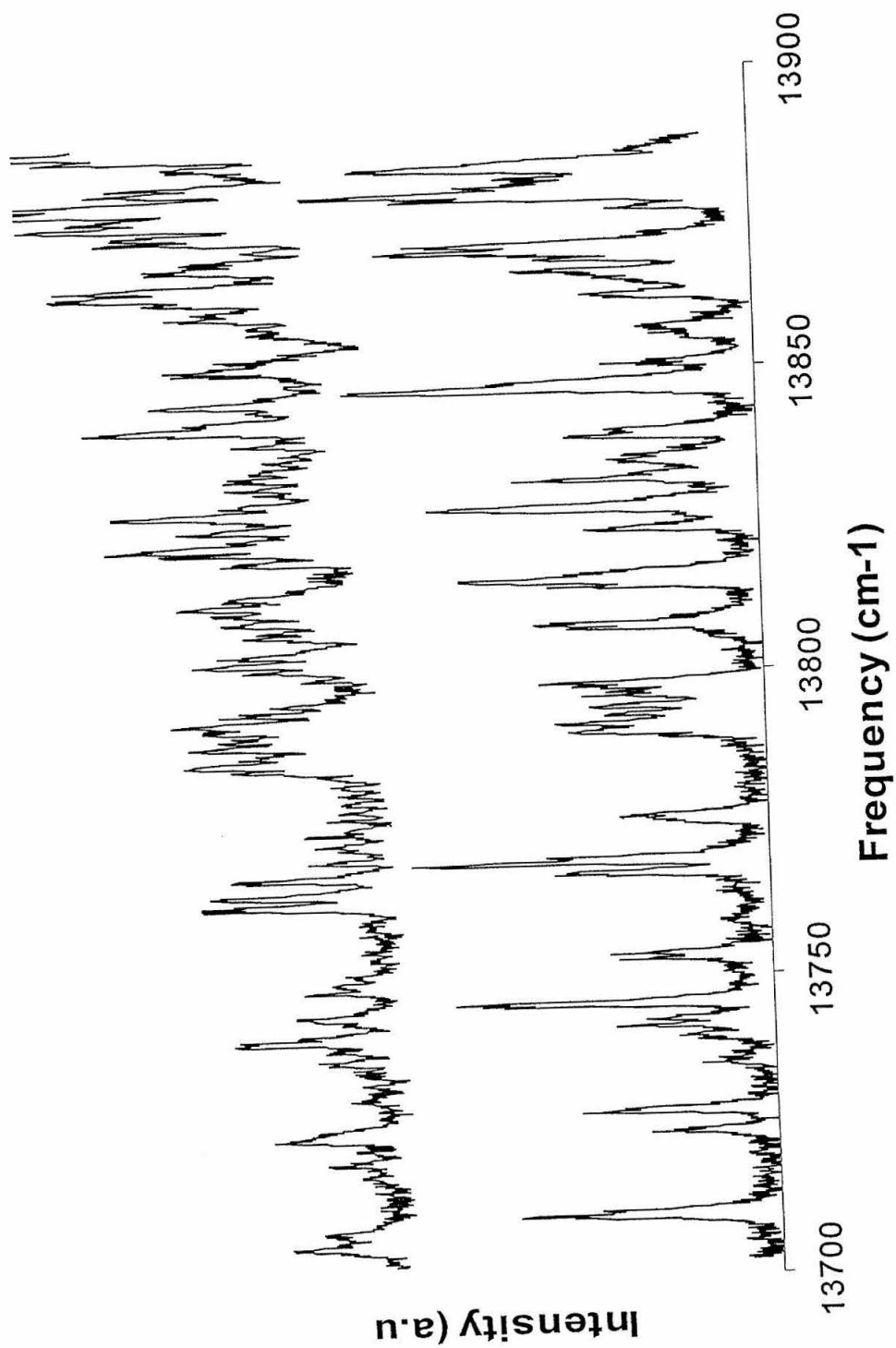


Figure 4-4

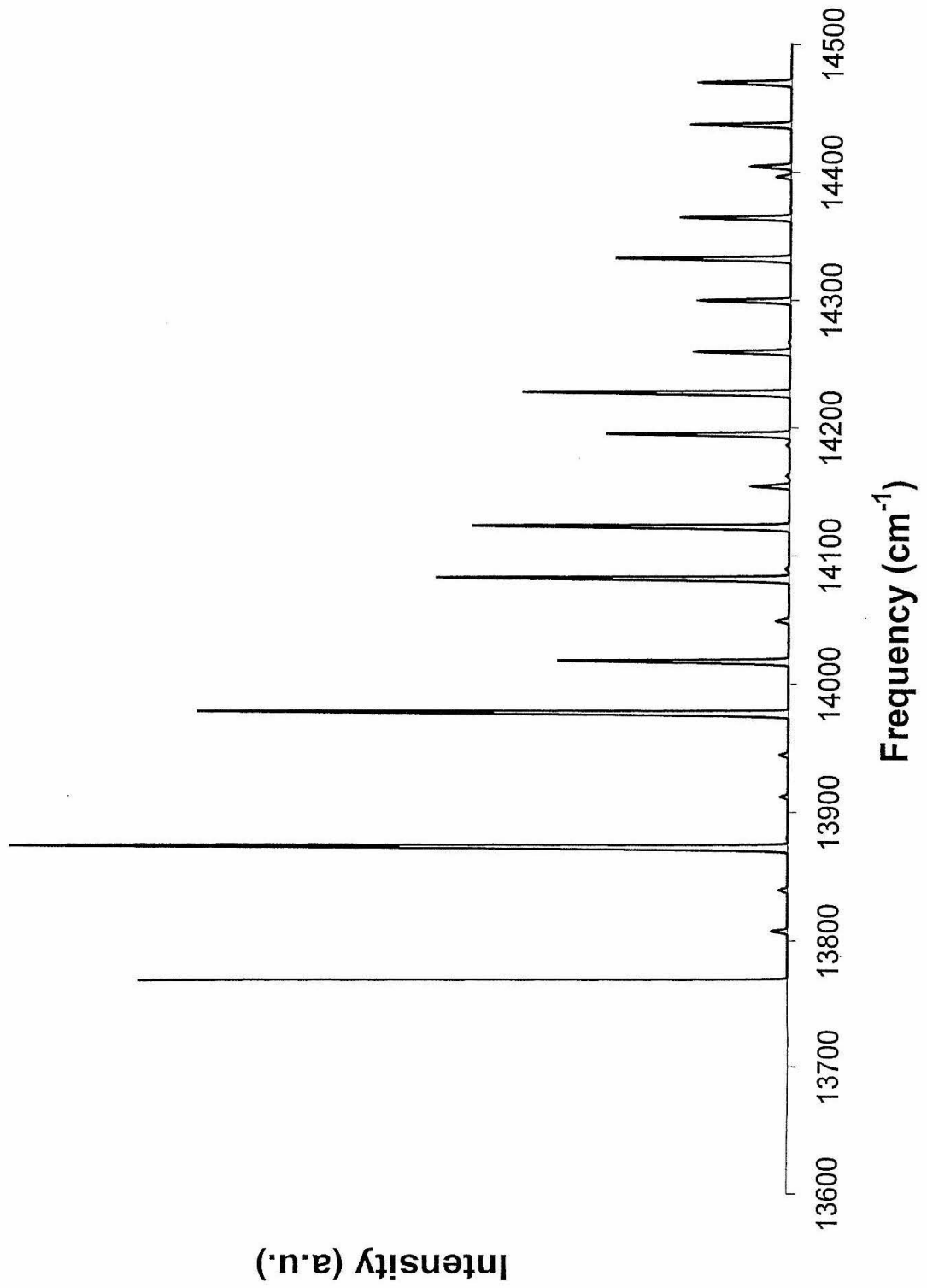


Figure 4-5

TABLE 4-I Calculated geometries, energies, and vibrational frequencies of the ground and lowest-lying excited electronic states of the V-shape C_{2v} planar $Ca_2^{35}Cl_3$ structure (and linear). From HF/6-311+G(3df) (ground state) and CIS/6-311+G(3df) (excited states) calculations.

		X^2A_1	2B_1	$^2\Sigma_u$	Expt.
<u>Coordinates</u>					
geometry		V-shaped	V-shaped	Linear	
r_1 (Å)	Ca(1)-Cl(1)	2.498	2.484	2.496	
r_2 (Å)	Ca(1)-Cl(2)	2.703	2.680	2.664	
r_2 (Å)	Ca(1)-Ca(2)	3.800	3.969	2.663	
α (deg.)	Ca(1)-Cl(2)-Ca(2)	89.33	95.5	180	
β (deg.)	Cl(2)-Ca(1)-Cl(2)	140.57	145.7	180	
<u>Electrostatic parameters</u>					
μ (Debye)		0.0923	1.1135	0	
α^b		424.86	649.31	324.50	
<u>Energetics (adiabatic states)</u>					
E_{el} (hartree)	HF/6-311+G(3df)	-2 732.36371			
ΔE_0 (eV)	CIS/6-311+G(3df)	0.00	2.181	0.856	1.698
<u>Vibrational frequencies</u>					
ν_1 (cm $^{-1}$)	B_1	30.6	-	-	
ν_2 (cm $^{-1}$)	A_1	36.6	27.4	-	
ν_3 (cm $^{-1}$)	A_2	50.5	33.3 (B_1)	-	
ν_4 (cm $^{-1}$)	B_2	61.5	43.6	-	
ν_5 (cm $^{-1}$)	A_1	105.5	78.5	7.35 ($I\Gamma_u$)	
ν_6 (cm $^{-1}$)	B_2	205.2	211.5	126.6 (Σ_g)	
ν_7 (cm $^{-1}$)	A_1	246.0	245.6	295.3 (Σ_u)	
ν_8 (cm $^{-1}$)	B_2	365.1	374.8	381.5 (Σ_g)	
ν_9 (cm $^{-1}$)	A_1	386.0	390.5	385.1 (Σ_u)	

^a Observed optical transition

^b Trace of polarizability tensor ($\alpha_{xx} + \alpha_{yy} + \alpha_{zz}$)

TABLE 4-I

TABLE 4-II Calculated geometries, energies, and vibrational frequencies of the ground and lowest-lying states of the distorted trigonal bipyramid C_{3v} $Ca_2^{35}Cl_3$ structure. From HF/6-311+G(3df) (ground state) and CIS/6-311+G(3df) (excited states) calculations.

		X^2A_1	$^2A_1^c$	$^2E^c$	Expt. ^a
<u>Coordinates</u>					
geometry		C_{3v}	C_{3v}	C_{3v}	
r_1 (Å)	Ca(1)-Cl(1)	2.598	2.684	2.683	
r_2 (Å)	Ca(2)-Cl(1)	2.901	2.844	2.845	
r_3 (Å)	Ca(1)-Ca(2)	3.458	3.396	3.397	
α (deg.)	Ca(1)-Cl(2)-Ca(2)	77.68	76.94		
β (deg.)	Cl(1)-Ca(1)-Cl(2)	78.96	80.70		
γ (deg.)	Cl(1)-Ca(2)-Cl(2)	90.48	89.92		
<u>Electrostatic parameters</u>					
μ (Debye)		9.3029			
α^b					
Spin density	Ca(1)	0.158			
	Ca(2)	0.847			
<u>Energetics (adiabatic states)</u>					
E_{el} (hartree)	HF/6-311+G(3df)	-2 732.37659			
ΔE_0 (eV)	CIS/6-311+G(3df)	0.00	1.7119	1.8312	1.698
ΔE_0 vertical	CIS/6-311+G(3df)	0.00	1.7521	1.8318	1.698
<u>Vibrational frequencies</u>					
ν_1 (cm ⁻¹)	E	113.8			
ν_2 (cm ⁻¹)	E	113.8			
ν_3 (cm ⁻¹)	E	123.6			
ν_4 (cm ⁻¹)	E	123.6			
ν_5 (cm ⁻¹)	A_1	178.8			
ν_6 (cm ⁻¹)	A_1	196.7			
ν_7 (cm ⁻¹)	E	293.1			
ν_8 (cm ⁻¹)	E	293.1			
ν_9 (cm ⁻¹)	A_1	318.5			

^a Observed optical transition

^b Trace of polarizability tensor ($\alpha_{xx} + \alpha_{yy} + \alpha_{zz}$)

^c Best non-converged geometry

TABLE 4–III Calculated geometries, energies, and vibrational frequencies of the rhombus C_s symmetry $\text{Ca}_2^{35}\text{Cl}_3$ structure. From HF/6-311+G(3df) (ground state) and CIS/6-311+G(3df) (excited states) calculations.

		X^2A'	$^2A'^c$	Expt. ^a
<u>Coordinates</u>				
Geometry		C_s	C_s	
r_1 (Å)	Ca(1)-Cl(1)	2.919	2.804	
r_2 (Å)	Ca(1)-Cl(2,3)	2.922	2.789	
r_3 (Å)	Ca(2)-Ca(1)	2.603	2.752	
r_3 (Å)	Ca(2)-Ca(2,3)	2.603	2.731	
r_4 (Å)	Ca(1)-Ca(2)	3.554	3.560	
α (deg.)	Cl(1)-Ca(1)-Cl(2,3)	77.46	81.69	
β (deg.)	Cl(2)-Ca(1)-Cl(3)	77.44	82.62	
γ (deg.)	Ca(1)-Cl(1)-Ca(2)	79.62	80.31	
δ (deg.)	Ca(1)-Cl(2,3)-Ca(2)	79.56	79.68	
<u>Electrostatic parameters</u>				
μ (Debye)		9.2410		
α^b		487.567		
Spin density	Ca(1)	0.107		
	Ca(2)	0.875		
<u>Energetics (adiabatic states)</u>				
E_{el} (hartree)	HF/6-311+G(3df)	-2732.35559		
ΔE_0 (eV)	CIS/6-311+G(3df)	0.00	1.9493	1.698
ΔE_0 vertical	CIS/6-311+G(3df)	0.00	1.9978	1.698
<u>Vibrational frequencies</u>				
ν_1 (cm^{-1})	A''	115.6		
ν_2 (cm^{-1})	A'	116.3		
ν_3 (cm^{-1})	A''	120.0		
ν_4 (cm^{-1})	A'	120.1		
ν_5 (cm^{-1})	A'	176.7		
ν_6 (cm^{-1})	A'	188.8		
ν_7 (cm^{-1})	A''	291.8		
ν_8 (cm^{-1})	A''	291.8		
ν_9 (cm^{-1})	A'	321.5		

^a Observed optical transition

^b Trace of polarizability tensor ($\alpha_{xx} + \alpha_{yy} + \alpha_{zz}$)

^c Best non-converged geometry

TABLE 4–III

Appendix A

Design of Second Generation Charged Liquid Helium Droplet Source

A.I. Summary

After pursuing the experiments that lead to chapter 2 of this work, we focused on building a charged helium droplet source that overcame difficulties in the operation of the first source. The new source was designed with the gained experience of having operated and reassembled the first source several times. Most of the improvements aimed at facilitating the assembly of the source. The change to a vertical axis was driven by the need to make the source compatible with most liquid helium cryostats.

Here we present the drawings of the new source, together with a brief discussion of the principle design parameters, source details, and advantages of the new source.

A. II. New source design

Modular assembly

The new design has the advantage of being modular and therefore simple to assemble. By releasing the Source Cover (Figure A–4), the insulating Macor piece (Figure A–5) can be removed, therefore simplifying the process of changing the high voltage needle. The replacement needle, which can be etched in place or beforehand, can be inserted through the glass nozzle, and then fixed in place by the two horizontal screws which transverse the Macor and copper clip parts (Figure A–1). The backside of the needle is then clipped and the source can be fixed back in place. The copper clip matches the 5 kV feed through pin ensuring good electrical contact.

Substitution of the glass nozzle is also straightforward. The Source Cover being removed can be separated from the Macor piece by releasing four screws. The low temperature epoxy can be removed from the glass–invar junction by heating, without damage to other parts of the assembly.

A.III. Figure captions

Figure A-1 Assembly of charged liquid helium droplet source. Components of assembly are shown by arrows.

Figure A-2 Assembly of charged liquid helium droplet source with dimensions.

Figure A-3 Drawing of the source body.

Figure A-4 Drawing of the source cover.

Figure A-5 Drawing of the macor piece.

Figure A-6 Drawing of the repeller piece.

Figure A-7 Drawing of the flange piece.

Figure A-8 Drawing of the base piece (top view).

Figure A-9 Drawing of the base piece (3D view).

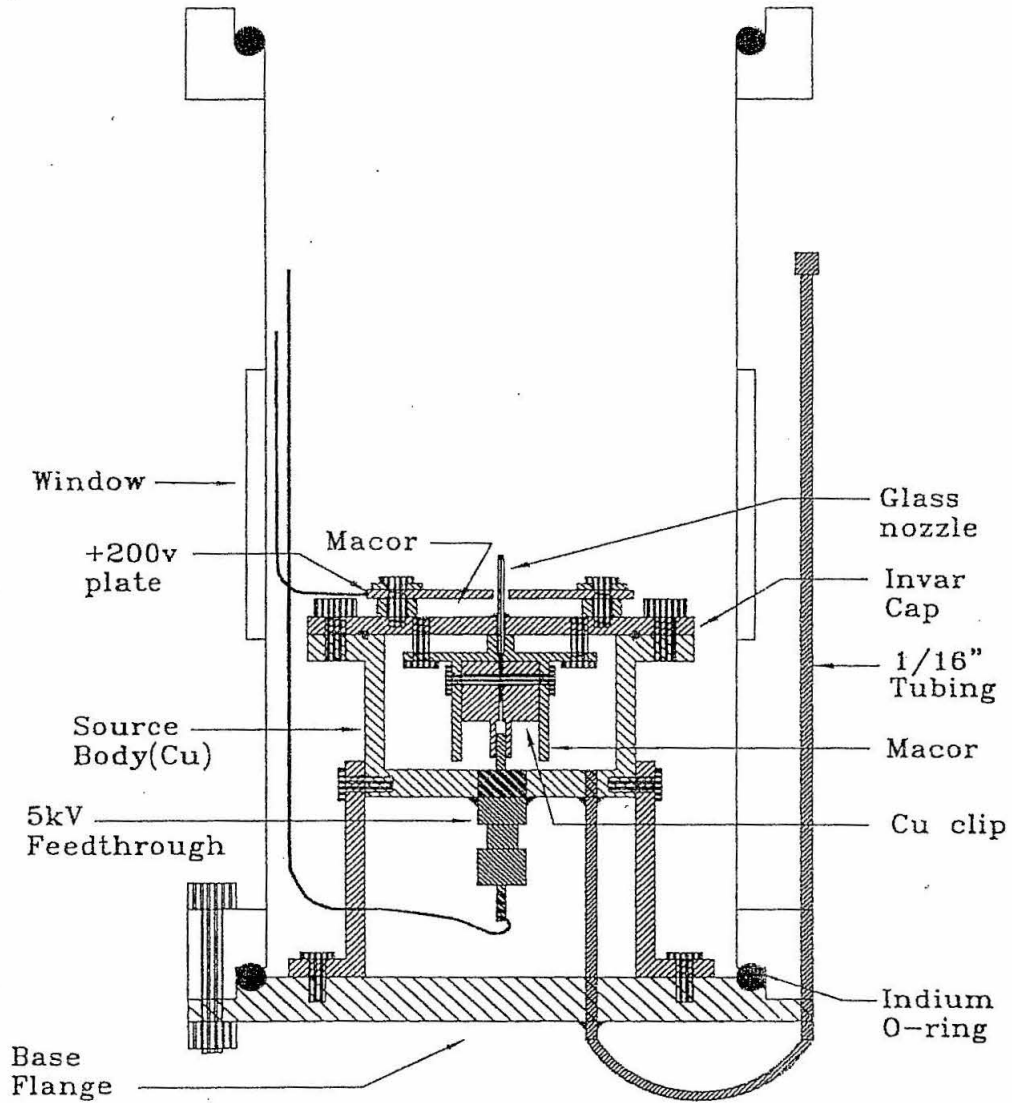


Figure A-1

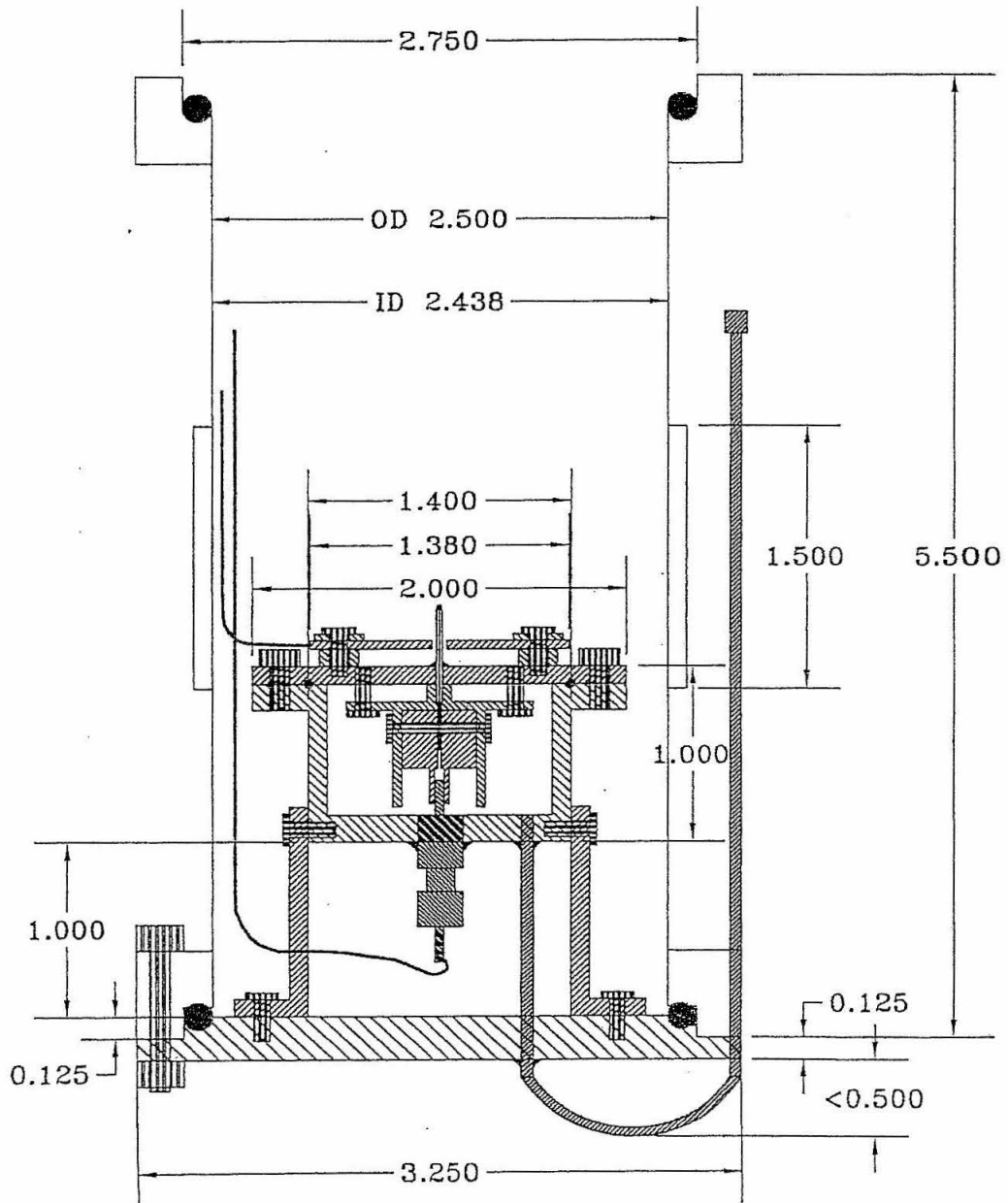
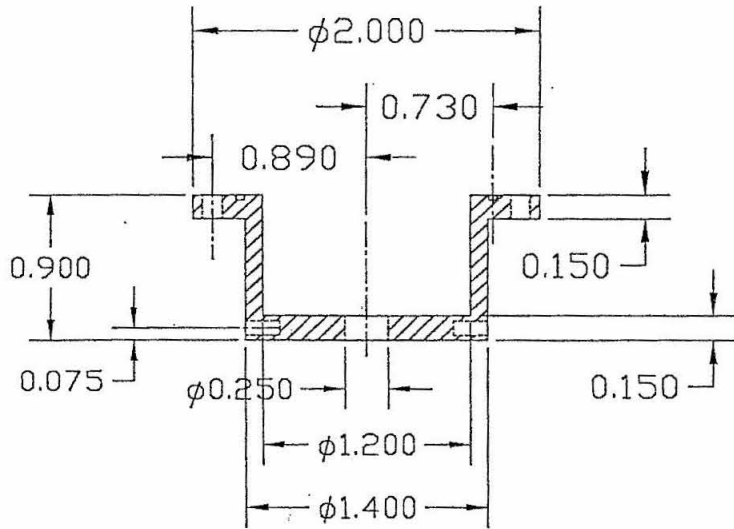
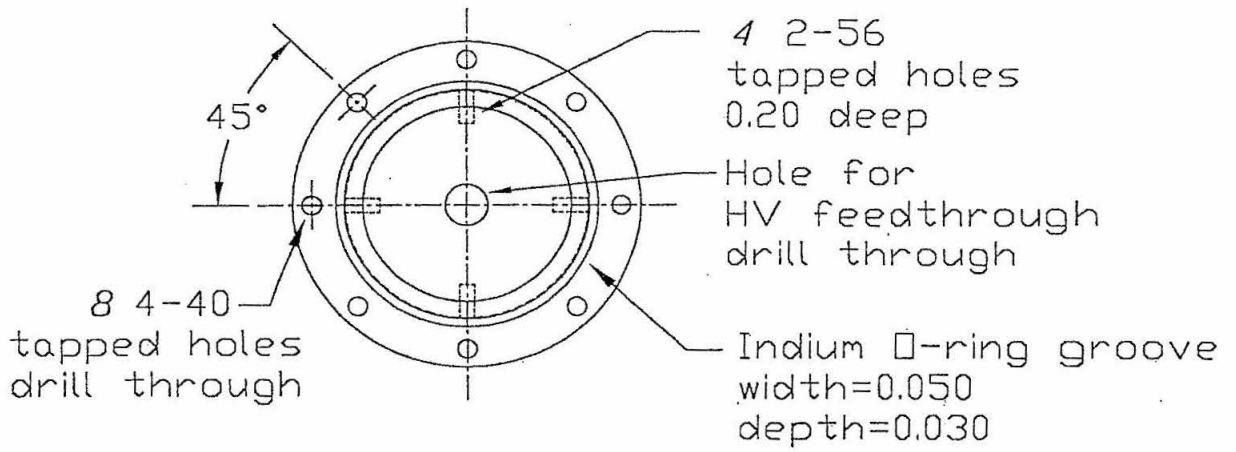
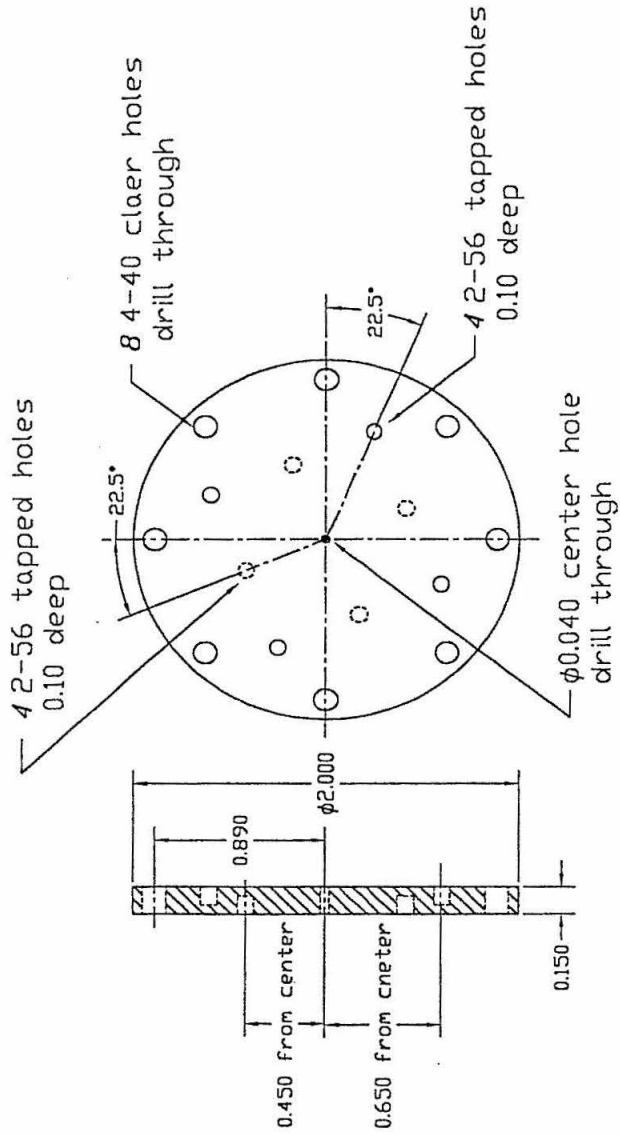


Figure A-2



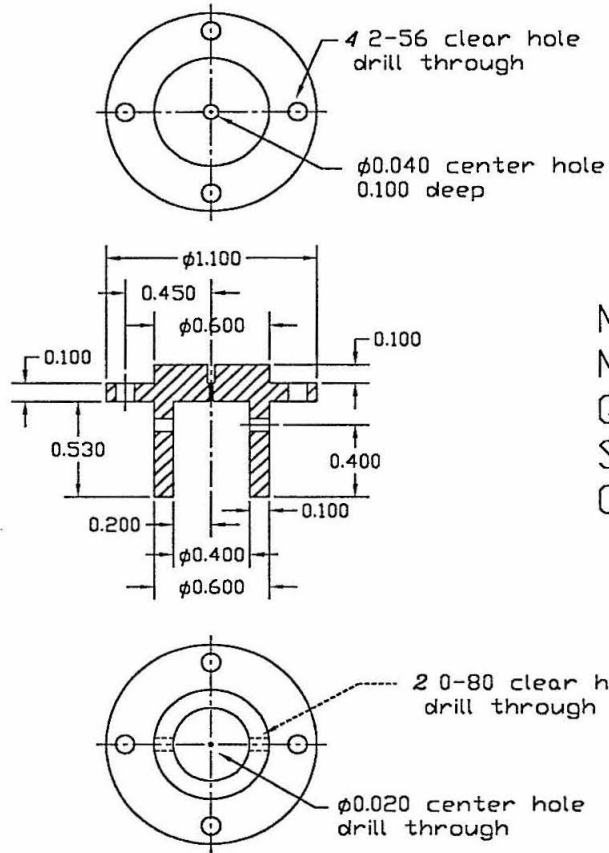
Source Body
 Material: □FHC
 Quantity: 1
 Scale 1:1
 Contact

Figure A-3



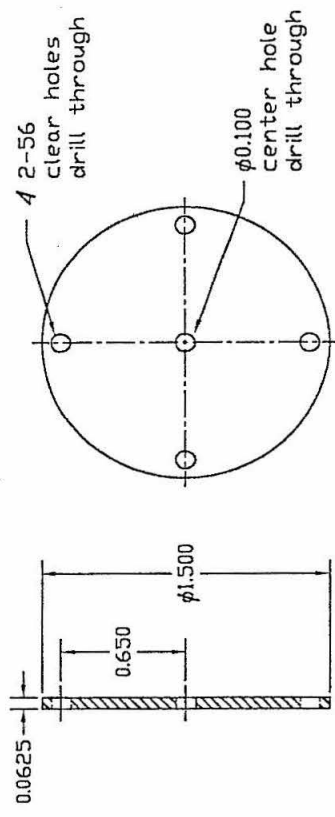
Source Cover
Material: Invar
Quantity: 1
Scale 1:1
Contact

Figure A-4



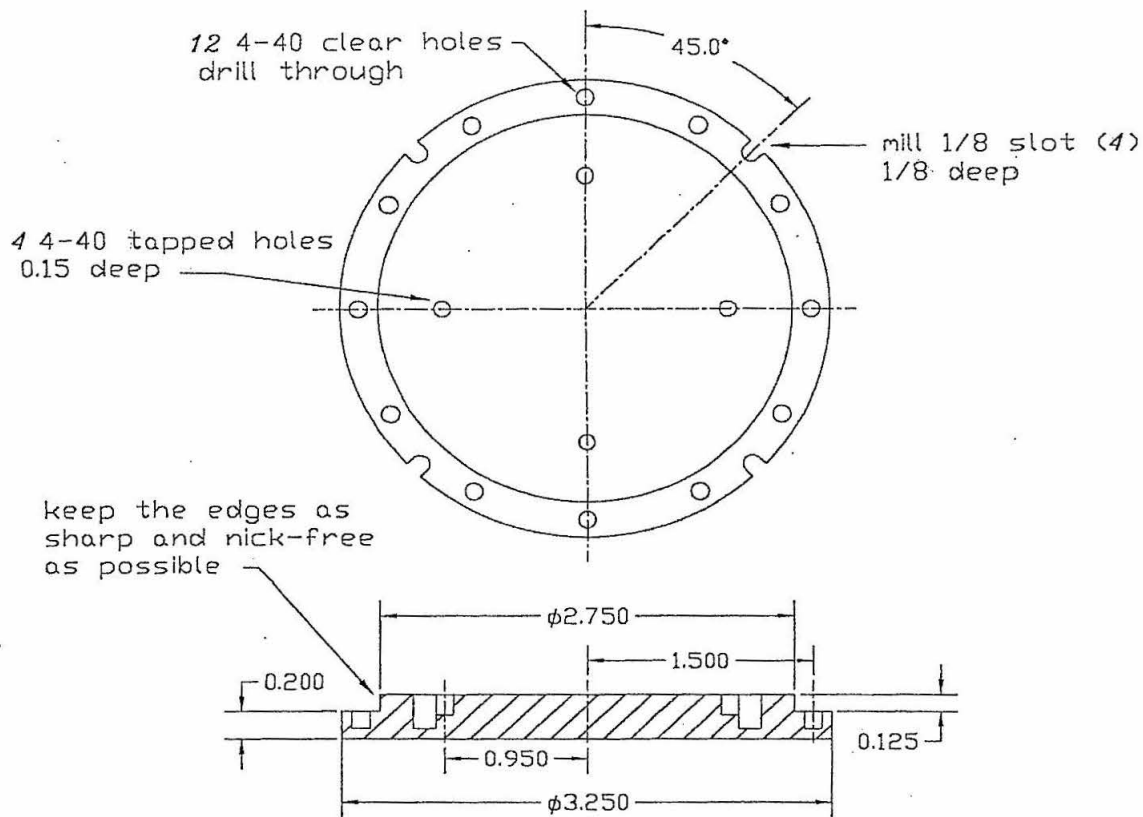
Macor
 Material: Macor
 Quantity: 1
 Scale 1:1
 Contact

Figure A-5



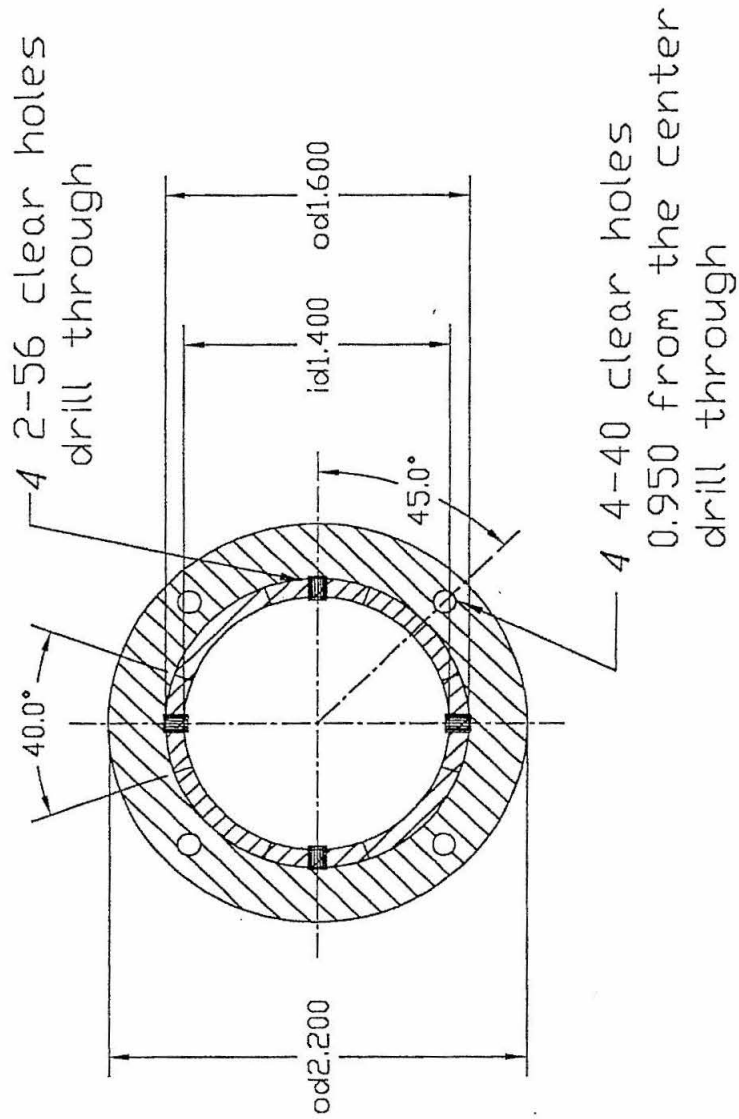
Repeller
Material: \square FHC
Quantity: 1
Scale 1:1
Contact

Figure A-6



Flange
 Material: \square FHC
 Quantity: 1
 Scale 1:1
 Contact:

Figure A-7



Base (top view)
 Material: \square FHC
 Quantity: 1
 Scale 1:1
 Contact

Figure A-8

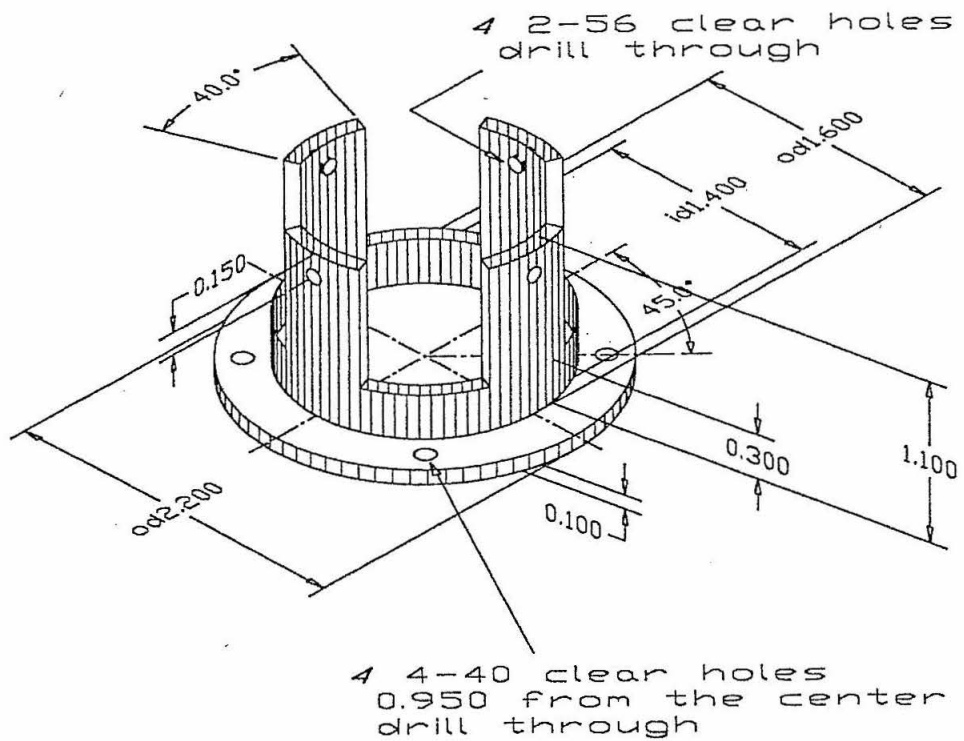


Figure A-9

Appendix B

Generation of 118 nm Photons

B. I. Summary

It is often convenient in laser - mass spectrometry experiments to have coherent vacuum-ultraviolet (VUV) photons, such that single photon ionization is possible. The cross-sections for single photon ionization are many orders of magnitude higher than nonresonant multiphoton ionization. Thus, higher ion intensities are attainable. In addition, since lower laser intensities are required, fragmentation is less likely than in multiphoton ionization.

Frequency up-conversion techniques for generating VUV photons are scattered throughout the laser physics literature. Most methods explore nonlinear optical effects.^{1,2} Lockyer and Vickerman³ reported third harmonic generation (THG) of 118 nm VUV Light (10.51 eV) using frequency tripled 355nm Nd:YAG laser pump source in xenon or xenon and argon cells. Lockyer and Vickerman reported optimized conditions for the generation of 118 nm photons. Starting from their empirical parameters, we have designed, built, and optimized a 118 nm laser source. Here we list the equipment and setup of the laser scheme used, some guiding parameters in the design, and the optimal pressure and laser power conditions we found by monitoring the ionization of benzene in our ion time-of-flight setup.

B. II. Experimental setup

The THG cell consisted of a cylindrical 150 cm long and 3.5 cm internal diameter cell. The ends of the cylinder were fitted with a 1 m focal length input CaF₂ lens, which focused the incoming 355 nm laser, and a 2 m focal length output MgF₂ lens. The focal lengths of the lenses were selected by fixing the beam waist of the 118 nm beam at the intersection with the molecular beam, while observing the limiting threshold for breakdown in Xe, the threshold for damage of the MgF₂ lens, and the de-focusing of the

355 nm light to avoid multiphoton ionization. The CaF_2 was mounted on a standard 2.75 Conflat flange. The MgF_2 was mounted on a custom made double sided flange, which also served to link the THG cell to the time-of-flight apparatus. The custom made flange consisted of a commercially available double-sided 2.75 Conflat flange, (MDC REF # FD-275000-1) modified to accommodate a 1.5 inch lens and with four 4-40 tapped holes. The lens was held in place by an o-ring, which in turn was fixed by a machined stainless steel plate with four 4-40 screws. See Figures B-1 and B-2.

At the center point of the cell there were three standard 2.75 conflat flange ports. One port held a leak valve through which the xenon gas was allowed into the cell. The second port held a window. The third port was connected to a standard four-way 2.75 conflat cross. The cross connected the cell to an ion gauge for low pressure measurement ($P < 10^{-4}$ Torr), a 100 Torr Baratron for operational pressure measurement ($P \cong 0.1\text{-}100$ Torr), and a turbomolecular pump (Balzers TPU 050) for efficiently pumping out the cell. The turbomolecular pump was backed by a mechanical pump (02A Leybold-Heraus). See Table B-1 for a list of the equipment.

The 355 nm light was obtained by third harmonic generation from a 1064 nm Nd:YAG pump laser (Continuum NY61-20). Approximately 30 mJ of 355 nm were focused into the xenon cell. The optimal xenon pressure was also considered in the design of the cell. It was estimated from the empirical data of Lockyer and Vickerman (See Calculation B-1).

The cell was assembled perpendicularly to our time-of-flight apparatus, intersecting an expanded argon/benzene molecular beam at the center of the time of flight extraction region. The time-of-flight is described in Chapter 3 of this work, and elsewhere.⁴ The cell alignment was performed by centering a HeNe laser through the tof flight extraction region, the MgF_2 lens and the CaF_2 lens.

B. III. Experiment

Benzene at room temperature was entrained in argon carrier gas and expanded into vacuum. The base pressure of the chamber was 5.6×10^{-7} Torr, and increased to 2.6×10^{-5} Torr while the source was operating. The opening of the valve and the laser firing were timed with a delay generator. (SRS DG535).

The benzene was ionized by the VUV photons at the extraction region of the time-of-flight. The ions were then detected at the microchannel plate detector. The signal was amplified and recorded on an oscilloscope (Tektronics model TDS320). An acquired scan of benzene ion signal from the oscilloscope is shown in Figure B-3. The data was acquired with a -1.58 kV MCP voltage and a 15 X amplifier. The signal disappeared once the xenon cell was emptied, and reappeared when refilled. Once benzene ion signal was observed, the laser power was optimized. The benzene ion signal increased with the laser power, but reached a plateau at 30 mJ.

The cell pressure was optimized with the benzene ion signal. Optimal signal was obtained at a pressure of ≈ 450 mTorr. The dependence of the ion signal versus xenon pressure was measured and is plotted in Figure B-4.

B. IV. References

1. N. B. Delone and V. P. Krainov, *Fundamentals of Nonlinear Optics of Atomic Gases*, Wiley, New York (1988).
2. A. L'Huillier, L. A. Lompre, G. Mainfray, and C. Manus. *Adv. At. Mol. Phys.* **24** 3315 (1991).
3. N. P. Lockyer, and J. C. Vickerman, *Laser Chem.* **17** 123 (1997).
4. J. M. Spotts, Ph. D. Thesis, California Institute of Technology (1999).

Estimate of pressure for Xenon cell (from: Vickerman et al. Laser Chem, 17,139, '97)

$$n1 := 1.4144 \quad \text{for CaF}_2 \text{ at } 355 \text{ nm} \quad \lambda1 := 3.55 \cdot 10^{-4}$$

$$f := 1000 \quad \text{mm} \quad \text{focal length}$$

$$n := 1 \quad (\text{in Xenon})$$

$$D := 5.5 \quad \text{mm} \quad (\text{diameter of beam waist at entrance})$$

$$K(n1) := \frac{1}{32} \cdot (n1 - 1)^{-2} \cdot \left(n1^2 - 2 \cdot n1 + \frac{2}{n1} \right) \quad \theta := \frac{1}{2} \cdot K(n1) \cdot \left(\frac{D}{f} \right)^3 + 1.22 \cdot \frac{\lambda1}{n \cdot D}$$

$$w_0 := f \cdot \theta \quad w_0 = 0.079 \quad \text{mm} \quad (\text{beam waist at focus point})$$

$$b := \frac{2 \cdot \pi \cdot w_0^2 \cdot n}{\lambda1 \cdot 10} \quad b = 10.977 \quad \text{cm} \quad (\text{confocal parameter})$$

$$\beta := 3.036 \cdot 10^{-17} \quad b \Delta k_{\text{opt}} := -13 \quad C_{\text{Xe}} := -6 \cdot 10^{-17}$$

$$P := \frac{b \Delta k_{\text{opt}} \cdot \beta}{C_{\text{Xe}} \cdot b} \quad P = 0.599 \quad \text{Torr}$$

Damage Threshold for optics: (355 beam size ~3mm at MgF₂)
(assume 10 ns pulse)

$$\text{MgF}_2 \quad \text{area} := 0.15^2 \cdot \pi \quad \text{area} = 0.071 \quad \text{cm}^2$$

$$\frac{10^8}{2} \cdot 10^{-8} \cdot 1000 \cdot \text{area} = 35.343 \quad \frac{\text{mJ}}{\text{pulse}}$$

$$\text{Threshold for breakdown in Xe:} \quad \text{area2} := 0.025^2 \cdot \pi \quad \text{area2} = 0.002 \quad \text{cm}^2$$

$$\frac{10^{11}}{2} \cdot 10^{-8} \cdot \text{area2} \cdot 1000 = 981.7477 \quad \frac{\text{mJ}}{\text{pulse}}$$

SiO₂

$$\frac{70}{2} \cdot \text{area} \cdot 1000 = 2.474 \cdot 10^3 \quad \frac{\text{mJ}}{\text{pulse}}$$

TABLE B-I List of equipment for assembly of THG xenon cell.

- 150 cm, 3.5 cm inner diameter 5-way cross cylindrical cell
- 15 cm lens holder
- modified double-sided conflat lens holder
- 4-way standard 2.75 conflat cross
- 1 m focal length CaF₂ lens
- 2 m focal length MgF₂ lens
- Xe 99.9999 purity gas
- Leak valve
- Ion gauge (Grainville-Phillips) and controller
- 100 Torr Baratron (MKS) and controller
- Balzers TPU50 turbomolecular pump
- Leybold-Heraeus 02A mechanical pump

B. V. Figure captions

Figure B-1 Drawing of modified blank double-sided flange.

Figure B-2 Drawing of internal flange for fixing MgF_2 lens.

Figure B-3 Benzene ion signal acquired from oscilloscope.

Figure B-4 Plot of benzene ion signal as a function of the xenon pressure in THG cell.

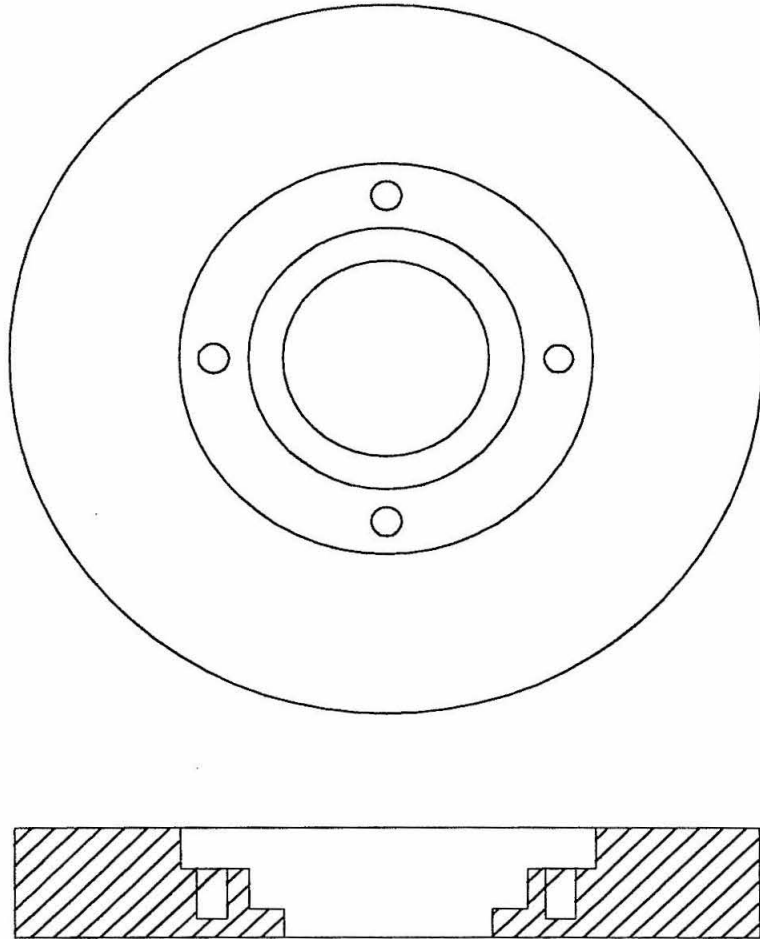


Figure B-1

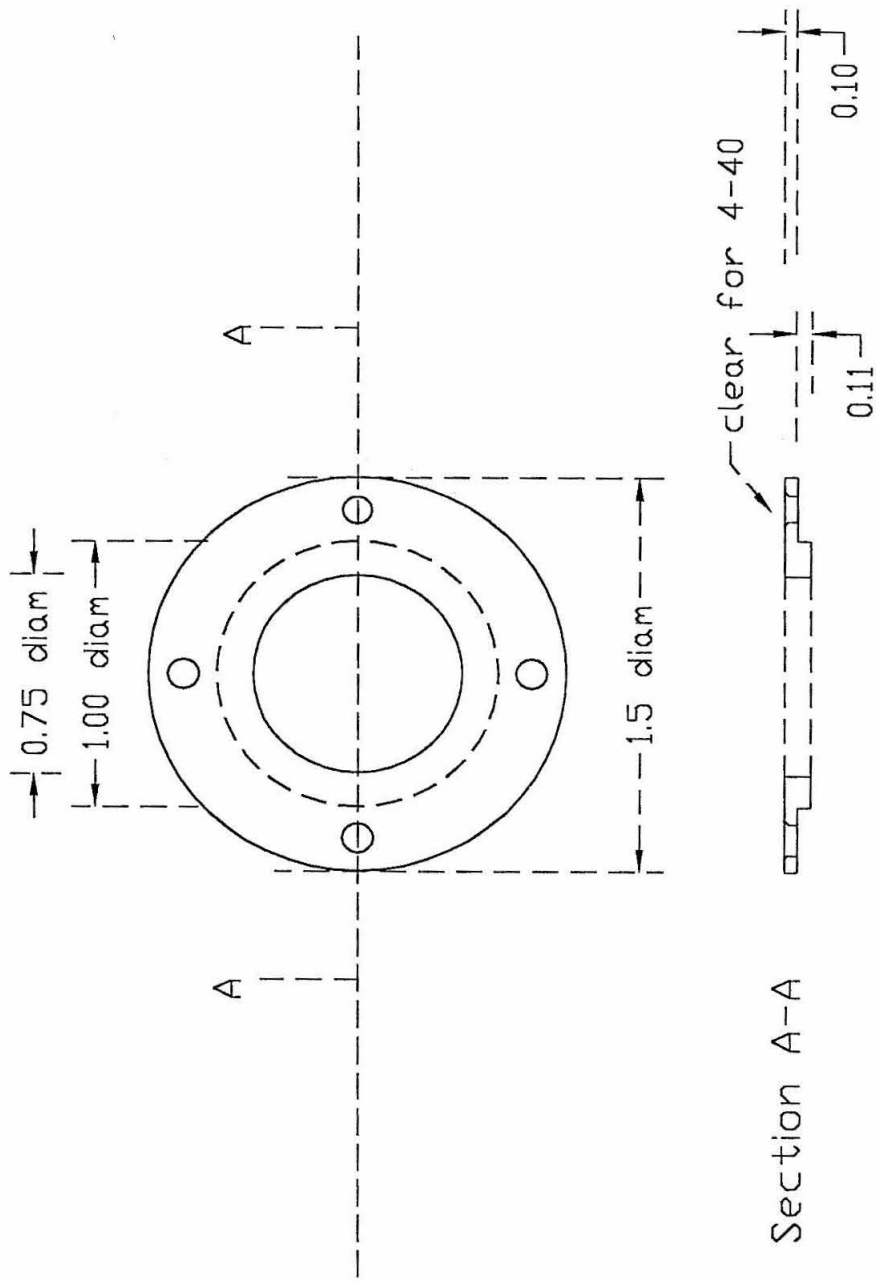


Figure B-2

Tek Stopped: 179 Acquisitions

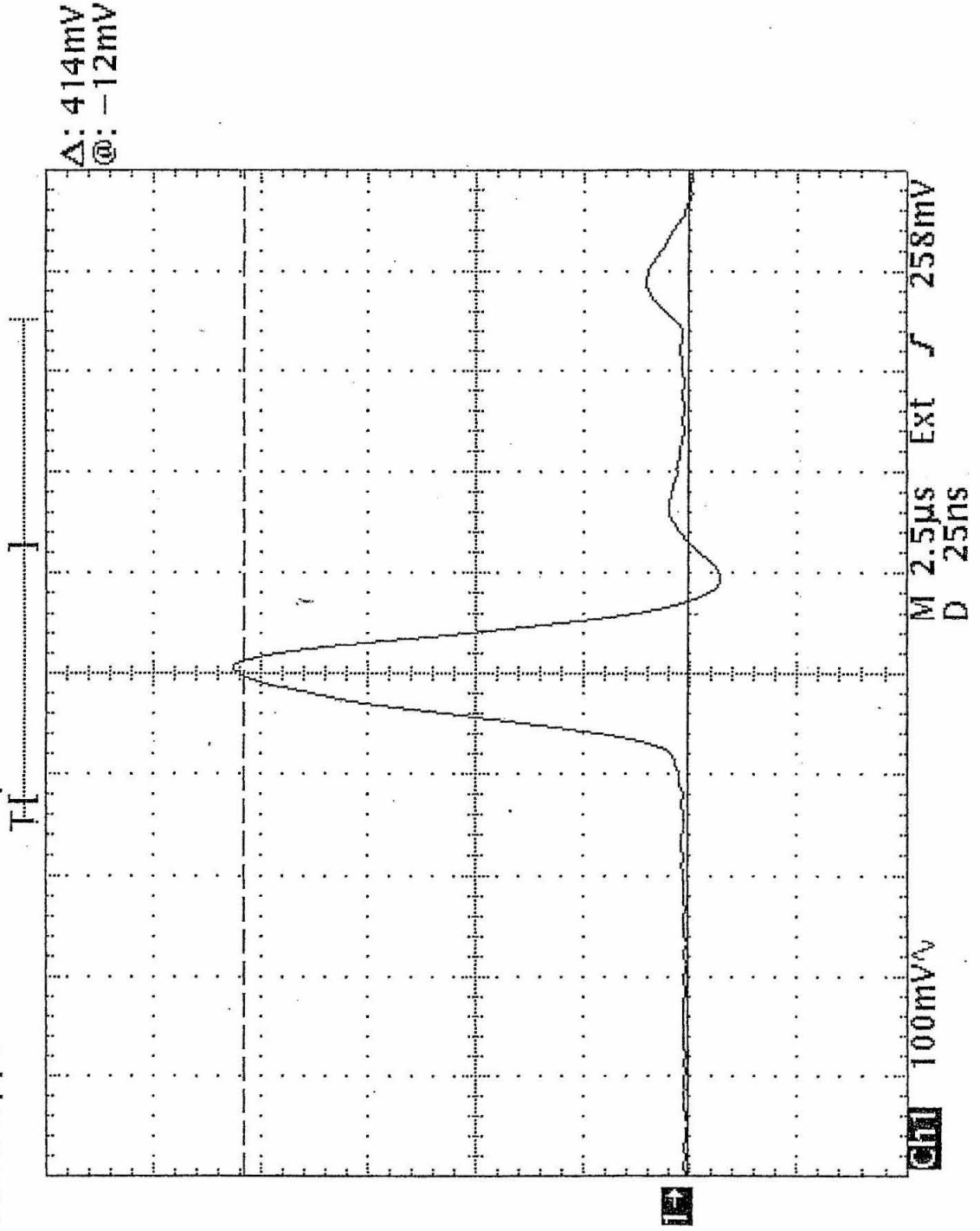


Figure B-3

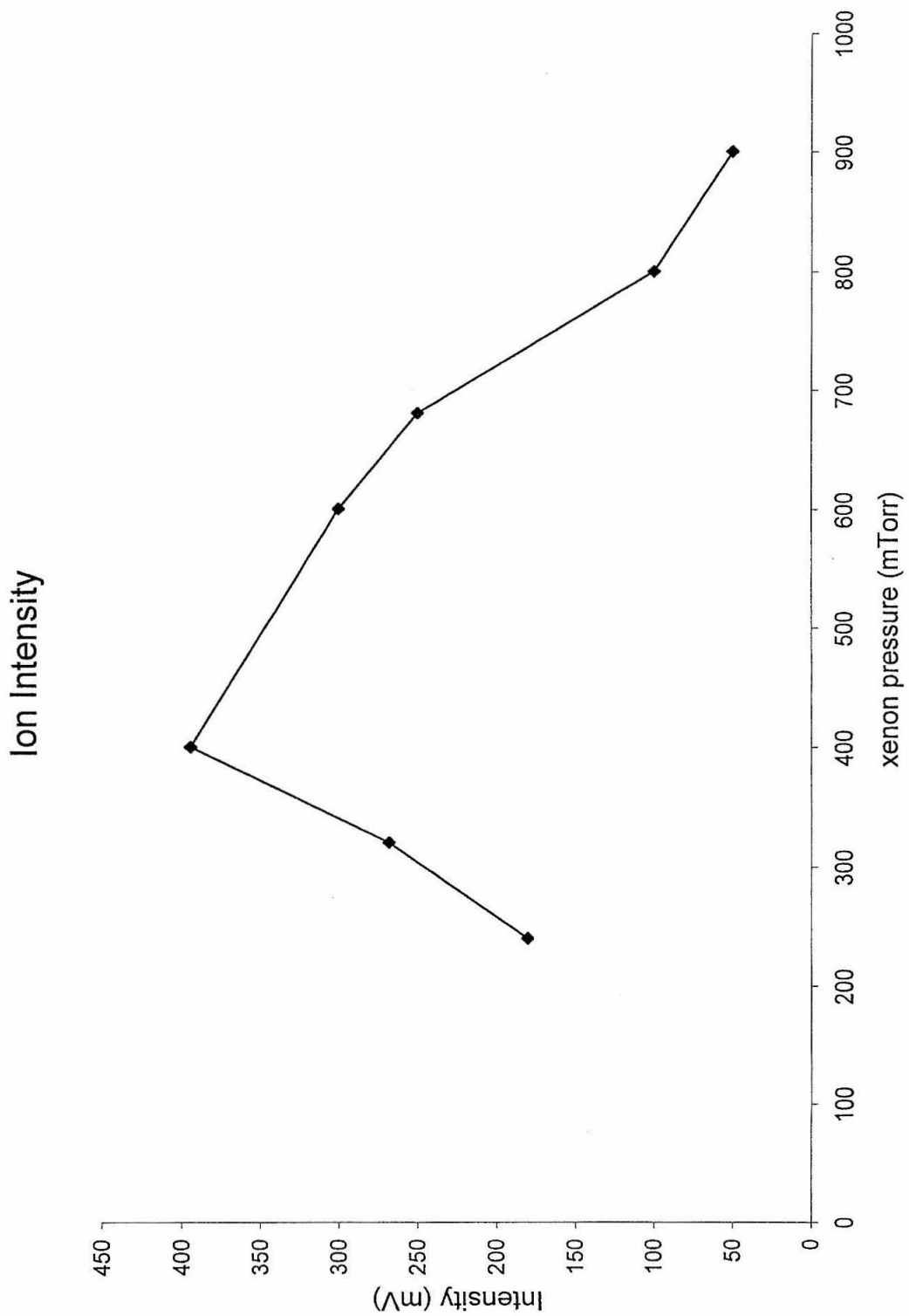


Figure B-4